ROMA TRE

UNIVERSITÀ DEGLI STUDI

SCUOLA DOTTORALE IN

GEOLOGIA DELL'AMBIENTE E DELLE RISORSE

XXIII CICLO

SEZIONE GEOLOGIA DELL'AMBIENTE E GEODINAMICA

Coupling at plate boundaries: insights from laboratory experiments

presented by

FABIO CORBI

accepted by the recommendations of

Prof. Claudio Faccenna, examiner

Dr. Francesca Funiciello, co-examiner

ROME, 2011

Table of contents

Abstract

The aim of this Thesis is to study the role of interplate frictional properties on boundary shaping and seismicity associated with subduction zones. This is achieved by means of a multidisciplinary approach, combining two different scales of analogue models, rheometry and worldwide statistics of subduction-related thrust-type earthquakes. Concerning the key problem of long-term frictional resistance to subduction, I relate the peculiar shape observed along Andes at present-day and associated topography to lateral variation in mechanical coupling. Frictional processes acting along the subduction thrust fault play also an important role also on shorter time-scale with effect on seismicity. The strategy of the adopted approach is to formulate the simplest setup allowing systematically the separation between different effects.

The Andean belt is the result of a favorable combination of plate kinematic parameters. While the Nazca plate, driven by negative buoyancy, undergoes weakened continental South America, mechanical coupling between converging plates is resisting to this motion. The development of trench curvature, shortening of the overriding plate, and topography could be related to lateral variation of the degree of mechanical coupling between converging plates. Here I use laboratory models of subduction in order to qualitatively test this hypothesis (Chapter 3).

Most of the global seismic energy is released by discontinuous shear of the frictional interface between the subducting and the overriding plate. First-order importance in controlling the seismic variability of subduction zones is recently attributed to interface roughness (including amount of sediments) and subduction velocity. Here I present a set of spring block-like models, which is known to mimic the seismic behavior, with the aim to explore the role played by the contact roughness, sliding velocity and normal load in friction dynamics (Chapter 5). The experimental set-up consists of a viscoelastic gelatin slider - analog of the Earth's crust - moving on sandpaper, a

small scale rough interface representative of the interplate contact. These experimental results, combined with worldwide seismic observables, offer the possibility of reconciling within a single model where contact interface is evolving during plate subduction the occurrence of creeping-velocity strengthening and seismic-velocity weakening regions along the subduction thrust plane. This work is supported by a preliminary systematic study of both rheological and physical properties of a wide range of gelatins (Chapter 4) which helped in selecting the right material (pig skin 2.5 wt.% at 10 °C) for a suitable experimental set-up to downscale model for subduction interplate seismicity.

I use both tribological and rheological background to built a realistic (wedge shaped) analogue model of subduction thrust-type earthquakes and rupture dynamics including rate- and state- friction and viscoelastic deformation (Chapter 6).

Chapter 1

General introduction

1.1 Preface

Subduction is the fundamental and most studied process in modern geodynamics. Earthquakes, volcanic activity, mountain building, and oceanic trench formation represent the most evident long- and short-term results of the activity occurring along convergent margins. The negative buoyancy of the cold subducted lithosphere (i.e. slab pull force) is supposed to be the main engine driving the subduction process against several resistive contributions [see McKenzie, 1977; Funiciello et al., 2003, Capitanio et al., 2010], among which an important contribution is played by the frictional shearing of the subducting plate below the overriding plate [e.g. McKenzie, 1977; Müller and Phillips, 1991; Ericksson and Arkani Hamed, 1993, Mart et al., 2005]. There is still a great debate on the essence of plate interaction and, in particular, on the way it is influencing plate boundary shaping and interplate seismicity. Only indirect observables are available (e.g. seismological data, remote sensing images, field and structural geology) on the effects of plate interaction and it could be useful their integration with results coming from ad hoc laboratory models. In fact, only through analogue modelling is possible to provide a direct control on the evolution of the studied physical process.

Along the pacific margin of South America the second world's largest mountain belt stand out and several mega-earthquakes occurred offering an ideal laboratory for studying interplate interactions.

The Andean system, where the Nazca plate undergoes continental South America, is in fact, regarded as the archetype of Cordillieran-type mountain belt. Its peculiar shape is progressively being acquired through clockwise and counter-clockwise rotations, respectively South and North of the Bolivian Orocline [Allmendinger et al., 2005; Maffione et al., 2009]. Even if there is no clear consensus on the timing of rotation (which is estimated to have occurred 30-40 Ma and 15 Ma ago for the southern- and northern Andes, respectively) the community agrees that most of the curvature developed because the central Andes experienced more crustal shortening during the late Cenozoic compared to elsewhere along the margin [e.g. Isacks, 1988] directly influencing its uplift history. Nonetheless, which geological process may simultaneously reconcile crustal shortening, curvature of the margin, and Andean uplift still stands as a most intriguing question in geodynamics. Width, age and buoyancy differences of the subducting plate may all play a role in determining the curvature of the margin [e.g. Schellart et al., 2007; Molnar & Atwater, 1978; Gorbatov & Kennett, 2003]. Laboratory models already pointed out that mechanical coupling [Mart et al., 2005] and that coupling combined with the presence of topography [Marques & Cobbold, 2006] may strongly affect the trench curvature. In this Thesis I demonstrate the possibility to relate trench curvature, shortening of the upper plate, and topography in amounts equivalently comparable to what is observed along Andes with lateral variations of mechanical coupling between subducting and overriding plates.

Heterogeneities along the subducting and overriding plates play also a key role in controlling the peculiar seismic signature characterizing convergent margins, influencing asperities and barriers distribution [Lay and Kanamori, 1982; Aki, 1984; Scholtz, 1998; Saffer and Marone, 2003; Bilek, 2005]. The interplate contact is seismogenic only in a specific depth interval [Scholz, 1998], which globally is comprised between 11±4 km and 51±9 km [Heuret et al., 2009] and corresponding to a temperature range of 100-150°C to 350-450°C [i.e. Hyndman and Wang, 1993; Wang, 1995, Hyndman et al., 1997; Currie et al., 2002]. The updip limit of seismogenic thrust

faulting is alternatively explained by the transition illite-smectite [Pytte and Reynolds, 1988] or by fault gouge lithification processes [Marone and Saffer, 2005], while the downdip limit is possibly controlled by the brittle–ductile transition of the crustal material [i.e. Brace and Kohlstedt, 1980] or by the intersection of the slab with the forearc mantle wedge [Peacock and Hyndman, 1999]. Focusing on along strike direction, the seismic behaviour of subduction thrust fault can be described by the "asperity model" [Lay and Kanamori, 1981; Lay et al., 1982], according to which asperity size correlates positively with earthquake magnitude. Subducting plate structure and amount of sediments has been proposed to play an important role on asperities distribution [see Bilek et al., 2005 for a review]. Bird et al [2009] highlighted the complex feedback relationship of subduction velocity and interplate seismicity.

Heuret et al., [in press] pointed out noteworthy correlations between a wide range of influencing parameters on seismogenic behavior searching for cause-effect relationships. However, robust agreement exists only in general understanding of the process but other critical details remain obscure:

- Why is interplate seismicity extremly variable in wordwide subduction zones?

- Which is the role played by subduction velocity, lithostatic pressure and roughness on interplate seismicity?

- Which are the mechanisms enhancing ~1000 km rupture along strike and, in turn, the triggering of mega-earthquakes (Mw>8.5) ?

- Can the structural evolution of the fault zone influence the seismogenic behaviour of subduction faults?

Answering these questions will help understanding subduction related seismicity.

1.2 Outline of Thesis

To address such considerations I will investigate physical processes governing plate interface frictional behaviour a) proposing a dynamic model to explain the Andean belt evolution and b) speculating on mechanisms able to produce the seismic variability characterizing the subduction thrust fault. I will realize laboratory models investigating the overall behaviour of subduction (i.e. mantle scale models characterized by large temporal and spatial scales) and spring-block/wedge models (i.e. wedge scale models characterized by small temporal and spatial scales) aimed to shed light on the dynamics of interplate seismicity. Subsequently, experimental results will be separately linked to available natural observables.

After briefly reviewing the methodology of laboratory modelling and adopted techniques (Chapter 2), I will focus on mechanical coupling along the central Andes and on implications for trench curvature, shortening, and topography (Chapter 3). Mechanical coupling represents one of the major controlling factor to mountain building. The surface expression of long-term coupling is found in the Andean belt where Nazca plate converges towards South America. The pronounced curvature of the convergent margin is symmetric with respect to the direction of convergence, the distribution of trench sediments, and the topographic volume of the Andes. The evolution of Andean belt is irregular in time and present great heterogeneities in space. The fundamental problem of what caused this peculiar evolution remain obscure. Here, supported by analogue models of subduction [e.g. Funiciello et al., 2003], I test the hypothesis that trench curvature, shortening of the upper plate, and uplift in amounts equivalently comparable to what is observed in the Andean case can be the result of lateral variation in the mechanical coupling between the overriding and the subducting plates.

On shorter-timescale and smaller-lenghtscale, deformation at converging margins occur by means of megathrust earthquakes. Some major problem of seismic behaviour of subduction zone

remains enigmatic. In this Thesis, I introduce and test a new experimental approach, based on spring-block-like models, to simulate seismic cycle including viscoelastic deformation. Starting from the description of the approach including model similarity, which is discussed in Chapter 2, I will focus on material requirements presenting an extensive study of both rheological and physical properties of a wide range of gelatines (Chapter 4). This study of general relevance, has been performed aiming to find the best analogue material suitable both for crustal visco-elasto-brittle deformation and for analogue earthquake simulation. According to 'similarity criteria'[e.g.Weijermars and Schmeling, 1986], I found that pig skin 2.5 wt.% at 10 °C has the right rheological and physical requirement to be used as analogue material.

I use spring-block models [e.g. Burridge and Knopoff, 1967; Voisin et al., 2008; Chapter 5], which is known to mimic the seismic cycle, aiming to study of the role played by the distribution of contact roughness, sliding rate and normal load in friction dynamics. This simple setting allows to explore how the effect of each single parameters with speculation on seismicity. This approach introduce the following new features: (a) using a gelatin slider reproducing the complex visco-elasto-brittle rheology representative of a properly scaled crustal/lithospheric behaviour [DiGiuseppe et al., 2009] and, therefore, taking into account also the time-dependence of the interseismic deformations; (b) testing a wide range of contact materials with roughness profiles characterized by well-sorted asperities; (c) investigating the effect of lithostatic pressure at seismogenic depths; (d) exploring both frictional static and rate- and state- effects.

I found that a) both stick-slip dynamics and stable-sliding occur, depending on sliding velocity and interface roughness and b) that stress drop and frequency of slip episodes vary directly and inversely, respectively, with the amplitude of asperities. Slow sliding velocity and an increase in normal pressure tends to favor stick-slip. The velocity strengthening/weakening parameter in the state- and rate-dependent dynamic friction law becomes negative (i.e. seismic) for intermediate (scaling to tens-hundreds of meters) values of asperity amplitude. Comparing experimental results

with the distribution of seismic energy release with depth along subduction thrust faults leads to the hypothesis that their behavior is primarily controlled by the depth- and time-dependent distribution of asperities.

Combining rheological (Chapter 4) and tribological/seismological (Chapter 5) results I build a novel analogue model (Chapter 6) featuring realistic rheology and friction monitored with state-of-the-art image analysis tools (photoelasticity and Particle Imaging Velocimetry) capable of generating time series of deformation and stress at various timescales. Aiming to explore the physics of seismic behaviour of subduction thrust fault and rupture dynamics in a properly scaled wedge shaped margin which represents the future direction of work.

Finally, Chapter 7 summarizes and discusses the results obtained in this study. Chapters 3, 4, and 5 are structured as papers already published or submitted. Unfortunately, this format entails unavoidable duplications, especially when experimental assumptions are presented.

Chapter 2

Foundations to modeling

2.1 What is a laboratory model and why it is important for geodynamics?

A model - either analog or numerical - is a simplified scaled representation of nature, though on a more convenient geometric and temporal scale (smaller and faster). The purpose of models is not simply to reproduce natural observation, but primary to test by controlled experiments hypotheses as to the driving mechanisms of tectonic processes.

Experimental tectonics can be said to have begun with the scale models of folding under compression performed by *Sir James Hall* [1815]. Since 1815, thanks to the introduction of proper scaling relationships [e.g. Hubbert, 1937; Ramberg, 1981; Weijermars & Schmeling, 1986] and improvement in the understanding of the rheology of both natural and model materials, experimental tectonics advanced considerably turning out to be a solid method for studying geodynamic processes.

The main advantage of analogue modeling lies in the fact that a correctly constructed model passes through an evolution which is the physical response of the system to the applied experimental conditions. Through experimental models is possible to study complex processes for which governing equations are still poorly known or too complex to be numerically solved. Moreover, experimental tectonics permit an easy control of boundary conditions and approach problems using 3D settings. These advantages of laboratory models make this methodology a valid tool for the advancement of our understanding of geodynamic processes.

2.2.1 How to design a laboratory model

The aim of any laboratory model is to determine functional relations that link causes (i.e parameters) controlling the studied problem to the related effects. A general workflow for modeling can be schematically listed as:

1. identification of the problem to study;

2. application of the "similarity criteria";

3. determining of the materials that satisfy the similarity criteria;

4. running the models;

5. verifying repeatability;

6. interpretation of the obtained results;

7. definition of a "general" theory and possibly find a scaling law allowing to export experimental results to natural cases.

The first step consist of selecting a certain phenomenon to model (phase 1). Experimental tectonics has examples both in large-scale geodynamic applications (subduction, convection, evolution of thrust belts, formation of basins, pluton emplacement, mantle and crustal convection) and in smaller scale structural geology (faults, folds, diapirism, boudinage). With right assumptions/simplifications, it is also possible to model complex multi-scale phenomena like earthquakes. Despite the strength of the methodology, it is not possible to model every tectonic process because of often unavoidable technical limitations and, mainly, the existence of a narrow number of materials that can properly scale the range of natural mechanical and thermal behaviors. A key step of phase 1 is the oversimplification of the adopted setup. For example, one can choose to neglect the existence of the overriding plate in a subduction model taking into account that only partial aspects of the natural prototype will be reproduced.

A fundamental requirement for laboratory models is the ability to scale natural processes to laboratory environment. Similarity analysis (phase 2) is the central step in the model design helping

to select analogue materials, dimensions of the experimenal setting and rate of deformation. In order to scale an analogue model to a natural process, the model should be geometrically, kinematically, dynamically and rheologically similar to the prototype [e.g. Hubbert, 1937; Ramberg, 1981]. The application of the similarity theory starts with the identification of the most relevant physical parameters active into the natural system. Similarity theory gives birth to a set of dimensionless parameters (for length, velocity, force and material rheologic parameters). Each set of dimensionless parameters defines a family of equivalent solutions, which only differs by a scale factor. When governing equations are known, they can be nondimensionalized to make the relevant parameters appear explicitly in the equations. If the governing equations are not known one can use the Buckingham-Π theorem [see Buckingham, 1914 for the theory and Boutelier and Cruden, 2008; Boutelier et al., 2008 for an extensive example of application to analogue modeling]. According to this theorem, if a model is described by N-dimensional parameters of which M have independent physical dimensions, then this model can be completely described by (N-M) combinations of the dimensional parameters. A list of dimensionless parameters frequently used in experimental tectonics is in Table 2.1.

Dimensionless numbers obtained adopting similarity criteria are, therefore, essential to select analog materials and to design a properly scaled experimental models (phase 3). Unfortunately, available analog materials able to satisfy similarity criteria are limited. Moreover, the selection must take into account that the material needs to be preferably inexpensive and manageable in sufficient quantities.

Geometric parameter	$l_0=l_m/l_n$	(length scale factor)	
Rheologic parameters	$E_0=E_m/E_n$	(Young modulus scale factor)	
	$\rho_0=\rho_m/\rho_n$	(density scale factor)	
	$\eta_0=\eta_m/\eta_n$	(viscosity scale factor)	
Kinematic parameters	$t_0=t_m/t_n=\eta_0/\sigma_0$	(time scale factor)	
	$v_0=v_m/v_n=\sigma_0\,l_0/\eta_0$	(velocity scale factor)	
	$g_0=g_m/g_n$	(gravity scale factor)	
Dynamic parameters	$\sigma_0=\sigma_m/\sigma_n$	(stress scale factor)	
	Ar=forces from density contrast/total strength		*Argand number*
	$F=gl^2\Delta\rho/\eta v$	(buoyancy force/viscous force)	*Buoyancy number*
	$Re=vl\rho/\eta=vl/\mu$	(inertial force/viscous force)	*Reynold number*
	$Ra=D^3g\rho\alpha\Delta T/\kappa\eta=D^3g\eta/\kappa$		*Rayleigh number*
	$Pr=\mu/k$	(viscous/thermal diffusivity)	*Prandtl number*
	$Pe=vl/\kappa$	(advection of heat/conduction of heat)	*Peclet number*
	$Nu=Hl/\kappa(T_2-T_1)$	(heat transfer/heat transfer which would occur by conduction)	*Nusselt Number*

Table 2.1: List of the most common dimensionless parameters used in the similarity analysis for laboratory experiments. Robust scaling implies that characteristic dimensionless ratios are the same for the model (subscript m) and its prototype (subscript n). l is length, ρ is density, η is viscosity, μ is the kinematic viscosity, g is gravity acceleration, t is time, v is velocity, σ is stress, E is Young's modulus, D is depth of convective mantle, Δp is pressure difference, κ is thermal diffusivity, k the thermal conductivity, H is heat transfer per unit area, T is the temperature, α is the thermal expansion coefficient.

Commonly, the brittle behavior is modeled by quartz sand with uniform grain size [Hubbert, 1951; Horsfield, 1977; Naylor et al., 1986; Vendeville et al., 1987; Davy and Cobbold, 1988, 1991; McClay, 1990; Ratschbacher et al., 1991; Richard, 1991; Richard and Krantz, 1991; Richard et al., 1991, 1995; Lallemand et al., 1992; Nieuwland and Walters, 1993; Brun et al., 1994; Faccenna et al., 1996, 1999; Bonini et al., 1997; Hatzfeld et al., 1997; Keep and McClay, 1997; Basile and Brun, 1998] or artificial well classed microspheres [e.g. Rossi and Storti, 2003,]. These are Coulomb materials with an internal frictional coefficient similar to nature (φ~0.6) and a negligible value of cohesion [McClay, 1990; Krantz, 1991; Faccenna et al., 1995;Gutscher et al., 1998; Acocella et al., 2000; Bonini et al., 2000; Mart and Dautevil, 2000; Schellart, 2000; Cobbold et al., 2001; Turrini et

al., 2001; Grotenhuis et al., 2002; Rossi and Storti, 2003]. Silicone putties and plasticines are materials that are mostly used to simulate the ductile creep behavior of rocks (lower crust, lithosphere, magma evaporitic and clay levels). They are viscoelastic materials but the elastic component is never involved in scaled geological models. In first approximation the silicone putty can be considered a Newtonian fluid with stress that increases linearly with strain rate [Weijermars, 1986]. It is composed of a pure polymeric substrate (among the most used PDMS and PBDMS) with the addition of solid particles (galena, barites) to calibrate the density /viscosity and, more in general, the rheology of model materials [see Weijermars, 1986; ten Grotenhuis et al., 2002; Boutelier et al., 2008 for rheological studies on putties for analogue models]. Finally, the astenosphere/mantle is frequently modeled by honey or syrups (glucose, corn, maple) which are Newtonian low viscosity and high-density fluids [e.g. Funiciello et al., 2003; Bellahsen et al., 2005; Funiciello et al., 2006; Heuret et al., 2007; Espurt et al., 2008; Guillaume et al., 2009; Guillaume et al., 2010; Schellart, 2004, etc].

Phase 4 consists in running the models. As a rule of thumb, a complete set of experiments should be realized widley exploring the parameter space of the analyzed problem. Hence, the parameters of interest are systematically varied while keeping constant all the other constraints. Models can be performed in a natural gravity field ($g_{model}=g_{nature}$) or in a centrifuge to create an increased gravitational field [Mulugeta, 1988; Liu and Dixon, 1991, 1995; Dixon and Liu, 1992; Ramberg, 1981; Koyi, 1997; Brun, 1999 Mulugeta and Ghebreab, 2001; Corti et al., 2001, 2002, 2003; Mart et al., 2005]. In the first case the natural prototype is reproduced in a apparatus like a vice or shear box. Techniques to construct and deform the model are a function of the analyzed geodynamic problem and of the selected material. External forces are driven at constant rates by step- or computer-controlled motors. It is useful to analyze a process making models only progressively more complex so that is possible to separate the contribution of single variables. In this phase is crucial to get as much information as we can from a single model (e.g. laser scanner is used together

with cameras to measure uplift and associated horizontal deformation at the same time; reference), allowing for the best quantification of the experimental process.

Experiments have to be repeated several times under the same boundary conditions to ensure repeatability (phase 5).

Final steps (phases 6 and 7) consist in interpreting results with the aim to formulate a theory finding a scaling law. It is, in fact, thanks to scaling law that is possible to predict the behavior of a given experimental system and, afterward, try to export obtained results to natural cases.

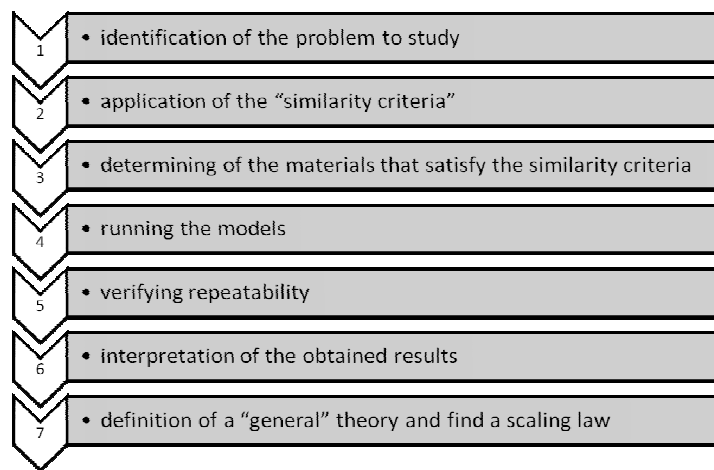|	
1	• identification of the problem to study
2	• application of the "similarity criteria"
3	• determining of the materials that satisfy the similarity criteria
4	• running the models
5	• verifying repeatability
6	• interpretation of the obtained results
7	• definition of a "general" theory and find a scaling law

Figure 1: Flow chart of experimental phases.

2.3 Measurement and visualization

The quantification of the deformation history of the model is crucial to describe a certain geodynamic process. There are several parameters that could be measured in an experimental model, however the most common can be schematically listed as: a) local measurement of motion; b) flow pattern and velocity; c) stress and strain; d) model. An overview of the most common tools used in modeling follow.

It is possible to directly measure the displacement of an interface defined by a grid just by cross correlating two subsequent photos.

The common procedure for measuring flow velocity/pattern characterizing the model consist in seeding neutrally buoyant particles (e.g. tiny air bubbles, hollow glass beads, polline) into the analog material and illuminating a cross-section of the experiment. A transparent analog medium and a good illumination (I.e. UV lamps or laser beam) are key ingredients to track the flow. Particles are small (generally few microns) and have densities as close to that of the fluid as possible, in order to passively follow the local flow. The Particle Imaging Velocimetry (PIV) technique provides a quantification of the velocity field over the entire selected plane. The PIV requires a high particle density and calculate the mean displacement of particles in a small region of the image (which is called interrogation window) by cross correlation of the transparency signal of the same interrogation window in two subsequent images [Adrian, 1991; Westerweel 1998; Nogueira et al., 2001]. The PIV algorithm is fast but the resolution is not so special as compared to Particle Tracking Velocimetry (PTV), which is used to track individual particles in subsequent images [Kobayashi et al., 1989; Cenedese and Querzoli 1997; Cenedese et al., 1997]. Recently Moroni and Cenedese [2005] successfully combined the good resolution of PTV with the fast algoritm of PIV. The result is a new Feature Tracking (FT) technique which has been applied to track mantle flow in a laboratory models of subduction by Funiciello et al. [2006] . FT reconstructs the displacement field by selecting image features (image portions suitable to be tracked because

17

they remain almost unchanged for small time intervals) and tracking these from frame to frame. The matching measure used to follow a feature (and its interrogation window) and its 'most similar' region at successive times is the 'sum of squared differences' among intensity values.

Stress and strain can be determined from the displacement and velocity fields measured by the method described above. Another possibility includes the property of certain material to become birefringent under the action of shear forces. Similarly to Earth's mantle, the particles of these material are resulting in an anisotropic distribution if the media is subject to shear force. The technique that uses this material property to directly measure the stress is known as Photoelasticity (e.g. Jessop and Harris,1949 for principles and methods) and the instruments designed to observe objects under polarized light is the polariscope. It is physically based on the fact that when polarized light passes through a stressed material, the light separates into two wavefronts traveling at different velocities, each oriented parallel to a direction of principal stress (s_1, s_2) in the material, but perpendicular to each other. Different values of the refraction index are assigned to two component that are out of phase when leaving the birefingent material. This difference in optical path can be measured by interferometry. The resulting output consist in a pattern of color fringes where fringes number is proportional (thanks to the stress-optic Brewster's law).
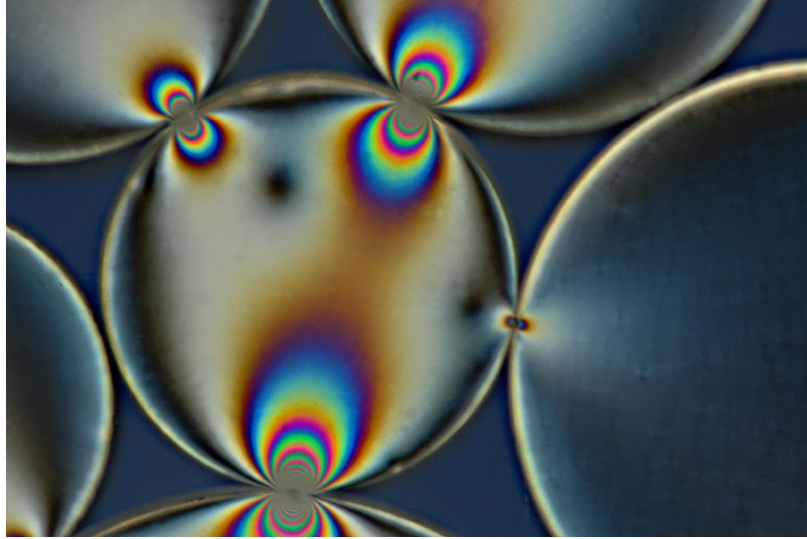
Figure 2: A typical photoelastic image. The stress at any point is proportional to number of fringes (from Allersma's webpage).

Schlieren and shadowgraph are two visualization techniques that use the fluid's refractive index dependency on temperature and composition. A flow in a transparent media alters the refractive index distribution. From the deformation of the optical wave front one can, therefore, deduce information on the refractive index of the medium and, in turn, speculate on its temperature and composition. Both shadow and schlieren techniques are whole-field integrated optical systems that project line of sight information onto a viewing screen or a camera (see Settles 2001 for a comprehensive review).

The use of thermochromic liquid crystals allow to visualize the 2D temperature field of a fluid without perturbing it (Rhee et al., 1984). These liquid crystals undergo to helical distortions and generate reflection at optical wavelength. The pitch of the wavelength depends on temperature and, thus, the color of the material changes over a temperature interval of few degrees. When subject to an incident white light, crystals are transparent-red for low temperatures and passes to blue-green at high temperatures.

The experimental surface topography can be quantified using a 3D laser scanner. These instruments are accurate up to 150 microns and scans are completed very quickly (few seconds). The laser output consists of a XYZ matrix where each coordinate of the scanned plane is associated an elevation data. Several commercial softwares filter noises and redundancies in measurements and also easily allow to subtract the scanned topography to a reference level.

It is also possible to measure model topography using an high-frequency induction coil proximity probe [Olson and Nam, 1986] with a sensitivity of 0.02 mm or using an interferometer [Griffiths et al., 1989]. The latter tool allows to reconstruct from the fringes pattern both the shape and the width of a feature including its height. Fringes of the interferogram are topographic contours with a vertical distance a part of half the laser wavelength. The surface height at any position is given by the number of fringes.
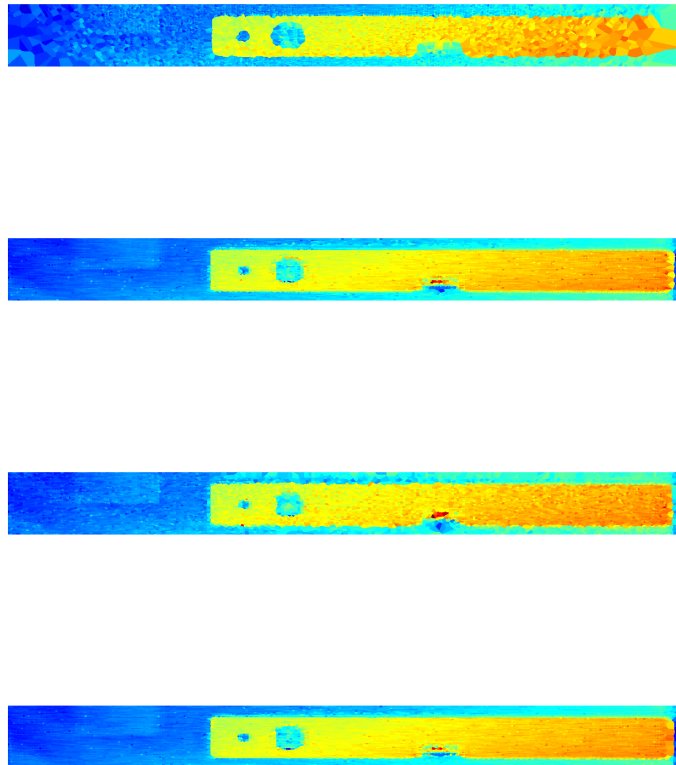
Figure 3: Time/resolution test for a 3D (eScan-Real 3D) scanner. Orange colors (right side of the picture) highlight a 20 cm long, 2 mm thick ruler. The number of point detected is increasing toward the South. Topography is acquired in less than 4 seconds. It is also possible to obtain longer scan with higher resolution.

Other more sophisticated tools can be added to the set-up in order to monitor specific quantities (i.e. X-ray tomography: no destructive analysis of internal deformation, infrared cameras). More information about the tools and methodologies used for this Thesis can be found in Chapter 3, 5 and 6.

2.4 State of the art of laboratory models

Since the pioneer work of Sir James Hall (1815), important changes have occurred in analogue modeling. They can be schematically listed as: (i) the development of a quantitative theory of scaling [Hubbert, 1937; Ramberg, 1967; Weijermars and Schmeling, 1986]. This point has been extensively described in section 2.2; (ii) continuous improvement in the knowledge of the rheology and frictional properties of both natural and model materials [e.g. Ranalli 1995; Boutelier et al., 2008; Di Giuseppe et al., 2009; Rosenau et al., 2009]. In order to reproduce the lithospheric strength profile modelers used to pile up different materials [e.g. sand for the brittle upper crust and silly putty for the ductile lower crust; see Davy and Cobbold, 1991]. This procedure is unfortunately including great approximations and "unpredictable" coupling between the two layers. Aiming to better constrain vertical and horizontal tectonic processes modelers are pushing to find a single material to model the Earth rheological structure [Di Giuseppe et al., 2009, 2010]. Finally, (iii) technological advances which have allowed the construction of more sophisticated experimental apparatus (e.g. including temperature gradients or controlling evaporation) and quantification tools (see previous paragraph for an overview on most popular measurement techniques).

2.4.1 Laboratory models of subduction

The subduction of oceanic lithosphere is the dominant process in the dynamics of the Earth [Chapple, 1977]. A slab sinks into the mantle because of its negative thermal and compositional buoyancy. The combination between a) temperature difference between the cold slab and the surrounding warm mantle and b) the low lithospheric thermal diffusivity causes a negative density anomaly and, consequently, a downwards directed body force. Subduction involves a wide variety of physical and chemical processes: earthquakes, volcanism (dehydratation, melting and melting migration), phase transformations, thermal effects, mantle circulation, and plate motion [e.g.,

Dewey, 1981; Fowler, 1993; Kincaid, 1995; Davies, 2001]. Understanding the way in which a cold solid lithosphere plunges into a convective mantle, therefore, can be addressed from several sides.

Seismology offers the only direct indication of the size, the geometry and the deformation of the down going slab. Zones of high seismicity and high velocity suggest that oceanic lithosphere sinks into the mantle with different dips and shapes that apparently cannot be explainable by a simple rule [e.g. Jarrard, 1986, Heuret and Lallemand, 2005, Cruciani et al., 2005]. Other interdisciplinary constraints from geology, geochemistry, petrology and mineral add important indirect constraints to the available "subduction database" [e.g. Jarrard, 1986, Heuret and Lallemand, 2005; Lallemand et al., 2005; Sdrolias and Müller, 2006; Schellart, 2008; Hayes et al., 2009]. For all we know, it is assured that present day subduction features are not consequence of a steady state phenomenon (e.g. Funiciello et al., 2003). Subduction may evolve for limited timeframe in a "quasi-steady" state but it certainly does not initiate and does not end as such. Several authors studied the dynamical forces acting on the slab-mantle system [Forsyth and Uyeda, 1975; Chapple, 1977; McKenzie, 1977; Davies, 1980; Conrad and Hager, 1999; Funiciello et al., 2003, 2008; Schellart 2004, 2008; Capitanio et al., 2009; Wu et al., 2009; Buffett&Rowling, 2006,]. It has been found that the driving slab pull arising from the negative buoyancy of the slab and the bending resisting force represent the main forces controlling the subduction process. A secondary role is played by ridge push (active force) and resistance to sliding along the subduction fault and both shear and normal slab-mantle interface forces (resisting forces). Nevertheless in a dynamic setting the absolute magnitude of these forces and their mutual interaction are still poorly understood. Laboratory models represents a key-tool providing an useful dynamic picture of the subduction process and a powerful link to seismological observables.

Taking into account of strong uncertainty in the rheological characterization of the Earth's layers [Karato and Wu, 1993; Karato et al., 2001; Ranalli, 2001; Choi and Buck, 2010; Stadler et al., 2010; Mei et al., 2010], modern modeling of subduction simulating the different phases of the

slab evolution, trying to speculate about some of the most intriguing questions in geodynamics such as the enigma of subduction initiation, the importance of trench migration, the fate of the slab at the 660 km discontinuity, the importance of the 3D slab induced mantle flow, and dynamic topography.

Shemenda [1992, 1993] performed analog models of subduction initiation using a complex elasto-plastic lithosphere (a mixture of powders and hydrocarbons) and an low viscosity upper mantle (water). Laboratory results demonstrated that subduction cannot initiate without the simultaneous existence of pre-existing discontinuities and horizontal compression. On the contrary, Faccenna et al. [1999] demonstrated that if a passive margin is subject to low horizontal compression (i.e. slow ridge-push) independently by the presence of pre-existing discontinuities, it may likely evolve into a Rayleigh–Taylor instability, enhancing the following subduction development. The experimental setup apparently seems not much different from Shemenda's one. However, the adopted materials are considerably different, consisting of sand and silicone putty to simulate the brittle and ductile parts of the lithosphere, respectively, with glucose syrup as the upper mantle analogue. This configuration overcome the major limitation linked to the Schemenda's setting: the high Reynolds number (i.e. about 10000), due to the fact that the water-mantle acts only an inviscid layer, does not allow to properly simulate the Earth-like Stokes flow. In the paper by Faccenna et al (1999), subduction initiates when the negative buoyancy (i.e. the driving engine) experimental force exceeds the viscous resisting forces of the lithosphere (i.e. slab bending, resistance to sliding along the subduction fault and shear and normal slab-mantle interface forces; see Funiciello et al., 2003, 2008 and Schellart, 2004 for experimental reviews of forces operating in the subduction system). Hence, the system appears to be not sensitive to the high shear strength of the brittle lithospheric layer but only to its ductile resistance. Mart and coworkers [2005] performed another set of analogue experiments focused on subduction initiation using the centrifuge technique. In this case the models are driven only by lateral/vertical density contrasts of plasticine layers -

enhanced by the centrifuge gravity - without the effect of any external lateral compression. Experimental results demonstrate that under the influence of enhanced gravity the oceanic plate detaches from the continental lithosphere and plunges at depth. They found that two ingredients - friction and density differences between the subducting and overriding plates - control the rate of thrusting, the amount of trench rollback and the shape/evolution of backarc basins.

After the beginning of subduction and during the journey of the slab into the upper mantle, trench velocity and slab geometry are found to be strongly time-dependent [Kincaid and Olson, 1987; Becker et al., 1999; Funiciello et al., 2003, 2004, 2006; Schellart 2004]. Using a simple single plate setting consisting of a viscous layers of silicone putty falling into glucose syrup, it has been observed how the slab dip progressively increases and the trench motion accelerates before the slab interacts with the 660 km discontinuity [e.g. Becker et al., 1999; Funiciello et al., 2003, Schellart, 2004]. However, the detailed behavior occurring during this phase can be strongly affected by the initial imposed conditions [Ribe, 2010]. Temporary steady state conditions of the subduction process can be recorded after the slab has interacted with the upper-lower mantle discontinuity [Funiciello et al., 2003, 2004, 2008; Schellart, 2004, 2008, 2009]. For the easiest configuration characterized by an impermeable deep barrier, Bellahsen et al. [2005] demonstrated that the velocity of subduction can be predicted by the dynamic interaction between acting and resisting forces, where- for the upper bound adopted modelling parameters- lithospheric bending likely represents the majority of the total resisting forces and primarily controls the trench behavior. In the same work, it has been highlighted also the unpredictable nature of trench motion which represents a key parameter for the subduction dynamics. Two characteristic modes of subduction have been observed systematically varying thickness, width, viscosity/density of the plate and mantle (e.g. Bellhasen et al., 2005, Funiciello et al., 2008) - a retreating and an advancing trench mode - resembling what recognized occurring in current subduction zones (Heuret and Lallemand, 2005, Funiciello et al., 2008).

However, the slab interaction with the 660 km discontinuity could be much complex than modeled with the previously described models with an impermeable barrier at depth, with the possibility for the slab to penetrate into the lower mantle as possibly highlighted by tomographic images [Van der Hilst et al. 1997, Bijwaard et al., 1998; Fukao et al., 2004]. Similar scenarios have been experimentally investigated by Kincaid and Olson [1987] by means of a three-layers purely viscous setup made of glucose syrups prepared at different temperatures/concentrations. Exploring various combinations of upper layer, lower layer, and slab densities-viscosities they recognized that the slab at the 660 km discontinuity can deflect, partially or totally penetrate as a function of the resistance offered at the boundary.

Using a similar setup, including a scaled Peclet number (a dimensionless scaling parameter, see table 2.1) but kinematically imposing the trench motion, Guillou-Frottier and co-workers [1995] highlighted five possible slab deformation modes at the 660 km discontinuity: sinking slab, stagnant slab, spreading slab, sinking pile and stagnant pile. Modes are governed by two velocity ratios, which characterize the horizontal and the vertical components of the slab velocity near the interface. In particular they found that slab penetration into the lower mantle takes the form of folded slab piles for large values of the velocity ratios, and stagnant behavior is promoted by rapid retrograde trench motion. A similar result has been experimentally achieved also by Griffiths and coworkers [1995], confirming the possible primary role played by trench migration rate in controlling the slab behavior at depth.

Ribe and coworkers [2007], quantifying factors controlling the style of deformation of sheets of viscous fluid poured onto a surface (i.e. speed, the height of fall, and the fluid properties), proposed a plausible physical interpretation of tomographic observations, suggesting buckling at depth.

Another intriguing aspect related to the subduction process and widely explored by means of laboratory models is represented by subduction induced mantle circulation and associated seismic anisotropy.

Pushed by seismological observation that trench motion could produce particular pattern in the upper mantle seismic anisotropy [e.g. Russo and Silver, 1994], Buttles and Olson [1998] used passively buoyant whiskers as analog of olivine a-axis in a model of subduction composed by a kinematically controlled Plexiglas slab moving into a box preliminary filled with syrup. They demonstrated that trench-parallel orientation in the seaward side mantle is controlled by amount of slab rollback while the mantle wedge orientation depends upon dip angle.

Rollback subduction induces flow both around and beneath the sinking slab with larger velocities in the wedge and flow focused toward the centre of the plate. These 3-D flows strongly influence the evolution of the plate. The amount of slab rollback depends on the degree of lateral confinement of the flow [Funiciello et al., 2003, 2004; Schellart 2004, 2005] and it is much reduced in the 2D-like models (i.e. laterally confined settings or models influenced by box boundary effects. For the adopted viscosity layering, this condition occurs when the distance between slab edges and sidewalls in less that the thickness of the convecting mantle). The lateral flow (toroidal flow), in turn, forces the hinge line to adopt a convex shape toward the direction of retreat [Funiciello et al., 2003; Schellart 2004].

An extensive study on three-dimensional aspects of mantle circulation in subduction zones, and the consequent temperature variations in the slab/ mantle wedge has been proposed by Kincaid and Griffiths [2003, 2004]. Using an undeformable Plexiglas subducting plate moving into a box filled with syrup combined with the PIV technique, they demonstrated the influence of the plate sinking style for speed, orientation and temperature of induced mantle circulation. Slab rollback motion (as also highlighted by Funiciello and coworkers in the same years using dynamically self-consistent models) triggers mantle circulation both around and beneath the sinking slab, with larger

velocities recorded in the wedge (up to 150% of the slab speed) and flow focused toward the center of the plate segment. They also demonstrated that the thermal evolution of the plate is strongly influenced by sinking style and rate: highest temperatures are along the edges of the slab for longitudinal sinking, but along the centerline of the slab segment for rollback motion.

Funiciello et al. [2006], using two linearly viscous layers of silicone putty and glucose syrup, investigated and quantified the influence of plate width and mantle viscosity/density on rollback and the induced 3-D mantle circulation. The poloidal component is the response to the viscous coupling between the slab motion and the mantle, while the toroidal component is produced by mantle lateral migration. Laboratory results show that both components are active since the beginning of the experiment and strongly episodic. Moreover, these models pointed up how mantle flow in subduction zones cannot be correctly described by the corner flow theory [ref. Turcotte and Schubert, 1978], assuming a two-dimensional steady state process [e.g. Tovish et al., 1978; Eberle et al., 2002;].
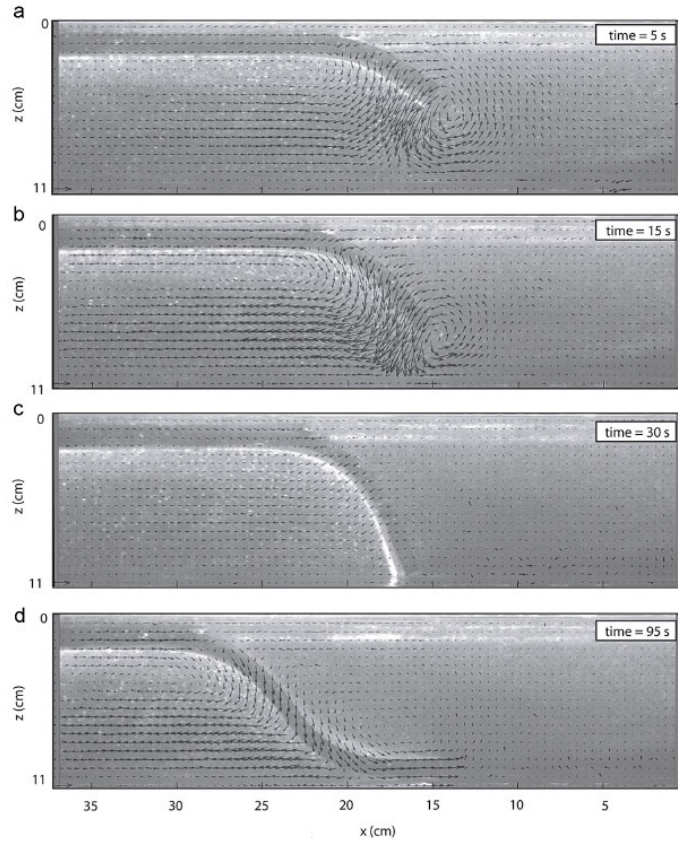
Figure 4: Four selected time steps of a subduction experiment showing the time-averaged velocity field recorded in the lateral view using the Feature Tracking technique. (a) and (b) First subduction stage, (c) second stage, and (d) third stage. The reference velocity shown at the bottom left corner of each panel is 0.1 cm s^{-1} [Funiciello et al., 2006].

Analogue models of subduction can be used to investigate relationships between mantle circulation and associated dynamic topography over geological time scales. Guillaume et al. [2010] demonstrated that a slab window opening during subduction strongly modify slab induced mantle circulation. In particular, the opening of a slab window and the upwelling of sub-slab mantle produces a regional-scale non-isostatic topographic uplift of the overriding plate that would correspond to values ranging between about 1 and 5 km in nature.

Figure 5: Lateral view of three stages of evolution of experiments characterized by different modes of subduction: (a) mode I, retreating trench mode; (b) mode II, retreating trench mode following an advancing s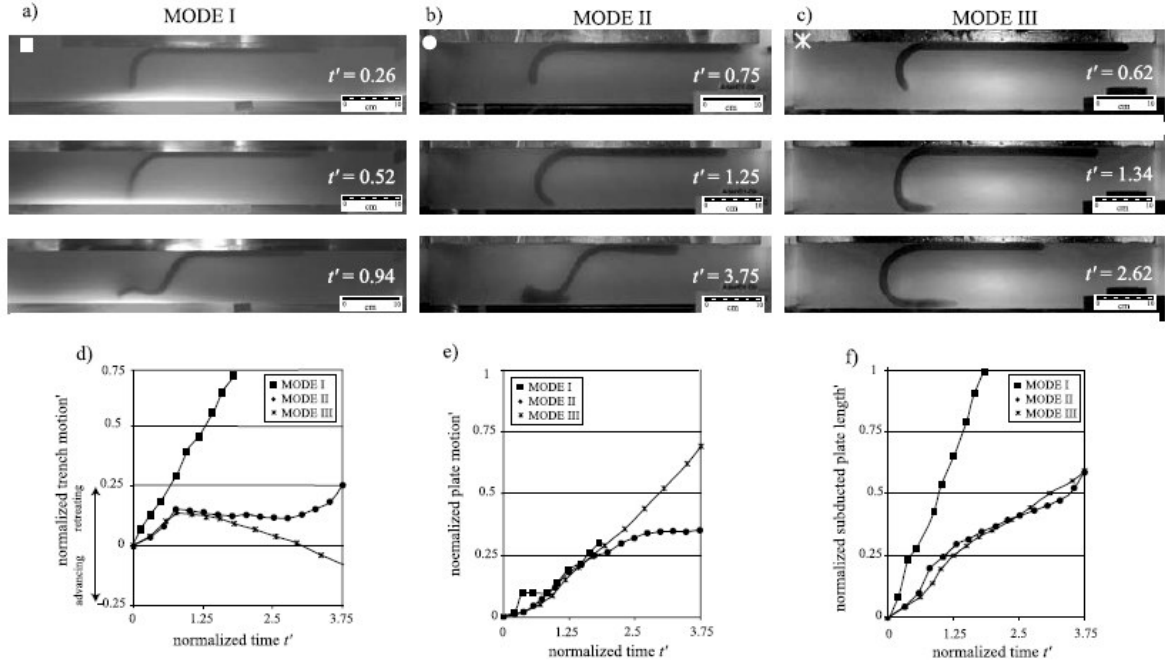tage; and (c) mode III, advancing trench mode. (d) Normalized trench motion measured in the three experiments presented versus normalized time. (e) Normalized plate motion versus normalized time. (f) Normalized subducted plate length versus normalized time [Bellahsen et al., 2006].

One of the most recent study of analogue subduction, fruitfully constrained by statistical data from natural cases, is proposed by Heuret and coworkers [2007]. They highlighted the way trench migration, overriding plate deformation and slab shape are related to the subducting- and overriding-plate kinematics. The analogue models - setup using silicone puttyfor the lithosphere and syrup for the mantle - allowed to systematically vary the subducting and overriding plate velocities exploring the variability of natural plate kinematics. Results recognized the importance of overriding plate motion on controlling the subduction process. In particular, they found that trenches migrate at a rate close to the overriding plate motion, the overriding plate shortens if it moves towards the trench and that both shallow and steeps dip are found if the overriding plate moves toward and away from the trench respectively.
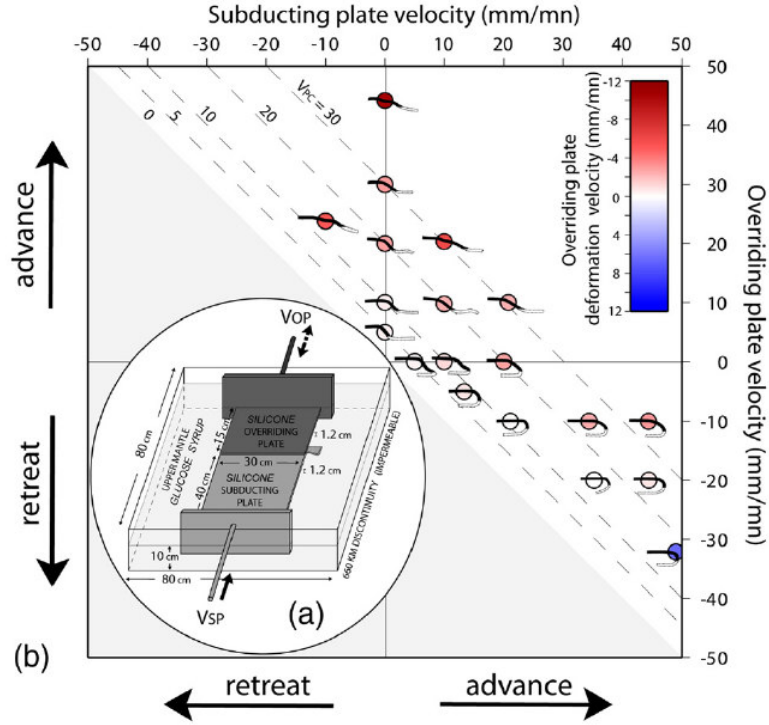
Figure 6: a) Experimental setup. The bottom of the box is impermeable. It mimics the 660 km discontinuity. b) Relations between the plate kinematics, the slab shape and the overriding plate deformation style of the performed experiments in a V_{SP}/V_{OP} space. Dot color refers to the overriding plate shortening rate. In each model, the shape of the slab is drawn when a total amount of 25 cm of silicone plate is subducted [Heuret et al., 2007].

Hence, the upper plate and, in turn, the coupling between subducting and overriding plates, seems to have a critical effect in tuning the experimental behaviour of subduction zones. However, so far the possible role played by lateral variations in the properties of the plate interface has been not experimentally approached despite numerical models are demonstrating the importance of the upper plates strength in controlling the long-term evolution of subduction zones and strain accommodation in the upper plates [Capitanio et al., 2010].

With the aim to fill this gap, I investigate in this thesis (Chapter 3) the long-term role of coupling (defined as a resistive force exerted on the subducting- overriding plate boundary) at convergent margins using analogue models of subduction. The setup is similar to Heuret et al., (2007) but includes lateral variation of coupling along the plate interface. In particular, as extensively described in Chapter 3, I try to link and dynamically explain relationships between trench shape, upper plate shortening/uplift and plate interface coupling.

2.4.2 Analogue models of earthquakes

An earthquake is the result of an elastic energy release caused by a failure of frictional strength on a fault plane. Over the years there have been many ways to model earthquakes. They can be schematically listed as: (i) analogue models [e.g. Brune, 1996, Roseau et al., 2009], (ii) analytical [e.g. Lin and Stein, 2004] and (iii) numerical models [e.g. Zheng et al., 1996; Wang, 2007].

Analogue models of earthquakes are useful to study problems such as parameters influencing the frictional behavior [e.g. Rubio and Galeano 1994; Baumberger et al. 2003; Voisin et al., 2008] and rupture dynamics [e.g. Xia et al., 2004; Lykotrafitis et al., 2006]. Depending on the goal to achieve modelers choose different experimental setup and material to perform their experiments. Rice, foam rubber, gelatin, Bristol paper are all used as analogue of deforming, potentially seismogenic rocks. Despite the inherent limitations of scaling laboratory models to the prototype, experimental models provide important insight and constraints for seismicity. As a rule of thumb, for determining if a model is acceptable is important to test if experimental results follow the Gutenberg-Richter law [Gutemberg and Richter, 1944]. According to the Gutenberg-Richter events of different size are characterized by different temporal cycles [see paper by Vargas et al., 2008 for simple spring-block system and Hanks, 1979; Andrews, 1980; Aki, 198; Pacheco et al., 1992].

Since the pioneer work of Burridge-Knopoff model (1967), one of the most common procedure for studying the earthquake dynamic is through spring-block models. The potentiality of spring-block models consists in reproducing the stick-slip dynamics. Stick-slip is a particular style of motion that occurs when two solids - in contact and driven at constant speed- show oscillations that essentially involve a "stick" phase associated with elastic loading of the system, and a sudden "slip" corresponding to stress relaxation [Baumberger et., al. 1994]. Stick-slip occurs in many systems and has been claimed to be a basic component of earthquakes [e.g. Brace and Byerlee,

1966]. The standard mechanism for stick-slip involves a static threshold (force necessary to start motion), that is larger than the force of friction during sliding. This weakening of sliding resistance may result in a dynamic instability that depends on "*a–b*". This parameter is known as state and rate friction and describes the variations in dynamic friction coefficient with a change in slip velocity. Conditions to describe the stability of a system are a) *a-b* > 0 velocity-strengthening behaviour, which is intrinsically stable (no earthquake can nucleate in this field); b*) a-b* < 0, the frictional strength decreases with increasing slip velocity (velocity weakening behavior) resulting in a slip instability associated earthquakes [e.g. Scholz, 1998; see Chapter 5 for application to spring-block models].

One of the most relevant study on friction stability were performed using simple Bristol board spring-block models by Baumberger et al. [1994]. They demonstrated that the characteristics of frictional sliding depend on mass, driving velocity and stiffness of the driving spring constant and that a bifurcation from stick-slip to stable sliding occurs with increasing velocity (see figure 2).
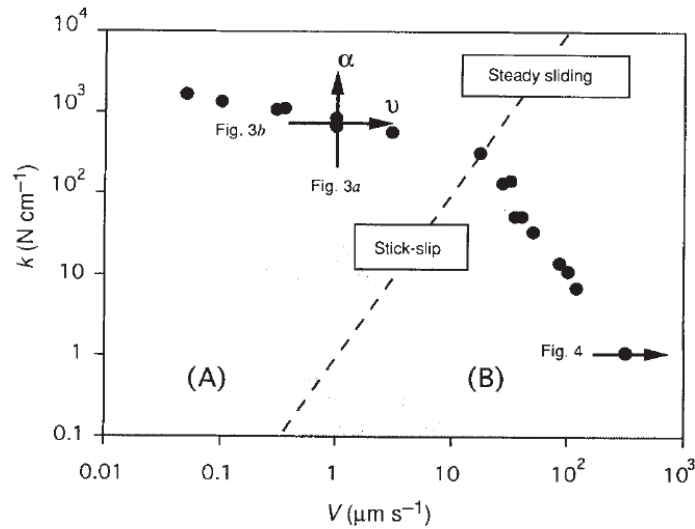

Figure 7: log-log plot in the *V-k* plane of the bifurcation curve (black dots). Sliding is stable above the curve whereas stick-slip oscillations occur below the curve [Baumberger et al., 1994].

Spring-block models are also useful for investigating the influence of cumulative displacement on frictional behavior. Voisin et al. [2007] demonstrated that a salt slider (which is used as analogue for natural faults deforming in the brittle and ductile regimes) experiences a continuous variation of the slip pattern from regular stick slip to continuous sliding accompanied by the change in the contact interface geometry with cumulative displacement [Voisin et al., 2007]. This result of general relevance, even if poorly constrained in terms of rate- and state- friction, allowed the Authors to speculate about the evolution of slip patterns along subduction zones with consequences on "unusual" slow earthquakes and non volcanic tremors [Voisin et al., 2008].

Another intriguing potentiality of analogue modeling consists in the study the dynamic of rupture. Two different models of rupture exist for the upper crust a) the *crack model,* where the nucleation region slips throughout the quake and the slipping region expands until rupture stops (e.g. the entire fault plane slips simultaneously); b) the *pulse model,* where only a small portion of the total fault area slips at any one time and only at the end of the quake all points on the rupture plane exhibit identical slip histories [Marone and Richardson, 2006]. Distinguishing between the two models is important for hazard assessment because they predict different degrees of strong shaking. Laboratory models can give insights on which of two models is better at explaining how Earth's crust ruptures during the occurrence of earthquakes.

Lykotrafitis and co-workers [2006], sheared two blocks of photoelastic plexiglass-like material (Homalite) in frictional contact in a dynamic impact apparatus and monitored rupture propagation with high-speed photography. They show that the rupture propagation mode varies systematically with the strength of initial forcing (produced by impact speed). Pulse-like ruptures are favored by slower impact speeds relative to those for crack-like ruptures. Also, the frictional slip velocity during rupture is lower for pulse-like ruptures than for crack-like ruptures. Despite the application of these experimental results to geologic materials and field observations is still far, they provide useful information on physical processes that govern dynamic rupture nucleation, growth, and arrest.
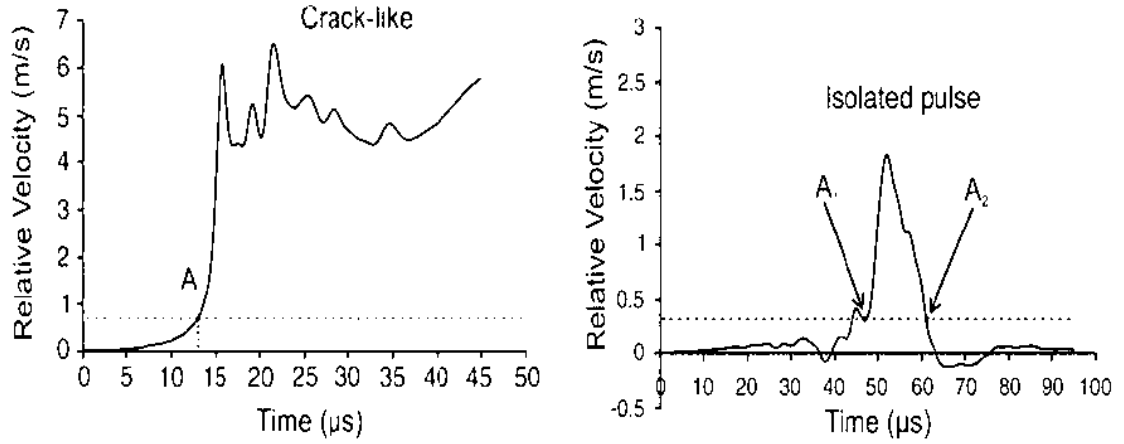
Figure 8: Relative velocity history of two points oppositely facing the slipping surface. Depending on the initial forcing two propagation mode occur in a sheared Homalite interface [Lykotrafitis et al., 2006].

Baumberger et al. [2008] investigated dynamical regimes and system stability of a simple spring-block system depending on the driving velocity. They found that, using a gel/glass system, steady sliding occurs at high driving velocity while periodic stick-slip dynamics occurs at low velocity. The intriguing point is that in the stick-slip regime, slip is inhomogeneous and occurs via the propagation of self healing pulses nucleated periodically at the trailing edge of the gelatin block.
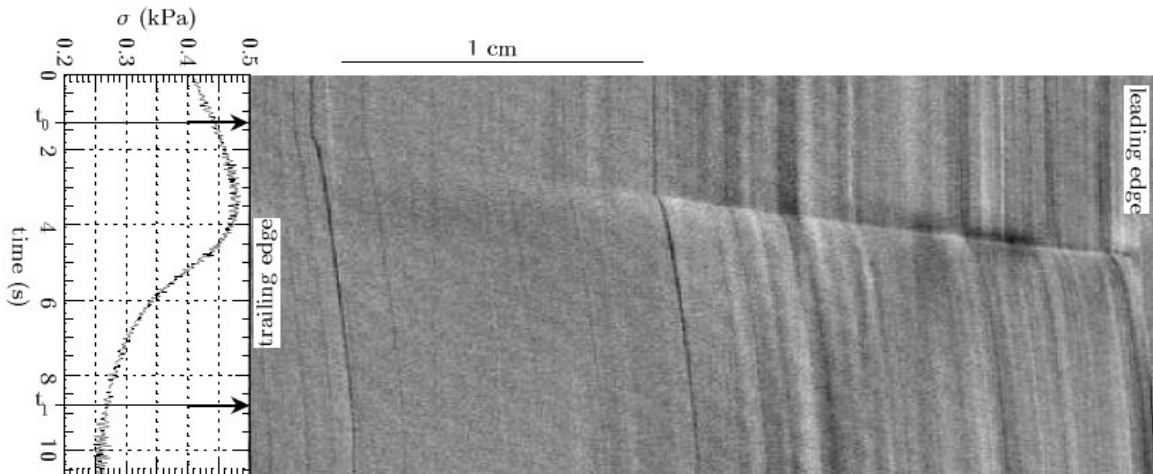
Figure 9: Spatio-temporal diagram of interfacial motion in the stick-slip regime, with time going down, and the gel driven to the right. Dark lines correspond to the trajectories of imperfections attached to the gel surface. For $t < t_0$, they are immobile, and the gel is stuck. At t_0, the trailing edge begins to slide, and sliding propagates along the interface. t_1

marks the beginning of resticking. The curve on the left shows the average shear stress measured simultaneously [Baumberger, et al., 2008].

The high potentiality of previously described experiment is unfortunately diminished by poorly constrained scaling. The general modelers approach is to use a certain material just because "it works" or "it allows to see something". This explains the difficulty to export experimantal results to natural cases and, consequently, to efficiently interact with the seismological community. As discussed in Chapter 2.2.1, in order to produce a "realistic" analog of earthquakes the model should be geometrically, kinematically, dynamically and rheologically similar to the prototype [e.g. Hubbert, 1937; Ramberg, 1981], which means including properly scaled complex rheology and friction into the experimental "ingredients".

The first example to this new models has been recently introduced by Rosenau et al. [2009]. Rosenau et al. [2009] investigated the elastoplastic megathrust earthquake cycles using a new analogue model featuring rate- and state-dependent elastic-frictional plastic and viscoelastic material properties scaled for gravity, inertia, elasticity, friction, and viscosity. Combining elastic dislocation numerical models to analogue results they highlighted the accumulation of permanent deformations during several seismic cycles. Experimental results demonstrate how strain localization at the rupture peripheries may lead to a seismotectonically segmented forearc, including a tectonically stable shelf and coastal high. Also, this new methodology allowed to speculate about link between fore-arc deformation and frequency-size distribution of megathrust earthquakes in subduction zones [Rosenau & Onken, 2009] which is standing out as one of the most intriguing question in geodynamics.

Further steps can be done in laboratory modeling of subduction thrust type earthquakes combining an extensive scaling study and material research with the state of art of stress and strain rate visualization tools aiming to systematically exploring cause-effect relationships of the key

ingredients of subduction zones seismicity (e.g. subducting plate roughness or velocity). This is one of the goals of this Thesis (see Chapter 5 and 6).

Chapter 3

Varying mechanical coupling along the central Andes: implications for trench curvature, shortening, and topography

Abstract

The Andean system, where the Nazca plate undergoes continental South America, is often regarded as the archetype of convergent margin where spatial and temporal correlations between the development of trench curvature, shortening of the overriding plate, and uplift of topography stand out from the geologic record. Despite the large amount of observations available, the details of those links are still matter of debate. There is, nevertheless, distinctive evidence suggesting that the degree of mechanical coupling between converging plates (i.e. the amount of resistive force mutually transmitted between plates and opposite to their direction of motions) may significantly vary along the Andean margin in the present-day situation. Here we present laboratory models of subduction performed to investigate quantitatively the role of the lateral variations of the mechanical coupling between converging plates in controlling the evolution of trench curvature, tectonic shortening, and the distribution of topography along the Andean margin. The analogue of a two-layer Newtonian lithosphere/upper mantle system is established in a silicone putty/glucose syrup tank-model. We find that the ability of the experimental overriding plate to slide above the subducting one is significantly inhibited by strong mechanical coupling. This inference applies in particular to the central Andean margin, where the overriding plate shortens more than elsewhere

along the margin, and the trench remains stationary as opposed to the advancing northern and southern limbs. Consequently, the margin evolves into the peculiar shape observed along the Andes in the present-day. The presence of the overriding plate and its laterally varying degree of coupling with the subducting unit impact the evolution of convergent systems perhaps more than previously thought.

3.1 Introduction

Subduction is a central process in Plate Tectonics [Morgan, 1968], whereby cold lithospheric plates sink into the Earth mantle along convergent margins, primarily driven by negative buoyancy [McKenzie, 1969]. However, a simple parameterization of the sole buoyancy term (i.e. slab-pull) often fails to explain even the observed temporal variations of convergence rates, globally reconstructed using paleomagnetic and geodetic data [e.g. Torsvik et al., 2010; Sella et al., 2002]. This indicates that other forces of resistive nature may contribute significantly to the momentum balance, influencing the not only the kinematics of the subducting system but also its geometry [e.g. Morra et al., 2006].

The Andean margin, where the Nazca plate plunges beneath continental South America, stands out as a prime example of subduction zone, characterized by a peculiar evolving curvature (Fig. 1). The trench extends from north to south for more than 40 degrees in latitude, and currently features a pronounced curvature that makes South America convex towards the Nazca plate. It appears clear from paleomagnetic and geodetic data that the shape is progressively being acquired through rotations that are clockwise to the south, and counter-clockwise to the north of the Bolivian Orocline [Allmendinger et al., 2005; Fig. 1]. Constraints on the temporal evolution of the curvature available from paleomagnetic studies of the Andean foreland indicate that North of the Bolivian Orocline rotations predate ~15 Ma, and become progressively younger as one moves northward

[Rousse et al, 2003]. Similarly, to the south Maffione et al. [2009] concluded that significant clockwise rotation occurred since 30-40 Ma. There is, however, no unique consensus on the time progression, and other studies plead for most of the curvature to have developed in the Eocene-Oligocene, with only minor rotation during the Neogene [e.g. Arriagada et al. 2008].

In addition to the available estimates of the temporal evolution of the curvature, constraints on the history of Andean uplift [Gregory-Wodzicki, 2000; Ghosh et al., 2006] to arrive at the present-day height and inland extension – i.e. topographic volume - (Fig. 1) have prompted to the community to agree that indeed most of the trench curvature developed because the central Andes experienced more crustal shortening in late Cenozoic compared to elsewhere along the margin, as originally proposed by Isacks [1988]. However, what geological process may simultaneously reconcile curvature of the margin, crustal shortening, and Andean uplift still stands today as a most intriguing question, to which various authors have proposed different answers. Molnar & Atwater [1978] argued that the thermal buoyancy of relatively young (less than ~50 Myr) oceanic lithosphere, as in the central portion of the Nazca plate [Mueller et al., 2008a], may not suffice to pull the slab readily into the mantle and, therefore, to generate broad deformation zones of the Andean type, calling for additional forces in place. Indeed a transition in material properties, and arguably in chemical buoyancy of young slabs has been recognized through joint bulk-sound and shear tomography [Gorbatov & Kennett, 2003]. Russo & Silver [1996] linked Andean deformation and shortening to mantle flow beneath the Nazca slab. Specifically, they resorted to shear-wave splitting observations and proposed that flow stagnation beneath central Nazca slab does not allow the latter to roll back as much as it does in the northern and southern margin. Schellart et al. [2009] revised this proposition, arguing that width of plates also has a role in determining the curvature of the margin. Lister & Forster [2009] have recently provided a general account that links slab roll-back and modes of orogeny. Another intriguing idea is represented by the possibility that climate-controlled sediment starvation of the central margin (Fig. 1) potentially increases friction and, in

turn, mechanical coupling locally focusing the stresses necessary to foster shortening and sustain uplift of the high Andean plateaus [Lamb & Davies, 2003].

The impact of properties and characteristics of the overriding plate on trench deformation has in the past been explored by taking advantage ofmodelling . As far as laboratory models is concerned, Mart et al. [2005] investigated the patterns of deformation arising from friction variations along the plate interface. Marques & Cobbold [2006], on the other hand, tested whether trench deformation may be related to increased deviatoric stresses arising from the thickened overriding plate during the orogeny. Recently, Boutelier & Oncken [2010] employed analytical and numerical models to show that a pre-existing, mild curvature of the margin is a necessary but not sufficient condition to the development of a high plateau. On a more fundamental level, this class of studies has linked trench deformation with variations of plate-interface mechanical coupling, which will be here intended as the amount of force that the plates mutually exert upon each other in the direction opposite to their motions. In that respect, laboratory and field data indicate that a change of either the friction coefficient or the horizontal deviatoric stress already impacts to similar degrees most of the mechanical coupling between plates (see supplementary information for more details).

In this study we take a step further and employ laboratory models of subduction [e.g. Funiciello et al., 2003] to quantitatively test whether trench curvature, upper-plate shortening, and possibly uplift in amounts comparable to the observations in the Andes may arise from lateral gradients of mechanical coupling. Our hypothesis stems from a variety of evidence supporting the emplacement of coupling variations along the Nazca/South America margin in late Cenozoic through either of the abovementioned mechanisms. The amount of sediments entering the trench has been recognized with the potential to lubricate the inter-plate area, effectively reducing the coefficient of friction [Kopf & Brown, 2003] and this mechanism already quaitatively proposed to tune upper-plate shortening and uplift of South America [Lamb and Davies, 2003].,On the same direction, Iaffaldano & Bunge [2006; 2009] proposed that the gravitational collapse associated with

the developing topographic volume of the central Andes may locally offset the horizontal deviatoric stress by ~50 MPa compared to the northern and southern margin. Such collapse is indeed capable of deflecting the subducting plate downwards along the trench [Iaffaldano & Bunge, 2008], as evident from sound and gravity surveys.
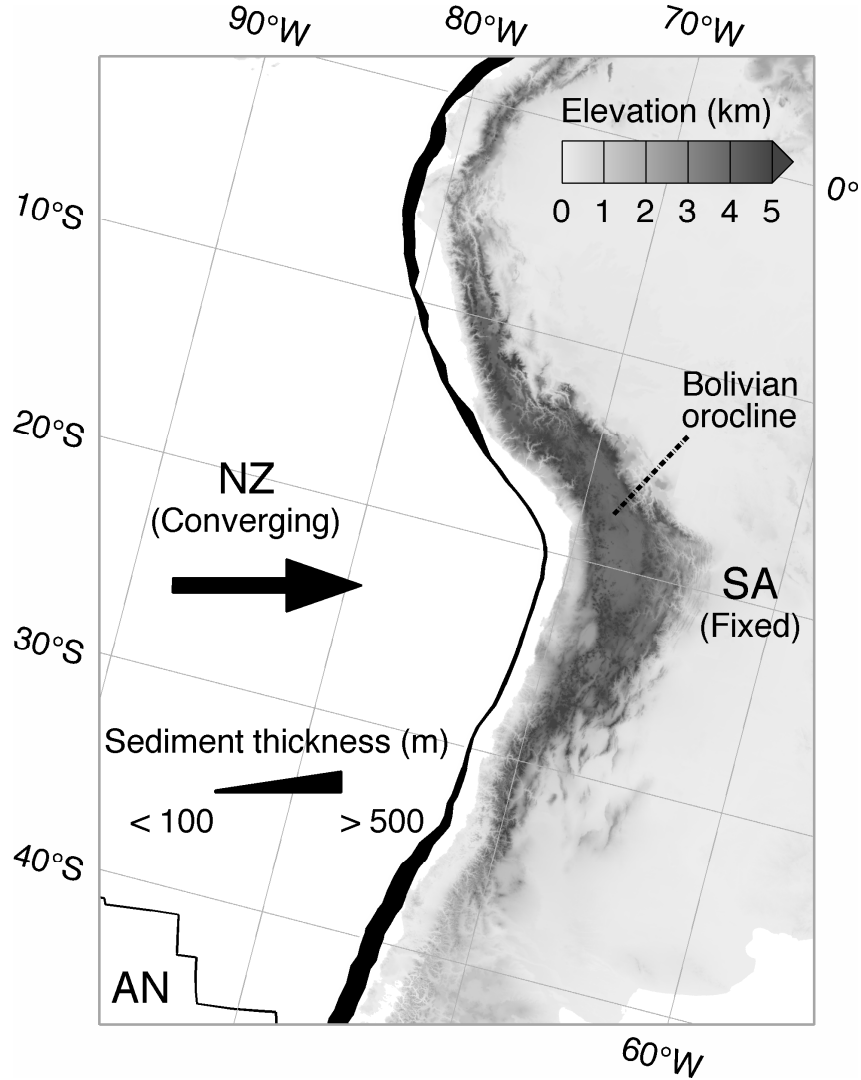
Figure 1: Tectonic setting of the Andean margin, where Nazca (NZ) converges towards South America (SA). Continental topography is in gray color-scale. Arrow indicates average convergence direction of NZ since 40 Ma, in a reference frame fixed with SA [Torsvik et al., 2010]. Thickness of the NZ/SA margin varies with the observed amount of sediments above the trench [National Geophysical Data Center - NOAA]. Other plate margins are in thin black. Note that the pronounced curvature of the convergent margin is symmetric with respect to the direction of convergence, the distribution of trench sediments, and the topographic volume of the Andes. AN – Antarctica.

3.2 Experimental results

We set up two analog models of oceanic subduction where a two-layer Newtonian lithosphere/upper mantle system is established into a silicon putty/glucose syrup tank-model (see the supplementary information for technical details). The conditions of mechanical coupling between plates are explicitly varied from one model to the other. In the first setting (mod#1) the central portion of the margin is more strongly coupled compared to the rest, where a lubricant paste has the effect of lubricating the interface. In the second model (mod #2) we instead maintain plate coupling at a uniform low level along the entire interface by leaving a channel of glucose syrup between the overriding and the subducting plates. Within the framework of our models and based on previous studies [e.g. Funiciello et al., 2003], we initially rank qualitatively the degree of coupling along the central margin in mod. 1 as high, while coupling along the lateral edges is ranked as average. By comparison, the uniform coupling in mod. 2 is ranked as low. A formal analysis of our results made *a posteriori* allows us to estimate the relative importance of plate coupling with respect to the driving force in each model (see supplementary information). We find that the highly-coupled central margin in mod. 1 experiences a resisting force amounting to ~37% of the driving force. Instead, resistance along the lateral edges in the same model is ~21% of the driving force. The convergent margin in mod. 2 experiences a resisting force as low as 5% of the driving one.

Results from our analog models are reported in Fig. 2 and 3. Panels A-D in each figure show the subducting system from a topside view at four different moments, from subduction initiation to the end of the model. The subducting plate undergoes the overriding one from left to right. The upper part of each panel is a half-view picture, while the lower part is a digital laser-acquisition of the other half, showing the relief of plates relative the beginning of the model. The last panel in Fig. 2 and 3 summarizes the temporal evolution of the lower half-trench shape, imaged through the

laser-scanning device. A comparison between the Fig. 2E and Fig. 3E shows that strong lateral variations of plate coupling are indeed capable to induce significant curvature of the trench, which evolves into a pronounced arc during the final 20-30 minutes of mod. 1. Based on the time-scale factor of our models (see supplementary information), this is equivalent to 20-30 Myr, and is thus compatible with estimates from paleomagnetic rotations along the Andean belt [Allmendinger et al., 2005]. Furthermore, note the development of topography on the overriding plate corresponding to the strongly coupled central margin (Fig. 2B, 2C, and 2D). We argue that the high degree of coupling efficiently works against the overriding plate motion so that deformation and local bulging occur. At the end of mod. 1 we observe a relief as high as 1.5-2 mm, equivalent to about 8-12 km in reality. This will also enforce, although minimally, the degree of coupling between converging plates by providing an additional offset to the horizontal deviatoric stress. Considering that erosive processes are not implemented in this type of analog models, and that no internal faults are available to distribute the topography laterally rather than vertically, we argue that the topographic volume obtained falls within an acceptable range for the high Andeas plateau.

On the contrary, mod. 2 (Fig. 3) indicates that the trench does not evolve into a curved arc if no lateral coupling gradients are in place. In fact, the original straight profile is preserved during the entire duration of the process, and no topography develops on the overriding plate (Fig. 3A-D). As all other parameters were kept similar between mod. 1 and 2, our results explicitly relate the curvature of convergent margins to lateral variations of mechanical coupling between subducting and overriding plates.

Figure 2: Laboratory model 1: analog subduction featuring variations of mechanical coupling along the plate interface (see text and supplementary information for details). Coupling variations are implemented through the presence/lack of lubricant paste on the subducting unit (see labels outlining lubricated regions). Panels A-D are snapshots of trench evolution; the elapsed time from model start is in the upper-right corner. The upper half of each panel is a picture of the plates, where 2 x 2 cm squares are outlined to detect deformation. The lower half is a laser-scanned image of plate relief acquired at the same moment. Relief is plotted as local offset from the initial relief at the beginning of the model. Note that the model plates are manually attached to the pistons, therefore the peripheral regions naturally bulge upwards or downwards, and are thus detected as anomalous. Panel E shows the evolution of half-trench through time, as detected through the laser-scanned images. Red on white is the portion of trench with no lubricant paste, hence featuring high coupling. Blue on gray is one of the lateral edges with lubricant paste, thus featuring average coupling (see text for details).
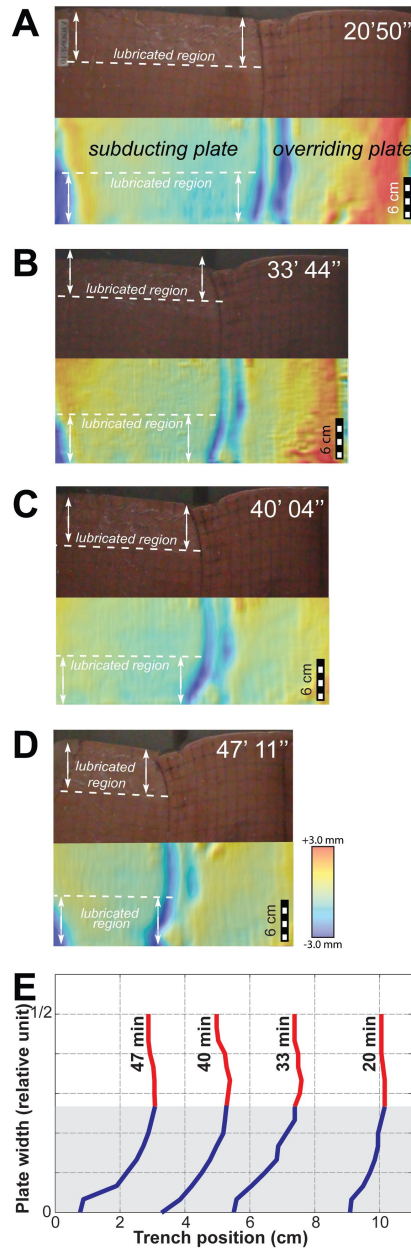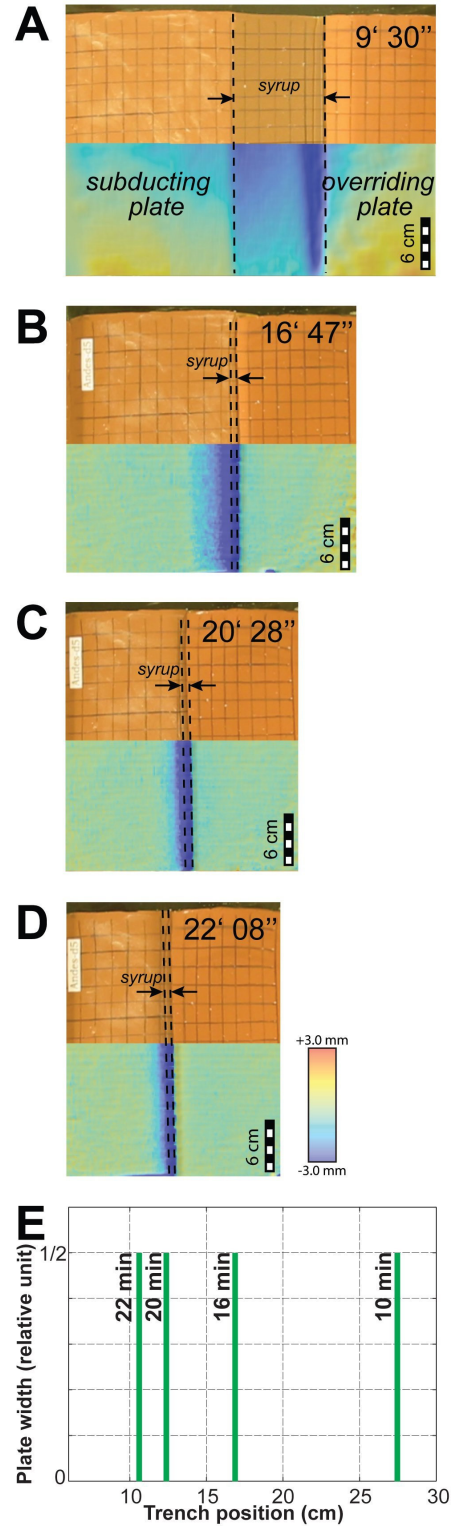
Figure 3: Laboratory model 2: analog subduction featuring uniformly low mechanical coupling along the plate interface (see text and supplementary information for details); the interface region with lubricating syrup is outlined in panels A-D. Images are equivalent to the ones in Fig. 3 (see label of Fig. 2 for details). A comparison of models 1 and 2 shows that the trench evolves into a pronounced curvature when lateral variations of coupling are emplaced. This is not observed when coupling is uniformly low along the entire plate interface.

3.3 Discussion and conclusions

In the ideal case of perfectly rigid plates, the shape of the trench would be prevented from undergoing any temporal variations, and mechanical coupling would only affect the rate of convergence between subducting and overriding units. In the more realistic case of non-rigid plates, it is therefore natural to relate the curvature of the trench to deformation, occurring particularly in the overriding plate. We detect horizontal deformation by means of 2 x 2 cm^2 squares, initially outlined on the upper surface of plates and compute the amount of shortening in the upper plate from the moment of subduction initiation. This allows us to verify the emplacement of lateral shortening gradients as origin for the pronounced curvature of the Andean margin. We collectively report these estimates from both models in Fig. 4A. Shortening has been measured separately in correspondence of the non-lubricated (high coupling) and lubricated (average coupling) portions of the trench in mod. 1; whereas we have verified that upper plate shortening in mod. 2 (low coupling) is consistently uniform along the trench (see upper-plate grid in Fig. 3A-D), therefore a single time-series is well representative of the entire margin. We find that the high degree of mechanical coupling in the central margin of mod. 1 causes the upper plate to shorten by as much as 4 cm by the time significant curvature and topography have developed (Fig. 4A – black dots). According to the characteristic length-scale factor of our models, this is equivalent to more than 240 km in nature. On the other hand, since the lateral edges of the upper plate feature an average degree of coupling, they only experience ~2.5 cm of shortening, equivalent to less than 180 km (Fig. 4A – white dots). We note that while deformation in our models is more diffuse since purely viscous rather than brittle, the equivalent shortening values compare well to field estimates along the Andean belt. In fact, it has been estimated that ~300 km of shortening are required to account for the topographic volume of the central Andes, but only ~150 km are needed in the northern and southern limbs [Klay & Monaldi, 1998; Hindle et al., 2005]. In comparison, very little shortening is detected in model 2, where the margin features uniform low coupling (Fig. 4A – triangles).

Our results explicitly link shortening, curvature and topography of the upper plate on one side, and lateral variations of mechanical coupling on the other. These links may be conveniently put in the framework of rates of horizontal deformation (Rd) and trench-advancement (Rt), which we report in Fig. 4B as fractions of the piston-velocity driving the overriding plate. In the presence of low mechanical coupling the upper plate deforms and shortens very slowly, because most of the driving velocity is transferred into advancement of the trench (Fig. 4B – triangle). As the degree of coupling along the plate interface increases, trench-advancement is progressively compromised in favor of shortening of the upper plate under compressive deformation (Fig. 4B – white and black dots). After a finite time interval, different amounts of trench-advancement along differently coupled portions of the trench will determine the latter to assume its pronounced curvature. Generally, for small amounts of deformation that the upper plate undergoes, the corresponding volume change will be small and virtually undetectable, implying Rd + Rt = 1 at all times. Within the accuracy of our estimates, this applies to all cases but one, where mechanical coupling is the highest (black dot in Fig. 4B). In this case the trench advances even less than what would be predicted based on the measured rate of horizontal deformation, implying the presence of additional, undetected deformation. The notion of continuity requires such an amount of deformation to concentrate along vertical planes, giving rise to topography of the upper plate (central margin in Fig. 2B-D).

To summarize, we have performed analog models of subduction specifically aimed at exploring the evolution of the Andean margin during late Cenozoic. We have systematically varied the mechanical coupling between converging plates, and found that the temporal evolution of trench curvature, shortening, and overriding-plate topography are significantly influenced by the degree of coupling along the local interface. Low mechanical coupling between converging plates implies little deformation and shortening of the overriding unit, whereas high coupling will locally inhibit the ability of the upper plate to override the subducting unit, forcing the former to shorten and eventually bulge upwards more than elsewhere. Those two scenarios represent the end-members of

a range that may be conveniently described in terms of trench-advancement and horizontal-deformation rates. The peculiar curvature of the Andean margin is therefore reconciled with shortening and topography of the upper plate if the central portion of the margin is more strongly coupled than the northern and southern limbs. Our results indicate that the presence of the overriding plate and its degree of coupling with the undergoing slab determine the evolution of convergent systems perhaps more than previously thought.

To our best knowledge it remains debated why shortening and orogeny in the Andes occurred mostly during the Cenozoic [Lamb & Davies, 2003; Montgomery et al., 2001], when subduction has been active since the late Jurassic [Mueller et al., 2008b]. Similarly, it is not straightforward to assess what curvature the margin featured at the time when significant shortening began. Lateral and temporal variations of inter-plate friction and local deviatoric stress may impact the total inter-plate strength and mechanical coupling to the same order of magnitude. However, it remains admittedly difficult to distinguish whether and when these mechanisms have been independently active, and possible feedbacks between them make the interpretation of the geologic record more challenging.
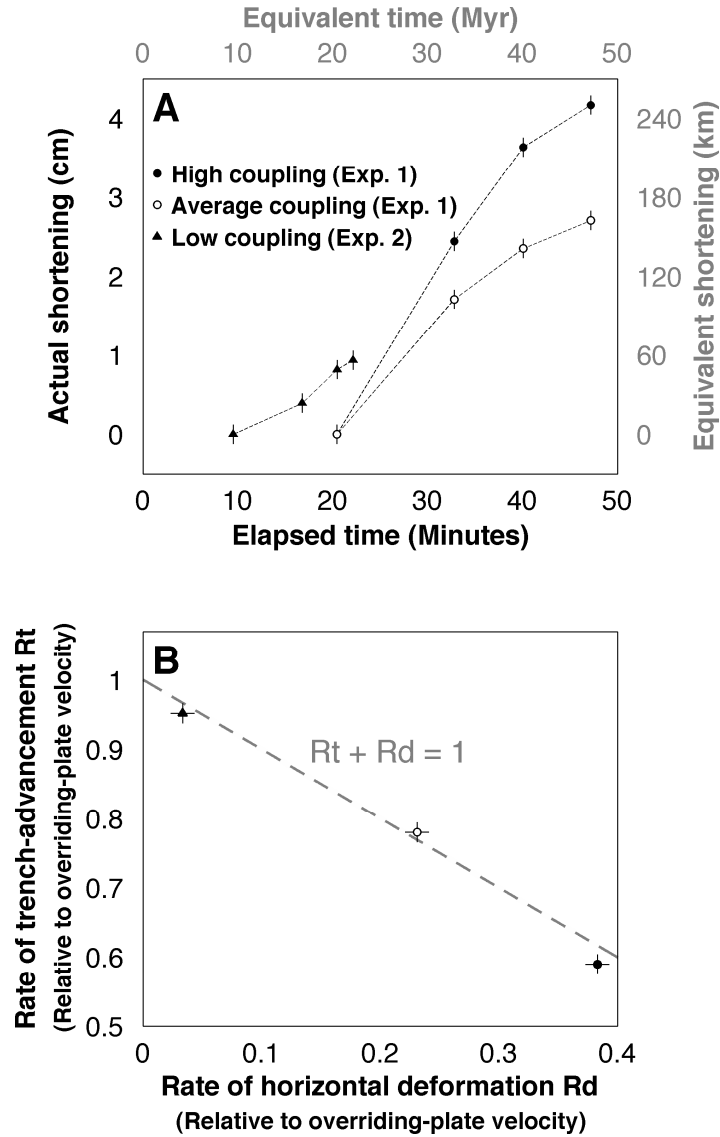
Figura 4: (A) Shortening of the overriding plate from our models. Shortening is measured from the progressive deformation of 2 x 2 cm squares outlined on the overriding plates, error-bars are also shown. Measures in model 1 were conducted distinctively across portions of the margin with (white dots) and without (black dots) lubricant paste. Shortening in model 2 has been verified to be uniform along the margin, and is therefore represented by a single time series (black triangles). Shortening increases with the increasing degree of mechanical coupling between converging plates (legend indicates our ranking of coupling – see text for details). Equivalent values of elapsed time and shortening are reported on the left- and top- side of the panel; for model 1 they compare well with available observations along the Andean belt. (B) Rate of trench-advancement (Rt) versus rate of horizontal deformation in the overriding-plate (Rd) from our models, reported as fraction of the piston velocity driving the overriding plate. Error-bars are also shown. As mechanical coupling increases, the ability of the trench to advance is progressively inhibited in favor of deformation of the overriding plate. In particular, different portions of the same trench in model 1 advance at different rates, and undergo different amounts of shortening (panel A). This results in the pronounced curvature of the trench at the end of the model. Small amounts of deformation in the overriding-plate result in Rt + Rd =1 (dashed gray line). The notion of continuity implies that any departure from there reflects the development of topography (see text for more details).

3.4 Supplementary information

3.4.1 Definition of mechanical coupling

Classically, the term 'coupling' has a pool of definitions that are not necessarily internally consistent, partly depending on the context under which they were originally formulated [Stein & Wysession 2003]. In this study mechanical coupling will be intended as the amount of force that plates mutually exert upon each other in the direction opposite of the respective motions. The high degree of symmetry between present-day curvature of the trench and the Nazca/South America convergence direction since 40 Ma (see Fig. 1 in the main text) gives us confidence that the definition we adopt is appropriate, at least within the Andean framework.

In the context of converging plates mechanical coupling is associated with forces opposing convergence, and with the resistive strength emplaced along the margin. It should be straightforward to argue for most of the strength to be located in the upper plate boundary. In fact, laboratory experiments of rock failure and flow [Kohlstedt et al., 1995; Karato & Jung, 2003] indicate that the brittle portion of plate boundaries contains most of the total strength, whereas very little strength resides deeper than the brittle-ductile transition (Fig. SF1). There are thus only two independent ways to control most of the strength along convergent margins: (1) by changing either the slope or (2) the intercept of the linear portion of the envelope. These ways correspond to vary either the inter-plate friction coefficient or the background deviatoric stress (see Fig. SF2). Furthermore within the ranges of rheological parameters typical of Plate Tectonics [Kohlstedt et al., 1995; Karato & Jung, 2003; Suppe, 2007], both mechanisms yield variations of the mechanical coupling of the same order of magnitude (Fig. SF2).
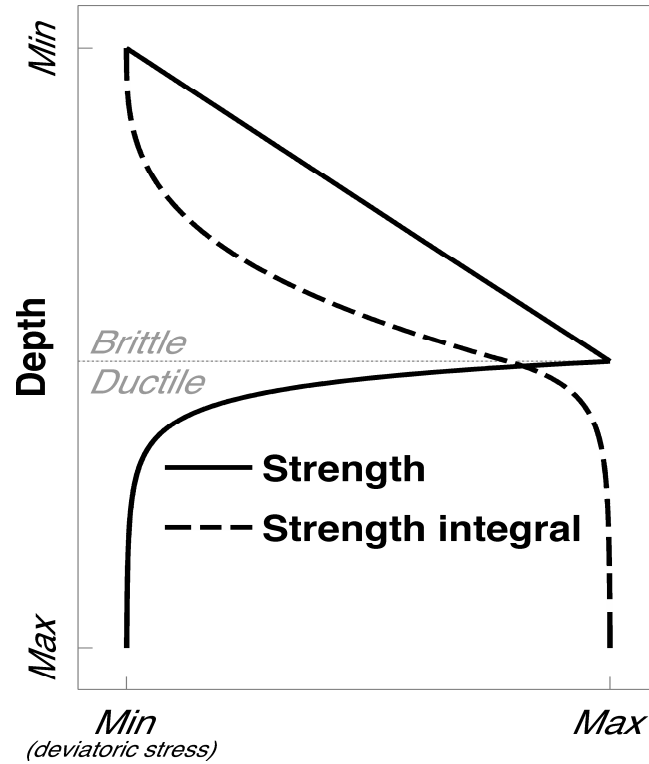
Figure SF 1: Sketch of lithosphere strength (solid line), inferred from laboratory experiments of rock failure and flow. In the upper lithosphere the regime is brittle, and strength increases linearly with the overburden pressure. In the lower part the regime is ductile, and strength decreases exponentially with increasing temperature. The dashed line is the strength integral to a given depth, and shows that the brittle portion of the lithosphere hosts 70-80% of the total strength. This inference holds within the ranges of rheologic parameters typical of Plate Tectonics.
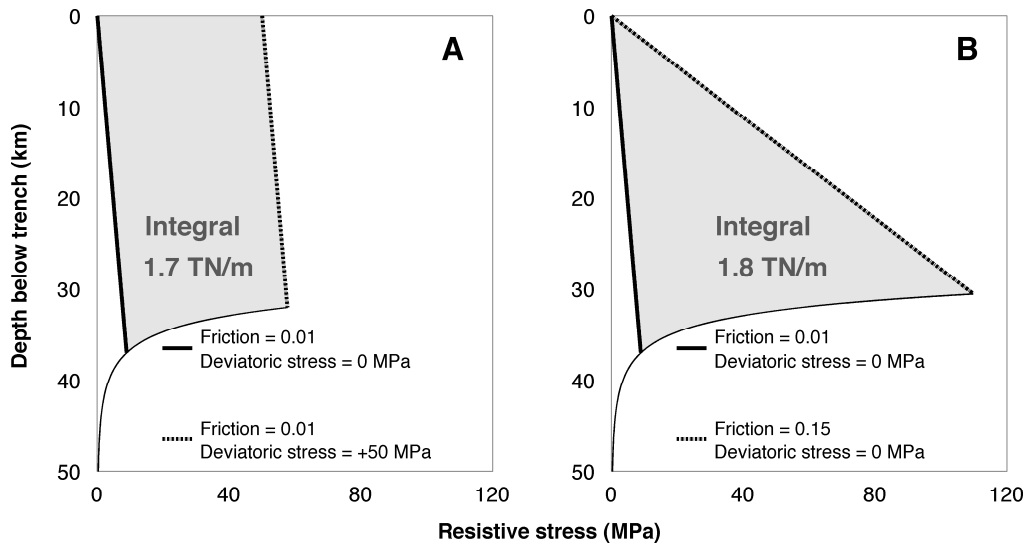
Figure SF2: Variation of mechanical coupling following a change of (A) horizontal deviatoric stress or (B) friction coefficient. Variation is computed as depth-integral of the difference between strength profiles corresponding to varying friction or deviatoric stress conditions. Note that the values of friction coefficients represents the end-members of the typical range valid for Plate Tectonics. 50 MPa is the deviatoric stress arising from a crustal relief of ~2 Km.

3.4.2 Models of analog subduction

We set up laboratory models of subduction, where overriding and subducting plates are simulated by means of two types of silicon putty, featuring different density and viscosity values. To model the subducting oceanic plate we employ silicon putty of density rho_sp = 1510 kg*m^-3, and viscosity mu_sp = 3.7*10^5 Pa*s. The overriding continental plate is instead set to have density rho_op = 1380 kg*m^-3, and viscosity mu_op = 3.0*10^5 Pa*s. Plates lay initially flat on a layer of low-viscosity glucose syrup (rho_m = 1430 kg*m^-3, and viscosity mu_m = 82 Pa*s) simulating the upper mantle (Fig. SF3). Models are carried out at room temperature, and we have verified that the rheological regime of plates and mantle are purely Newtonian. The particular rheological parameters we chose have been previously widely discussed [Funiciello et al., 2003], and imply that models scale to nature as follows: 1 cm corresponds to 60 km (length-scale factor h_l = 1.67*10^-7) and . 60 s correspond to 1 Myr (time-scale factor h_t = 1.9*10^-12), in laboratory and nature respectevely. In the adopted setup plates are 1 cm thick and 30 cm wide, whereas the mantle is 11 cm deep (Fig. SF3). These lengths are equivalent to a plate thickness of 60 km, a plate width of 1800 km, and a mantle as deep as the 660-km transition zone. The adopted setup minimizes possible boundary effects, since the distance between plate and box boundaries is lagrer than the thickness of the convective mantle [Funiciello et al., 2004, 2006]. Therefore the toroidal component of mantle circulation that will be excited at the plate edges during the experiment should not affect significantly the dynamics

In our models we let two pistons drive the subducting and overriding plates. At the beginning of each model, the oceanic lithosphere locates centrally to the tank, attached to piston A while the overriding plate lays on the opposite side attached to piston B, overlapping by ~2 cm on top of the oceanic plate (Fig. SF3). In order for subduction to operate spontaneously, we initially drive the oceanic plate towards the overriding plate through piston A at a velocity as low as v_a = 1.6*10^-3

cm*s^-1 – equivalent to 0.6 cm*yr^-1 – and stop piston A only when the slab starts sinking into the model mantle under its own weight. Once subduction proceeds naturally under the effect of buoyancy, we let piston B drive continuously the overriding plate at a velocity v_b in range [8.3-27.5]*10^-3 cm*s^-1 – equivalent to [3-10] cm*yr^-1. Modelling evolution have been recorded by taking pictures from the topside and laser-scanning to monitor the evolution of plate relief during the process. Furthermore, 2 x 2 cm^2 black squares painted on top of both plates (see Fig. 2 and 3 in the main text) allowed detecting deformation and shortening of plates.

We run two subduction experiments where conditions of mechanical coupling between plates significantly vary from one to the other. In one model the central portion of the margin is more strongly coupled compared to the rest (in the main text we refer to this model as mod. 1). Specifically, we implement strong lateral variations of mechanical coupling by distributing lubricant paste (Vaseline) along the lateral edges of the subducting plate. Each lubricated segment is about 1/4 of the total plate width (Fig. SF3) and equivalent to ~500 km, while the central portion of the plate interface is left without any lubricant. In the second model we instead maintain plate coupling uniformly low along the entire interface by leaving a channel of glucose syrup between the overriding and the subducting plates (in the main text we refer to this model as mod. 2).
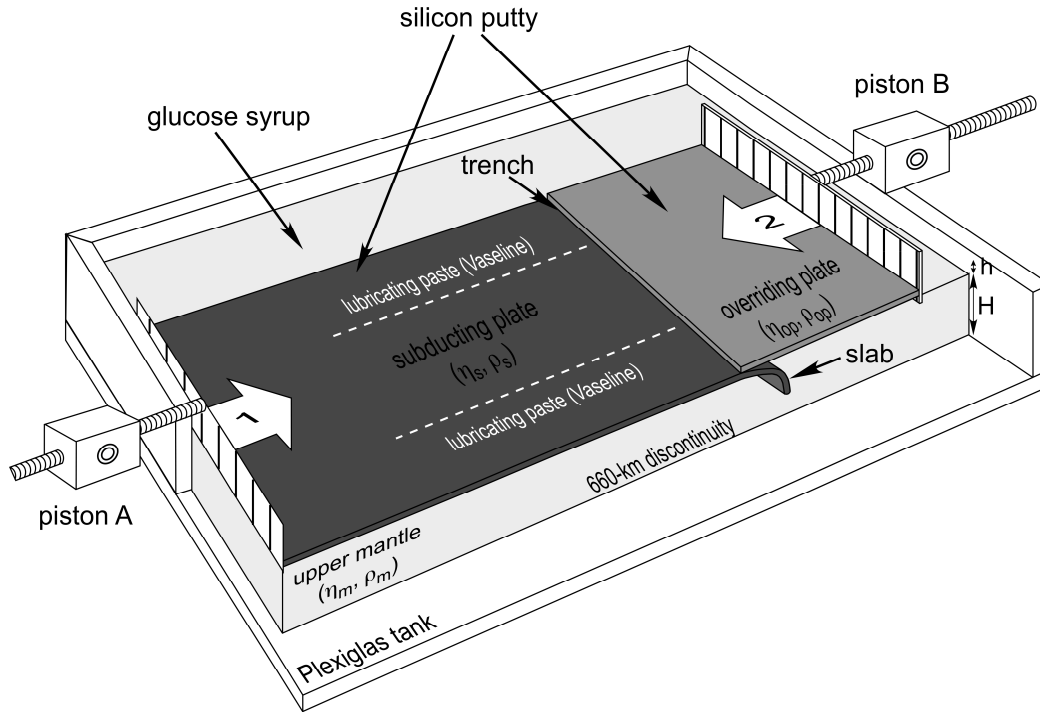
Figure SF3: Schematics of the 3D model set-up used in this study. In order to test the effect of lateral variations of plate coupling on the curvature of the trench, we perform a first model where we cover left and right portions of the subducting plate with lubricating paste, and leave its central portion clean (see white labels on the subducting plate. White dashed segments indicated transition between areas with/without vaseline). As subduction goes on in our models, plates experience persistent lateral variations in coupling due to the presence of lubricant along the lateral edges of their interface, and the absence of the same in the central interface. Results from this set-up are compared to a second model, where no paste is used. Rather we lubricate the entire interface with a layer of glucose syrup, to obtain a uniform low coupling between plates.

3.4.3 Estimates *a posteriori* of trench resistance in models of analog subduction

Within the framework of our analog models, we initially rank the degree coupling along the central margin in mod. 1 as high, while coupling along the lateral edges ranks as average. By comparison, uniform coupling in mod. 2 is ranked as low (see main text). A more precise estimate of the relative importance of resistance along the trench with respect to the driving force in our models may be obtained a posteriori from the trench-velocity measured in our models.

With reference to Fig. SF4, let $\vec{D}$ be the driving force pushing an ideal, perfectly rigid plate on one side. Let also $\vec{R}$ be the resisting force applied on the opposite side, oriented as $\vec{D}$, but acting in the opposite direction. $\vec{VR}$ is the viscous resistance from the fluid underneath that will act at the base of the plate as soon as this begins to move, and is therefore also oriented as the other forces. We will also assume that in general $R < D$ (where letters identify the magnitude of the corresponding vector). By comparing the orientation of forces with our analog models, we imagine that the trench is locates on the left-hand side of the plate (t in Fig. SF4). When a steady state is achieved, the vector equation of momentum balance for the center of mass is

(1) $\vec{D} + \vec{VR} + \vec{R} = 0$

For the sake of simplicity, we also assume that the plate is sufficiently thin that all forces lie on the same imaginary plane, so that the plate is prevented from spinning. Since $\vec{R}$ acts in the direction opposite to $\vec{D}$, eq. (1) corresponds to one scalar equation along the direction of all forces

(2) $D = R + VR$

When the fluid beneath the plate is at rest, the strain rate will be proportional to the velocity of the plate $\vec{v}$. Therefore eq. (2) becomes

(3) $D = R + \alpha \cdot v$

Where α has dimension of a viscosity times length. Being the plate perfectly rigid, the velocity that satisfies eq. (3) applies throughout the plate. Note that if $R = 0$ only the viscous resistance acts against the driving force, and the velocity of the plate will be directed as D, with magnitude

$$(4) \qquad v_0 = \frac{D}{\alpha}$$

where the subscript indicates no side resistance. When $0 < R < D$, the velocity resulting from eq. (3) will be still directed as D and have magnitude

$$(5) \qquad v = \frac{D - R}{\alpha} = v_0 - \frac{R}{\alpha} = v_0 \cdot \left[1 - \frac{R}{\alpha \cdot v_0} \right] = v_0 \cdot \left[1 - \frac{R}{D} \right]$$

If D is kept constant, Fig. SF5 shows a plot of v as function of R. In the more realistic case of a non-rigid plate, internal deformation should be also taken into account, and the velocity of the plate can no longer be described by means of one single vector. In the particular case at hand deformation will be compressive along the direction of all forces, and the velocity at the tip t where $\vec{R}$ acts ($\vec{v_t}$), i.e. at the trench, will be in general smaller in magnitude that the velocity of an ideally rigid plate.

For small deformations, we may arguably obtain an expression for the magnitude of $\vec{v_t}$ by perturbing eq. (5) as follows

$$(6) \qquad v_t = v_0 \cdot \left[1 - \beta \cdot \frac{R}{D} \right]$$

where β is a constant strictly larger than 1. In fact, $\beta = 1$ describes the velocity of a perfectly rigid plate. Fig. SF5 shows v_t as a function of R for two values of β, when D is kept constant. Note that eq. (6) satisfies the requirement of v_t being smaller than v for any value of $0 < R < D$. Finally, we may write v_t as fraction of v_0

$$(7) \qquad v_t = \gamma \cdot v_0 = v_0 \cdot \left[1 - \beta \cdot \frac{R}{D} \right]$$

we obtain

$$(8) \qquad \frac{R}{D} = \frac{1-\gamma}{\beta}$$

where $0 \leq \gamma < 1$.

In the context of our models, we have measured the ratio between trench-velocity and overriding-plate velocity, i.e. the coefficient γ (see Fig. 4B in the main text). We can use then use these measurements to estimate the relative importance of R with respect to D from eq. (8) (Fig. SF5). Taking $1 < \beta \leq 1.2$, we find that what the central margin of mod. 1, which we had initially ranked as high coupling, in fact experiences a resisting force amounting to ~37% of the driving force. Instead, resistance along the lateral edges in the same model is ~21% of the driving force. The convergent margin in mod. 2 experiences a resisting force as low as 5% of the driving one.
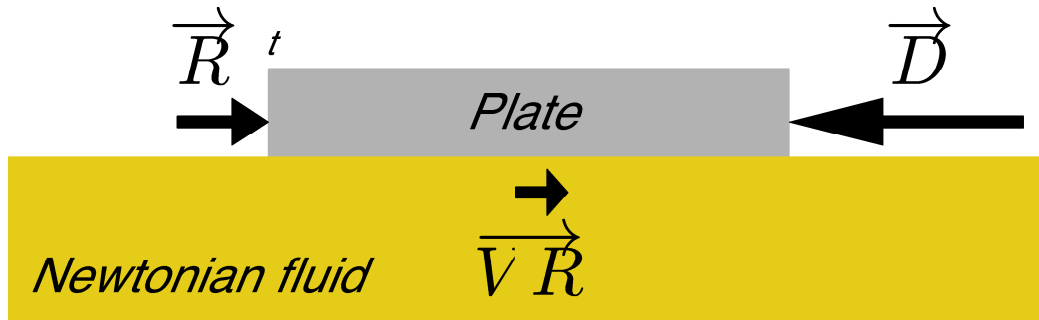
Figure SF4: Sketch of a rigid plate on top of a Newtonian fluid at rest.
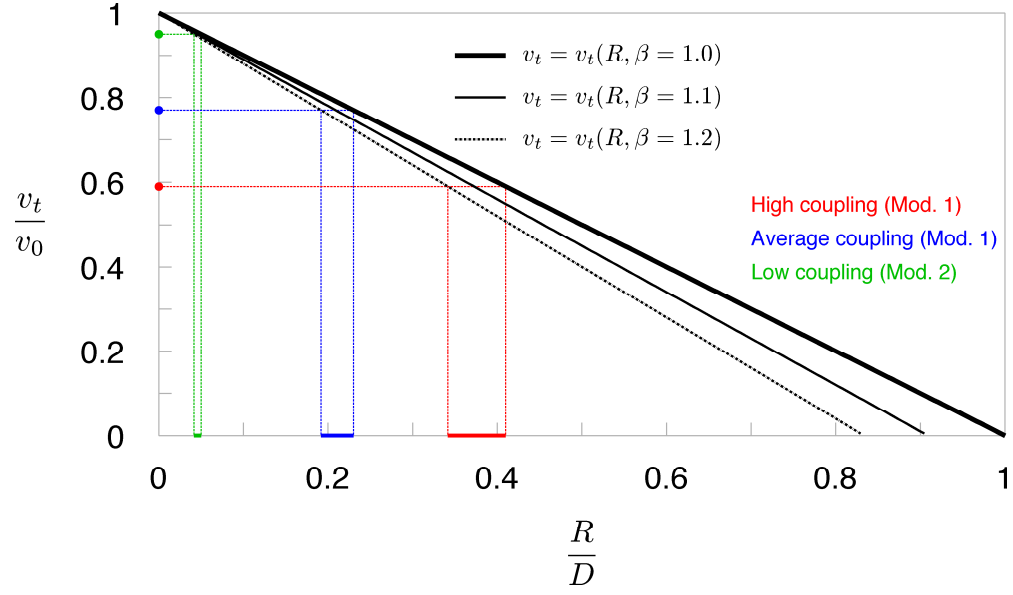
Figure SF5: In black we plot the trench-velocity (units relative to rigid-plate velocity) as a function of the magnitude of the resisting force (units relative to the driving one). Black bold line represents the case of a perfectly rigid plate ($\beta=1.0$). Black thin line is the case of a non-rigid plate, obtained by perturbing the velocity solution through a coefficient $\beta=1.1$. Black dashed line is the same case, for $\beta=1.2$. Bold color lines on the horizontal axis are the range of resistance (units relative to the driving one) in place along the trench of our analog models, according to the measured trench-velocity.

Chapter 4

Gelatins as rock analogs: a systematic study of their

rheological and physical properties

Abstract

In a laboratory model the behavior of the selected analog material must be properly scaled to nature. Here, we systematically investigate both rheological and physical properties of a wide range of gelatins as functions of temperature, composition, concentration, ageing and applied strain rate. Results show that gelatins' behavior changes gradually from purely elastic to visco-elasto-brittle to purely viscous (nonlinear) rheology going from the gel- to the sol-state. The rheological variability of gelatins appears promising for the potential use of these analog materials to simulate crustal and lithospheric rheological behavior. In particular, we found that pig skin 2.5 %wt at 10°C has the required rheological properties for a suitable experimental set-up to model crustal deformation.

4.1 Introduction

An analog model is a simplified dynamic representation of the Earth. According to 'similarity criteria', the rheological and physical parameters in the model must be properly scaled to natural conditions [e.g. Weijermars and Schmeling, 1986]. Analog models commonly use granular materials to simulate frictional Mohr-Coulomb plasticity [e.g. Hubbert, 1951; Ramberg, 1981; Davy and Cobbold, 1988, 1991; Krantz, 1991; Weijermars et al., 1993; Storti & McClay, 1995] and bouncing putties, paraffin waxes and glucose syrups to simulate ductile creep [e.g. Ramberg, 1955;

Davy and Cobbold, 1991; Brun et al, 1994; Shemenda, 1994; Griffiths et al., 1995; Grujic and Mancktelow, 1995; Davaille, 1999; Funiciello et al., 2003]. The predictive power of this methodology may be limited by a) the limited range of available materials properly scaling the behavior of the Earth; b) simplified rheologies and c) the necessity to use different experimental materials to simulate any rheological stratification in nature. Hence, a key requirement toward the improvement of this technique is the selection and calibration of suitable analog materials able to reproduce the complex rheological behavior of rocks. However, analog material knowledge is often restricted to the analysis of few physical parameters [e.g. Weijermars, 1986; Mancktelow, 1988; Cobbold and Jackson, 1992; Rossetti et al, 1999; Schellart 2000; Galland et al. 2006]. Only recently, ten Grotenhuis et al. [2002] and Boutelier et al. [2008] adopted an approach commonly used in Material Science for complete rheological characterization of materials and applied it to plasticines. Rheological behavior can be completely described by measuring the energy stored in the sample during deformation and the energy lost afterwards [Mezger, 2002]. These two quantities are expressed by the storage (G') and the loss (G'') moduli, determined over a broad range of deformation rates [Nelson and Dealy, 1993].

In this paper, we adopt the same rheometric approach to perform an extensive study of the properties of a wide range of gelatins, including those commonly used in laboratory modeling. Usually, gelatins are assumed to have a simple elastic-brittle rheology. Hence, their use has been limited to models of shallow crustal processes such as propagation of dykes [Fiske and Jackson, 1972; McGuire and Pullen, 1989; Takada, 1990, 1994; Koyaguchi and Takada, 1994; Lister and Kerr, 1991; McLeod and Tait, 1999; Bons et al., 2001; Ito and Martel, 2002; Walter and Troll, 2003; Pasquare' and Tibaldi, 2003; Acocella and Tibaldi, 2005; Watanabe et al., 1999, 2002; Menand and Tait, 2002], emplacement of laccoliths [Pollard and Johnson, 1973; Johnson and Pollard, 1973; Hyndman and Alt, 1987], formation of sills [Rivalta et al., 2005; Kavanagh et al, 2006], and bubble growth in soft sediments [Boudreau et al., 2005]. Most of these models provide

an insufficient scaling of the gelatins, with consequent limitations on the kinematic similarity. Despite their use as a brittle-elastic analog, gelatins show a more complex mechanical behavior, strongly dependent on temperature, composition, concentration, ageing and applied strain rate [Bot et al., 1996a, 1996b; Kavanagh and Ross-Murphy, 1998; Norziah et al., 2006; Barrangou et al., 2006]. In particular, gelatins show a visco-elasto-brittle rheology in their gel-state and a viscous rheology in their sol-state. This behavior has the twofold experimental advantage of: (i) reproducing the complex visco-elasto-brittle rheology representative of crustal/lithospheric behavior, until now simulated only by means of simplified rheologies; (ii) using a single material to model the Earth rheological structure, avoiding the use of different materials to simulate rheological layering. For these reasons, gelatins may represent a ground-breaking experimental material and a deeper knowledge of their rheological and physical parameters, as attempted in this study, is crucial for a proper modeling.

4.2 General properties of Gelatins

4.2.1 Composition

In Material Science, "gelatin" is the ordinary name for particular biopolymers. In this work, as usual in Earth Sciences literature, the term is used for both plant and animal biopolymers. They are naturally occurring long-chain polymers either composed of amino acids (peptides, polypeptides, proteins) or of saccharides (mono-, oligo-, and polysaccharides). Such macromolecules, available in tasteless and odorless powder form, are water diluted in small quantities and used in food production, pharmaceutics and oil recovery to achieve appropriate rheological properties, i.e. to improve texture, prevent drainage, increase viscosity and stability of foodstuffs.

4.2.2 Structure and mechanical behavior

Gelatins are constituted by flexible linear chain-like polymers assuming complex 3-dimensional structures. When these polymers are able to entangle forming a continuous network in the entire sample volume, gelatins show the so called "gelling behavior" moving from a sol-like (i.e. fluid) state to a gel-like (i.e. solid) state. The gelation is primarily triggered by temperature, i.e. a sol-like state at higher temperature (approximately in the 40-80°C range) becomes a gel-like state at lower temperatures (4-40°C). However, other parameters (composition, concentration, and applied strain rate) play an important role.

A qualitative description of the gelatin structure can be obtained from texture analysis that considers its strength (firmness, hardness, brittleness, elasticity and cohesiveness) in the gel-state. Hence, gelatins can be soft/weak-flexible to firm-brittle (Figure 1). However, this classification does not provide a comprehensive description of their rheological properties.

In general, gelatins in gel-state show an elastic response when a high stress is applied for a short time and a viscous response when low stress is applied for a long time. For a constant imposed strain, the initial elastic deformation is converted into permanent viscous deformation and the associated stress decays in time. Materials exhibiting such characteristics are called viscoelastic (VE) [e.g. Ferry, 1980].
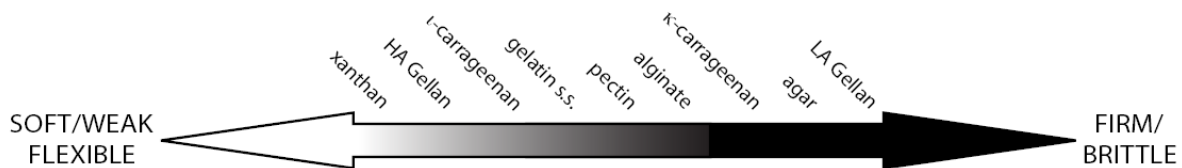
Figure 1: Characterization of gelatins according to their gel strength.

4.3 Theory and Methods

4.3.1 Basic Theory

A complete characterization of material properties requires two complementary approaches. The solid-mechanic approach deals with elastic solids, which do not dissipate energy and follow Hooke's law: strain (γ) is always proportional to stress (σ), and the stress is independent of strain rate ($\dot{\gamma}$) [e.g. Chou and Pagano, 1992; Ranalli, 1995]. The fluid-dynamic approach deals with viscous liquids that do not store energy but dissipate it, and in which there exists a proportionality between the stress (σ) and the strain rate ($\dot{\gamma}$), either linear (Newtonian) or nonlinear [e.g. Drozdov, 1996].

VE materials display a delayed, time-dependent, response when stress is applied and/or removed. The simplest rheological models to represent a visco-elastic behavior are obtained combining linear elastic and linear viscous elements in series (Maxwell model) or in parallel (Kelvin-Voigt model) [Barnes et al., 1989]. To describe this behavior it is necessary to measure the deformation energy stored in the sample during the deformation and lost afterwards [Mezger, 2002]. The rheological properties of a material can be studied by applying the theory of viscoelasticity when the material behaves "linearly", or strain-independently (i.e., its behavior does not depend on the strain history). Material characterization is carried out in terms of the storage and loss moduli [Ferry, 1980]. These parameters are determined as functions of strain, strain rate (frequency), temperature and time providing a full characterization of the material behavior. To avoid possible ambiguities, a material is termed "linear" (i.e., linear visco-elastic) when its mechanical properties do not change with strain. When a linear relationship occurs between stress and strain rate, the material is said to show Newtonian fluid behavior.

In a linear VE sample the shear stress τ is out of phase with the applied strain following the relation [Ferry, 1980]:

$$\tau = \gamma_o (G' \sin(\omega t) + G'' \cos(\omega t)) \tag{1}$$

where γ_o is the maximum amplitude of the strain and, G' and G'' are frequency-dependent functions. Measurements performed at a given frequency (ω) provide simultaneous determinations of G' and G'' [Mezger, 2002]. *VE* behavior is illustrated in Figure 2. In the region where $G'>>G''$, the system can be described by Hooke's law and the elastic shear modulus, G_o, is given by [Bagdassarov and Dorfman, 1998]:

$$G_o = \lim_{\omega \to \infty} G'(\omega) \tag{2}$$

On the other hand, the material shows viscous behavior in the frequency range where $G''>>G'$. The complex viscosity, η^*, is defined by [Nowick and Berry, 1972; Barnes et al., 1989]:

$$\eta^*(\omega) = \frac{G' + iG''}{i\omega} \tag{3}$$

and the dynamic viscosity is given by [Marin, 1998]:

$$\eta_o = \lim_{\omega \to 0} \eta^*(\omega) = \lim_{\omega \to 0} \frac{G''}{\omega} \tag{4}$$

In the intermediate zone between the elastic and the viscous range (G'~G''), the material is viscoelastic. The ratio of the viscous to the elastic portion of the deformation behavior, G''/G', called "loss factor" or "damping factor", is relevant for material characterization [Mezger, 2002]:

$$\frac{G''}{G'} = \tan\delta \tag{5}$$

The parameter G''/G', also labeled as "internal friction" (Q^{-1}) and comparable with the seismic attenuation [e.g. Ranalli, 1992], is used in studies of the rheological properties of lavas [Bagdassarov and Dorfman, 1998; James et al., 2004; Sumita and Manga, 2008]. The phase shift angle, δ, between viscous and elastic parameters, known as "loss angle", is used as criterion in determining the gel formation [Mezger, 2002]:

$$\delta = arctg\left(\frac{G''}{G'}\right) \tag{6}$$

Ideal-elastic behavior occurs when $\delta = 0°$; while, ideal-viscous behavior is expressed as $\delta = 90°$. When viscous and elastic behaviors exactly balance (*G'=G''*), $\delta = 45°$: the sample structure is in

sol-state for $\delta > 45°$ ($G''>G'$) and is gel-state for $\delta < 45°$ ($G'>G''$). The mechanical behavior is strongly dependent on composition, concentration, temperature and time [Askeland, 1990].

To give a full characterization of material properties it is also required to provide information about large-deformation properties and fractures. Fracture is considered to occur when all bonds between the structural elements of a material in a certain macroscopic plane break, resulting in a breakdown of the structure of the material over length scales much larger than the structural elements [van Vliet and Walstra, 1995]. Materials that fracture in the elastic region are termed brittle. Brittle fracture shows a sudden drop in stress on fracture. Fracture properties are much more strongly dependent on the physical structure of gelatins than small-deformation properties. Moreover, the stochastic size distribution of defects and the deformation speed play an important role. Therefore, relationships are not simple and depend on the physical structure of the gelatins.
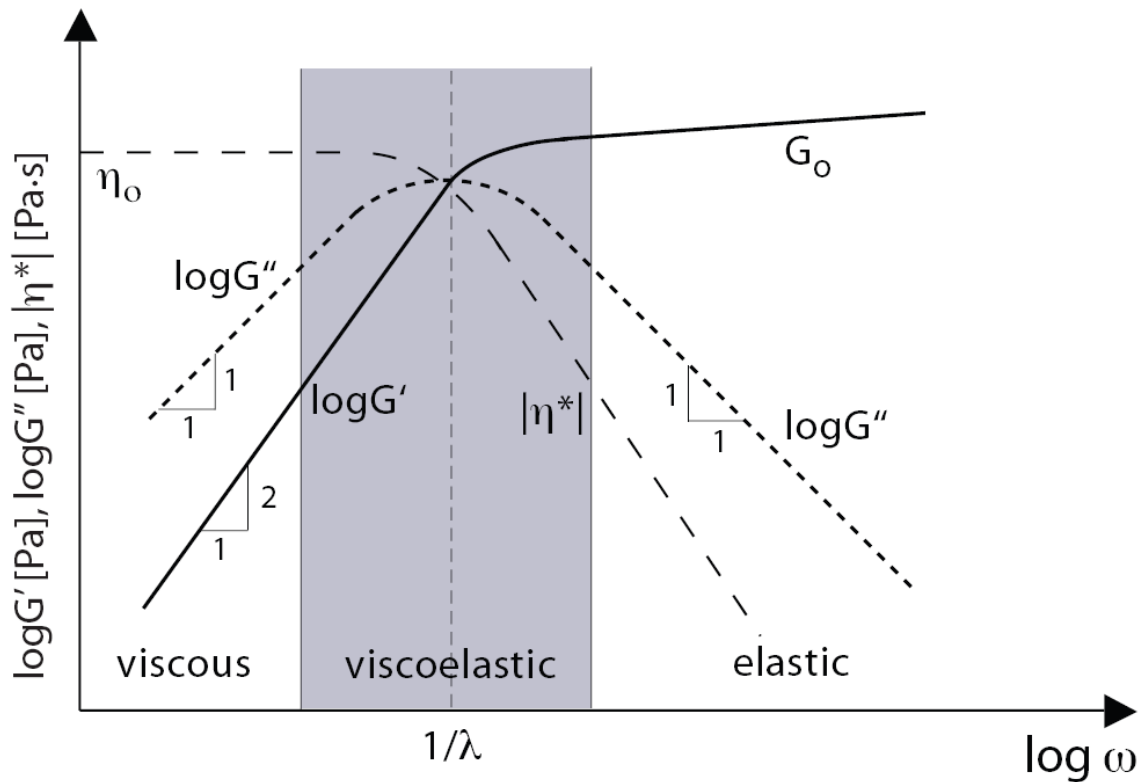
Figure 2: Typical rheological properties of an ideal linear viscoelastic material. At low frequency (viscous behavior) $\log G'(\omega)$ increases with slope as 2:1 because $G' \sim \omega^2$ for $\omega \rightarrow 0$, while $\log G''(\omega)$ increases with slope as 1:1 because $G'' \sim \omega$. In this range the loss modulus G'' is always larger than the storage modulus G'. The complex viscosity $|\eta^*|$ is

constant and equal to the zero-shear viscosity η_o. At high frequency (elastic behavior) $G'(\omega)$ reaches the constant plateau value G_o and $G''(\omega)$ falls with a slope (-1):1 because $G'' \sim 1/\omega$ for $\omega \to \infty$. The storage modulus is always larger than the loss modulus. At intermediate frequencies (viscoelastic behavior) G' and G'' are of the same order of magnitude. At the point $\omega \cdot \lambda = 1$, $G''(\omega)$ reaches its maximum and the intersection of G' and G'' determines the relaxation time, λ, of the system [modified from ten Grotenhuis et al., 2002].

4.3.2 Rheological methods

Several tests can be performed in order to explore the visco-elastic rheology of gelatins. The rheometric determinations are performed using a Physica MCR 301 (Anton Paar) rheometer (Figure 3). The instrument accuracy is better than 0.1 % which results in a measurements accuracy less than 5 %, as verified by random repeated tests. A Couette measuring system (Figure 3a) or parallel plate geometries (Figure 3b) are used. To ensure an accurate temperature control within the sample a Peltier element coupled with a thermo-electrical pump is adopted. This equipment allows high heating and cooling rates to be achieved within a precision of 0.01°C. Evaporation of the sample is prevented using a water-lock.

Oscillatory regime (dynamic sweep test) is used to estimate visco-elastic behavior, while torsional flow is imposed to the sample in rotational regime (rotational test) when estimating ideal viscous properties. In both cases raw data (i.e. torque or speed) can be easily computed in shear stress, strain or shear strain rate. Features of the tests are briefly described in the following.
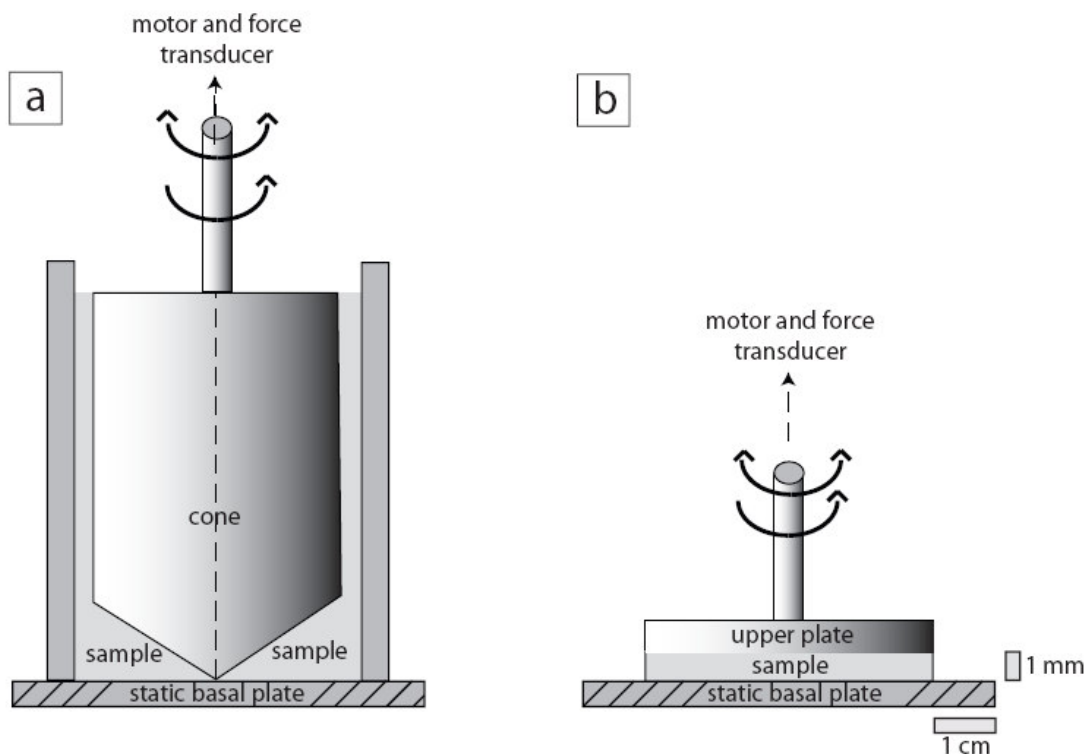
Figura 3: Schematic drawing of the stress-controlled experimental setups used in this study. a) Cone-plate geometry. b) Parallel plate geometry. Black arrows show motion directions.

4.3.2.1 Oscillatory tests

Oscillatory tests are used to examine the visco-elastic behavior of gelatins in the gel-state.

The first test required to investigate the structure of a material is the "amplitude sweep" test, in which the sample is subjected to an increasing oscillatory strain ($10^{-1} - 10^3$ %) while frequency and temperature are kept constant ($\omega = 1$ rad/s and T = 10, 30, 50°C; see Table 1 for details on measurements performed in this study). The measured G' and G'' are plotted as function of strain (Figure 4a). From the amplitude sweep the sample's character can be easily revealed defining which parameter between G' and G'' dominates. This test is performed to determine the VE range. The range is defined as the domain below a strain threshold value (γ) where the sample structure is

preserved and the *G'* and *G''* values show a constant high plateau (Figure 4a). When the strain amplitude exceeds the value (γ_l) limiting the *VE* range, the sample structure is irreversibly changed. Once the *VE* range is defined, the *"frequency sweep"* test is performed, in which a constant oscillatory deformation (lower than the limit of VE range) with variable frequency (10^{-1}–10^{2} rad/s) is applied to the sample (see Table 2 for details on measurements). The measured *G'* and *G''* can be plotted as functions of frequency or shear strain rate. The frequency where *G'* and *G''* curves cross each other is the Maxwell relaxation time (Figure 4b).

To identify the sol/gel transition temperature, *"temperature sweep"* tests are performed (Table 3). The magnitudes of *G'*, *G''* and η^* are computed while a slowly cooling rate is applied to the sample. Frequency and oscillatory deformation are kept constant within the *VE* range. In the resulting diagrams, where moduli are plotted as function of temperature, the crossover of the *G'* and *G''* curves gives the characteristic temperature called 'sol/gel transition temperature', 'gel point' or *Tg*, below which the sample is in gel-state (Figure 4c).

To control the ageing effect on gelatin structure, *"time sweep"* tests are performed, in which strain, frequency and temperature are kept constant (γ = 5 %; ω = 1 rad/s and T = 10°C), while changes of *G'* and *G''* over time are determined. The values of *G'* and *G''* are measured at regular intervals (1 minute for 6 hours). The resulting curves show a constant high plateau after few hours, showing that the gel structure is approaching equilibrium (Figure 4d).

a

log G′ [Pa]

log G′

log G″

log G′ , log G″ [Pa]

LVR

NLVR

$\gamma_L (\tau_L)$

log γ [%] (l

b

G_O

$G_O/2$

logG′, logG″ [Pa], |η*| [Pas]

log G′

log G″

t_M

log ω, log

c

log G′

log G″

log G′ , log G″ [Pa]

T_{min}

T_g

T_{max}

T [°C]

d

2

1

3

G′ [Pa]

t [s]

e

3

1

2

η [Pa s]

$\dot\gamma$ [s⁻¹]

70
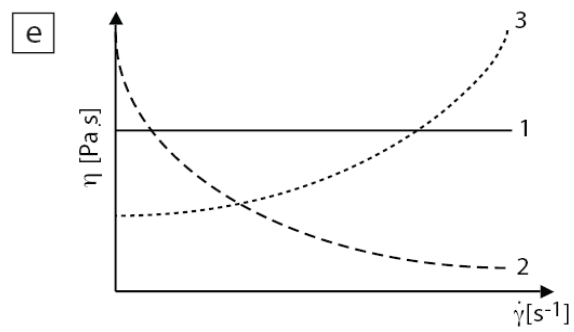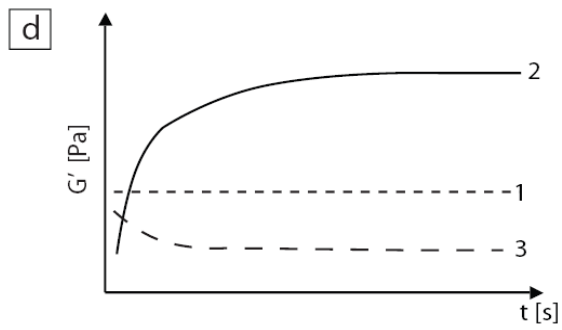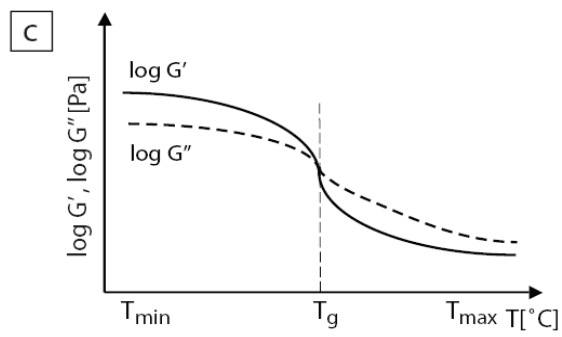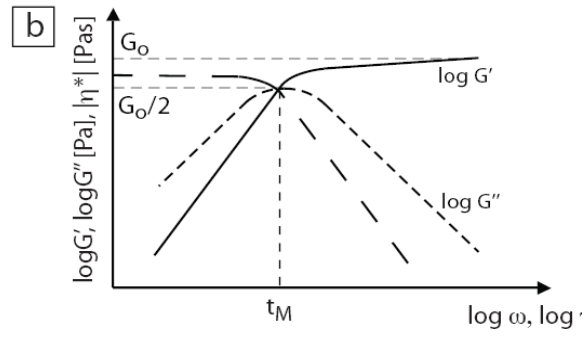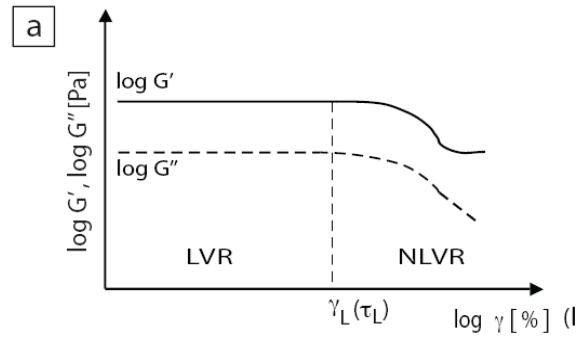
Figure 4: Different tests performed on the samples.

a) Amplitude sweep curves (γ variable, ω constant). Log$G'(\gamma)$ and log$G''(\gamma)$ with the limiting value γ_L of the *VE* deformation range. At low amplitude, each of the functions log$G'(\gamma)$ and log$G''(\gamma)$ shows a constant plateau value and the structure of the sample is stable. At deformation higher than γ_L, the limit of the *VE* range is exceeded; the structure of the sample has been irreversibly changed or destroyed (non linear visco elastic range). $G'(\gamma)$ is taken for determining the limit of the *VE* range since its curve always falls before the $G''(\gamma)$ curve. This test constrain also the yield strength of the sample when G' and G'' are expressed as function of stress. If the stress amplitude exceed the critical value τ_l where the curves G' and G'' show constant high plateau values, the sample structure is irreversibly changed. LVR and NLVR stay for linear visco-elastic region and non-linear visco-elastic region, respectively.

b) Frequency sweep curves (ω variable, γ constant). After the amplitude test, the test conditions for the frequency sweep are selected to ensure that the test is really carried out in the range. At the point $\omega \cdot \lambda = 1$, log$G''(\omega)$ curves reaches its maximum with the value $G''_{max} = G_o/2$. At low values, gelatins show the range of the zero-shear viscosity η_o, in which the viscosity value is constant. While the G' values increase with increasing ω values (the gelatins becomes more rigid) the value of $|\eta*|$ decreases, i.e. the flow resistance of the polysaccharide melt decreases. t_m, expressing the frequency where G' and G'' curves cross each other, represents the Maxwell relaxation time.

c) Temperature sweep curves (ω and γ constant). The interval in which $G'' > G'$ is referred as the sol state and the interval in which $G' > G''$ is referred as the gel state. The intersection of the G' and G'' curves marks the sol/gel transition point T_g.

d) Time sweep curves (ω, γ and T constant). 1) time-independent material: G' is constant in function of time; 2) the strength increases with aging time: the number of entanglements rises blocking particle movements; 3) the strength decreases with time: entanglements are destroyed with time.

e) Viscosity curves obtained with rotational test. 1) Idealviscous (Newtonian); Non-Newtonian materials: 2) Shear-thinning when η decreases with increasing load; 3) shear-thickening when η increases with increasing load.

4.3.2.2 Rotational tests

We use the *"controlled shear rate test"* deforming the sample in sol-state by imposing a wide range of shear strain rate (10^{-2} – 10^{3} s^{-1}; see Table 4 for details) in a logarithmic ramp profile. The method ensures the achievement of steady state flow. The resulting stress is recorded and flow and viscosity curves are produced (Figure 4e). The analyzed material is defined as ideal-viscous, shear-thinning or shear-thickening if η is independent, decreases or increases with shear strain rate, respectively. Gelatins are usually ideal-viscous or shear-thinning.

"Controlled shear stress tests" are used to determine the yield stress of gelatins [Eisenstadt and Sims, 2005] . The sample in sol state is loaded between the plates, then, the temperature is set at a fixed value (10°C) to achieve the gel state and to ensure that the sample adheres to the rheometer plates. The shear stress is increased logarithmically (no normal stress acts on the sample) and the stress value required to achieve non-recoverable strain (that is the yield stress) is determined. If gelatins follow the Coulomb frictional law, this yield stress is the cohesive strength. Determination of frictional properties requires a different instrumentation and will be the subject of future work.

4.4. Results

4.4.1 Selected gelatins

Properties of gellan gum, κ-carrageenan, gelatin s.s. (pig skin) and xanthan gum samples were extensively investigated. These gelatins cover the spectrum from brittle and firm samples to weak and flexible ones (Figure 1). All the selected gelatins are thermo-reversible, forming firm gels and fluids below and above the gel point, respectively. The main difference between these materials is that gellan gum, κ-carrageenan and xanthan gum are plant polysaccharides, while pig skin gelatin is an animal protein.

Pig skin is largely the most mentioned gelatin in geoscience applications, especially in models of dyke and magma propagation [e.g. Heimpel and Olson, 1994; Menand and Tait, 2002; Acocella and Tibaldi, 2005]. However, it is often not possible to have any information about the material used, sometimes referred to as common gelatin [Fiske and Jackson, 1972; McLeod and Tait, 1999; Hyndman and Alt, 1987; Walter and Troll, 2003; Kavanagh et al., 2006; Rivalta et al., 2005], or identified by manufacturer's labels only [Takada, 1990, 1994; Koyaguchi and Takada, 1994; Ito and Martel, 2002; Muller et al. 2001].

4.4.2.1 Composition

Rheological properties of gelatins are strongly dependent on the composition of macromolecules forming the gel network (Figure 5; Table 1). The amplitude sweep data, carried out at constant temperature and concentration (10°C and 1.0 %wt, respectively), show clear differences for the selected samples. In gel-state, xanthan gum is the weakest with the lowest measured values of G' and G'' (except for G'' at concentration of 1.0 % wt at 10°C). The other gelatins form a firmer network, (κ-carrageenan, gellan gum and pig skin from the stiffest to the weakest).
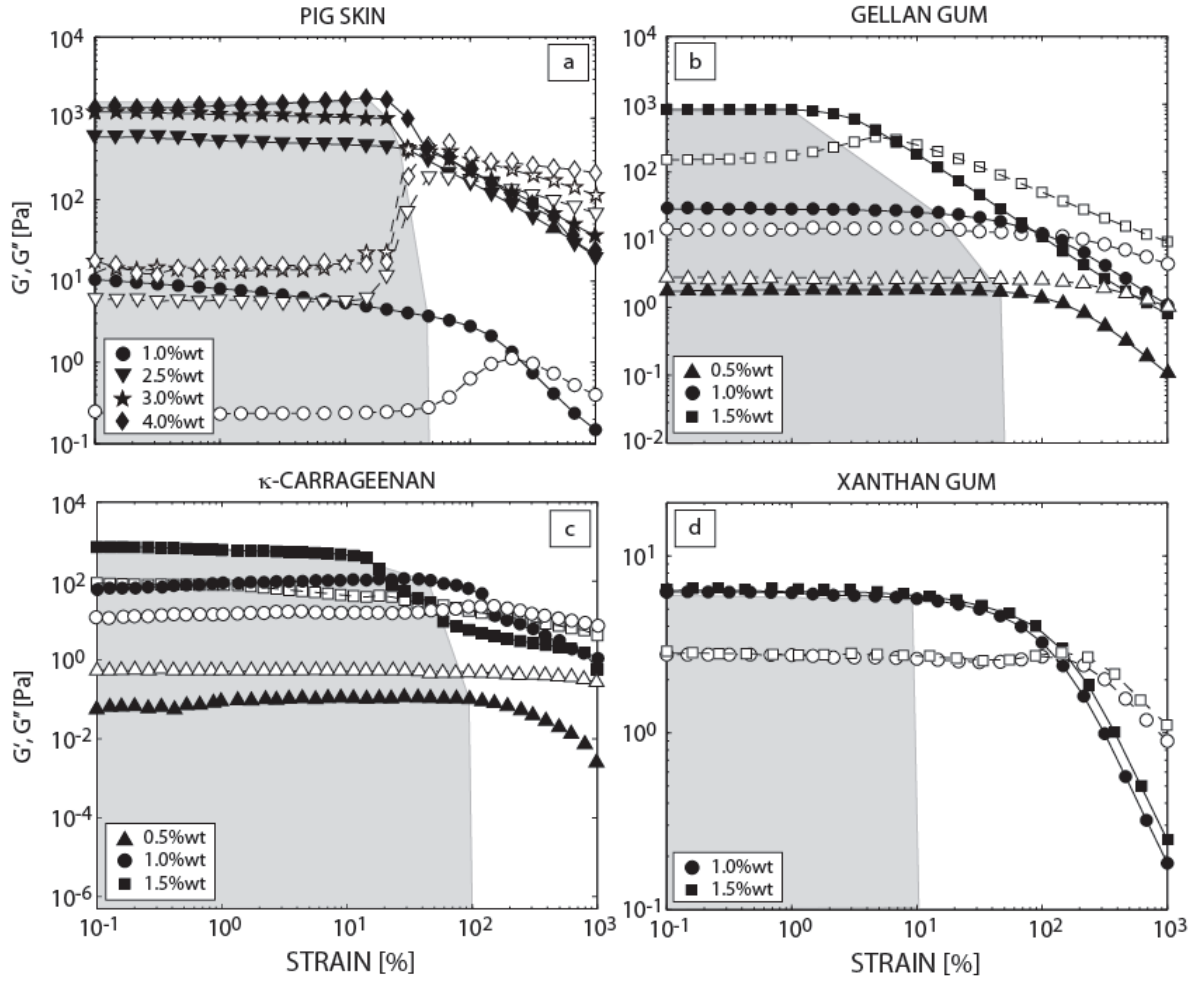
Figure 5: Effects of concentration of different gelatins as determined by amplitude sweep tests at T = 10°C for strain ranging between 10^{-1} - 10^3 %: (a) pig skin, (b) gellan gum, (c) κ-carrageenan, (d) xanthan gum. Filled symbols refer to the storage modulus, G'; empty symbols to the loss modulus, G''. Shaded areas identify the *VE* range.

The *VE* range is affected by composition as well. The value of γ_L decreases with increasing firmness, i.e. γ_L = 10 % for gellan gum, γ_L = 37 % for κ-carrageenan, and γ_L = 68 % for pig skin (Figure 5; Table 1). Xanthan gum does not follow this trend (γ_L = 14 %).

The composition affects also the gel/sol transition. Temperature sweep data show that, at the same concentration, the transition is reached at a lower temperature for pig skin than for κ-carrageenan and gellan gum (i.e., $T_g \approx 6$ and $26 - 28$°C at 1.0 %wt concentration; Table 3).

The viscous properties of different gelatins are analyzed using rotational shear rate tests at constant temperature ($T > T_g$), shear strain rate, and concentration (Table 4). Composition affects the viscosity of the sample, which increases with gelatin firmness, i.e. $\eta = 0.02$ Pa s for pig skin, $\eta = 0.05$ Pa s for gellan gum. The viscous component in the gel-state, as recorded at 10°C, shows a similar trend. Again, xanthan gum displays a peculiar behavior, since it is a weak gelatin (see Figure 1), but shows a relatively high viscosity. This can be probably related to its atypical structure, characterized by chains forming double helixes, which give it a rather rigid configuration [Davidson, 1980]. Consequently, xanthan is able to produce a large increase in water viscosity by adding a very small quantity of gum.

Compositional differences influence also the stiffness of gelatin networks. The stress limit to the range, determined by amplitude sweep data, shows that, for a fixed concentration (1.0 %wt; Table 1), κ-carrageenan forms the stiffest network. Gellan gum and xanthan gum show a slightly lower value, and pig skin is the weakest, with a stress limit 3 – 4 order of magnitude lower than the others.

4.4.2.2 Concentration

In order to investigate the effects of concentration, temperature is kept constant and the concentration of the polysaccharide in water is varied systematically from a minimum of 0.5 % to a maximum of 4.0 %wt for each of the selected gelatins (Figure 5, Tables 1-5).

The amplitude sweep data (Figure 5; Table 1) show that gelatins with higher concentration display an increase of both storage and loss moduli. Moreover, the difference between G' and G'' rises with the increase of the concentration (Figures 5a-c, Table 1), since G'' increases at a lower rate than G'. Xanthan gum shows a different trend (Figure 5d, Table 1): G' and G'' increase at the same rate and only slightly with concentration.

This behavior, confirmed by frequency sweep data (Table 2), is also highlighted by the trends in the coefficient of internal friction, Q^{-1}, and the loss angle, δ (Table 5). Both factors decrease with

increasing concentration in κ-carrageenan, gellan gum and pig skin, while they are constant for xanthan gum.

Flow data in the sol-state recorded for constant T and $\dot{\gamma}$ (Table 4) show that the viscosity of each gelatin increases with increasing concentration. The threshold, γ_L, under which the sample is in the *VE* regime decreases with increasing concentration (Figure 5, Table 1).

Results of controlled stress tests carried out on pig skin samples show that the yield stress increases with increasing concentration, varying as an order of magnitude from 10^2 to 10^4 Pa for concentrations in the $1.0 - 2.5$ %wt range (Figure 6).
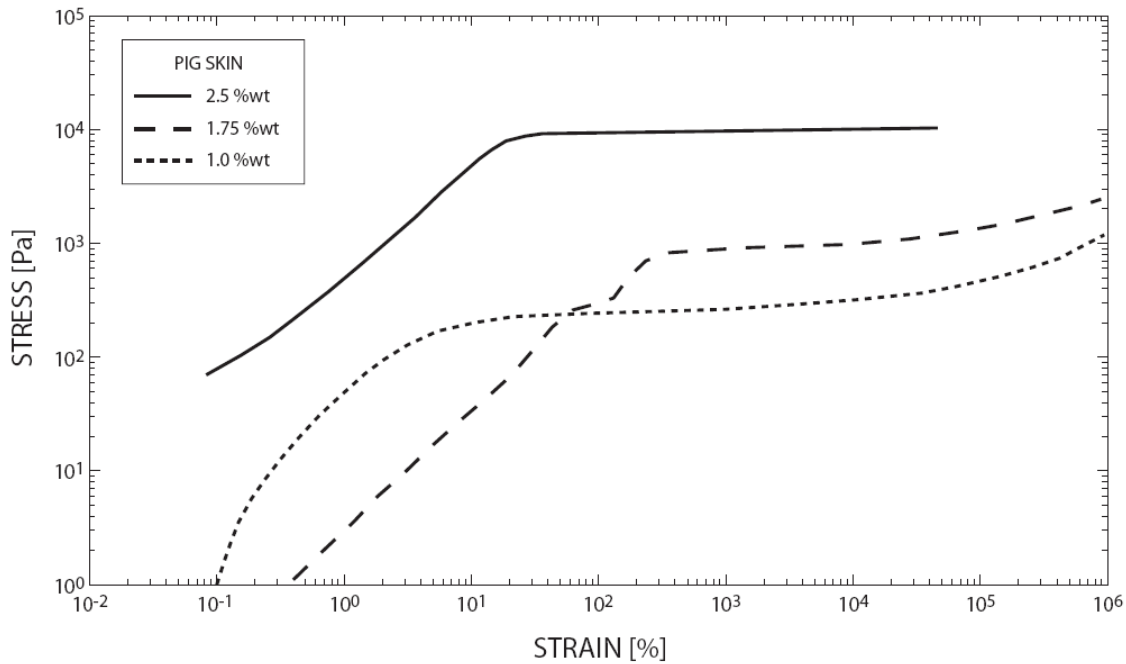
Figure 6: Results of controlled stress tests for pig skin. The yield stress increases with concentration, varying from approximately 10^2 to 10^4 Pa for concentration in the $1.0 - 2.5$ %wt range.

4.4.2.3 Temperature

The role of temperature on the *VE* properties of the gelatins is examined by rheometric tests in which only the temperature is varied (from 10°C to 50°C), while the concentration is kept constant (in a range from 0.5 % to 4 %wt). Dynamic amplitude/frequency sweep (Tables 1-2), temperature

sweep (Table 3) and rotational tests (Table 4) are performed.

Figure 6 a-c shows the variations of the moduli of gellan gum with temperature. Both G' and G'' increase, and their difference decreases, with decreasing temperature. G'' is larger than G' for the sample with the lowest concentration, i.e. gellan gum at 0.5 %wt, in the whole explored T range (Figure 7a). For higher concentration, i.e. 1.0 %wt, G' is slightly larger than G'' for $T < 30°C$, but $G'' > G'$ above (Figure 7b). For the highest concentration (1.5 %wt, Figure 7c), $G' > G''$ always. Moreover, by decreasing the temperature the viscosity increases (Table 4) and the VE range (Table 1) decreases. κ-carrageenan and pig skin bear in the same way by varying the temperature of the experiments (Tables 1-4).

The behavior of xanthan gum is exactly the opposite (Figure 7d-e, Table 1-2) because, unlike other gums, this gelatin is very stable under a wide range of temperature. G' and G'' slightly increase with increasing T. $G' > G''$ in every case and the difference between the two moduli decreases for increasing T. Therefore, the range in which the sample is VE is larger for lower temperature (Figure 7, Table 2).
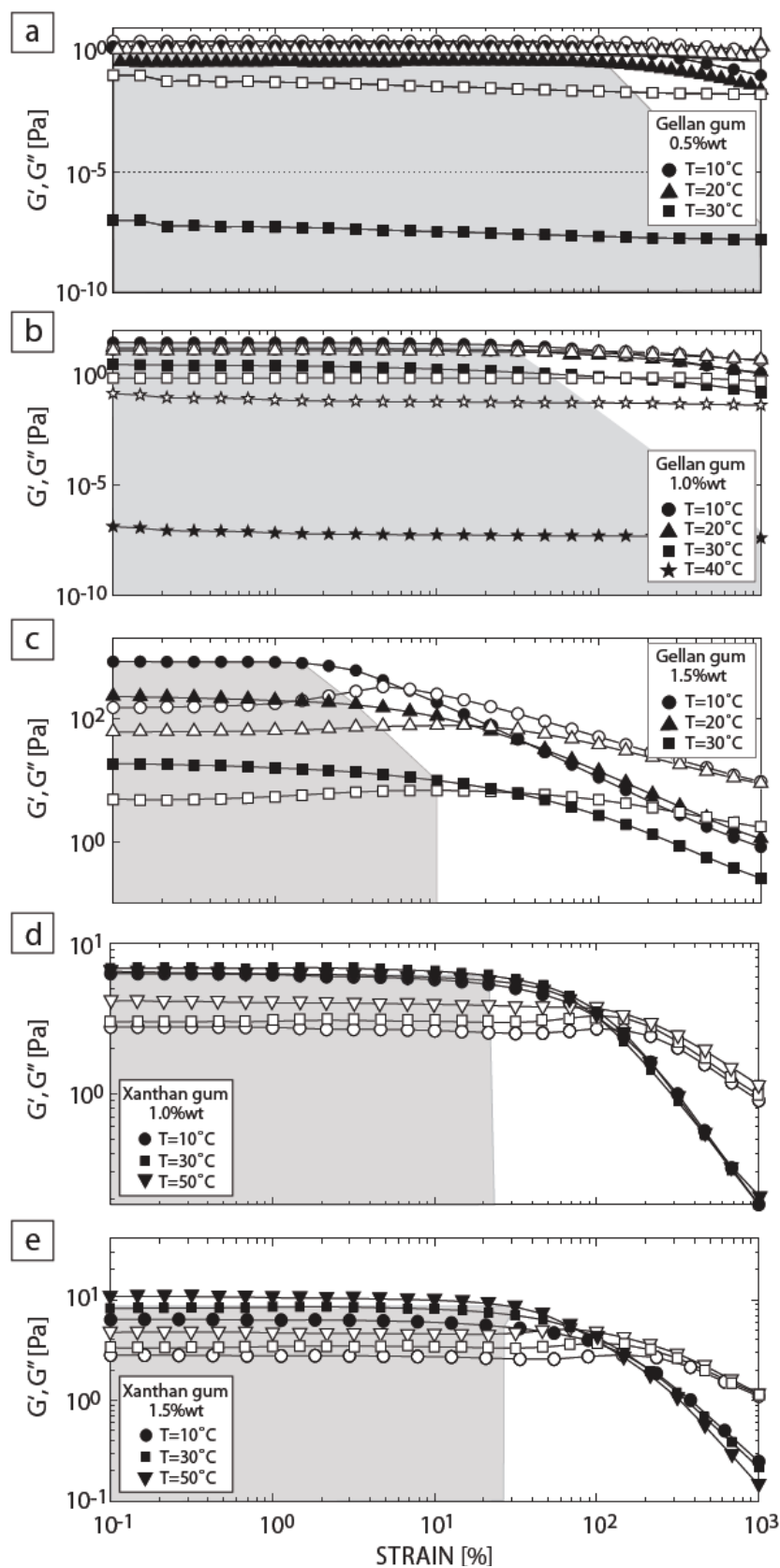
Figure 7: Effects of temperature on gelatins as determined by amplitude sweep tests: (a) gellan gum 0.5 %wt, (b) gellan

gum 1.0 %wt, (c) gellan gum 1.5 %wt, (d) xanthan gum 1.0 %wt, (e) xanthan gum 1.5 %wt. Filled and empty symbols as in Fig. 5.

Further information about the effects of the temperature can be obtained by the temperature sweep test. Results on gellan gum samples (1.0 %wt and 1.5 %wt) are shown in Figure 8, where G', G'' and the modulus of complex viscosity, $|\eta^*|$, are plotted as functions of T. The storage modulus, G', is larger than the loss modulus, G'', for low T. The temperature at which the curves $G' = G''$ determines the gel point, T_g. For a given gelatin, T_g increases with increasing concentration (Figure 8). The behavior of gellan gum is similar to that of other gelatins (Table 3).
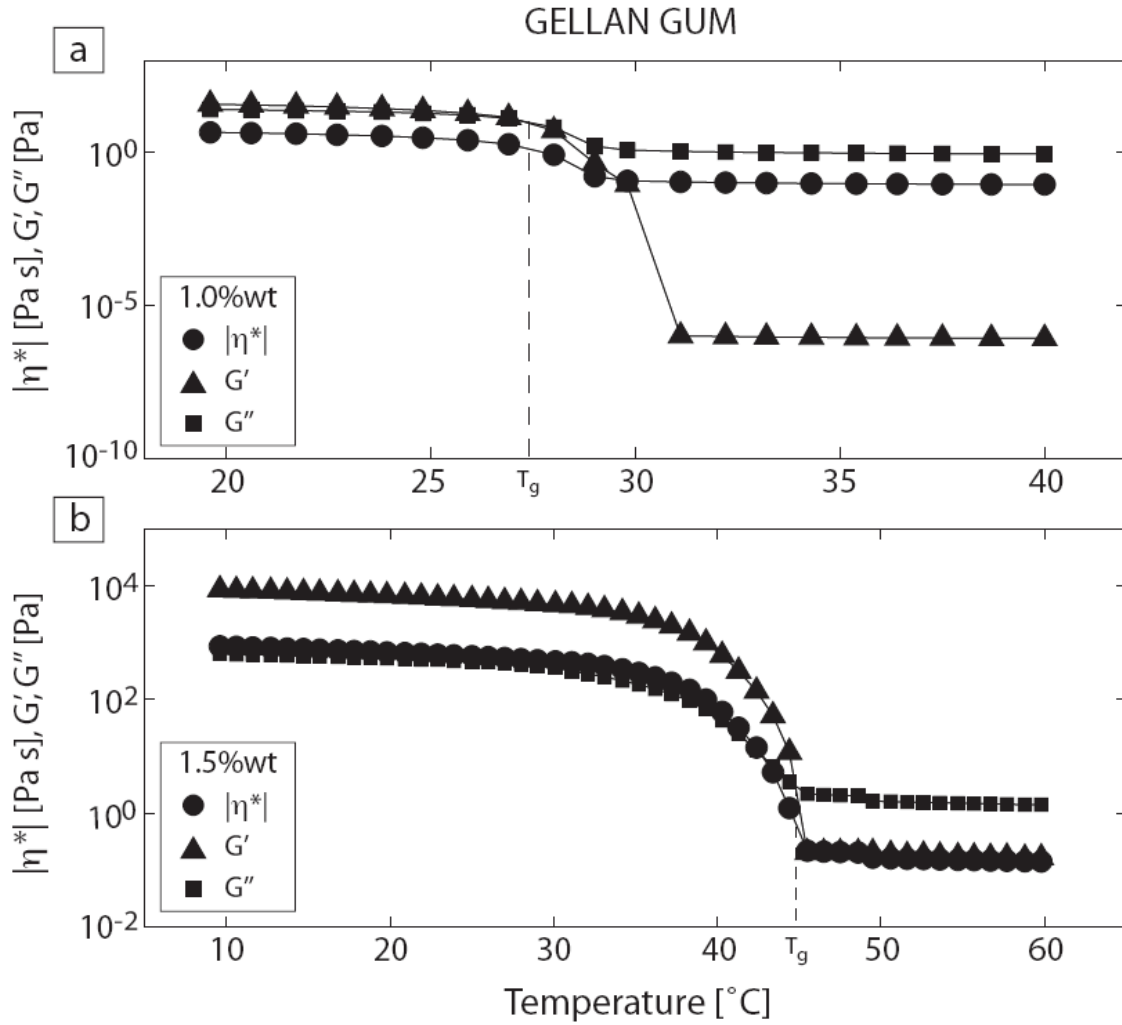
Figure 8: Results of temperature sweep tests performed on gellan gum with different concentrations, (a) 1.0 %wt and (b) 1.5 %wt. The intersection of G' and G'' gives the gel point.

4.4.2.4 Ageing

As with concentration and temperature, the ageing of the gelatin may affect its rheological properties. The structure of the gel is not static and progressively changes because of the instability of the low energy interactions that connect the gel network [Tosh et al., 2003]. Therefore, it is necessary to know the time elapsed since formation of the sample.

Time sweep tests allow to distinguish two main phases (Figure 9). The moduli *G'* and *G''* increase rapidly during an initial time interval, related to continuous development of entanglements. Afterward, a plateau is reached when the sample reaches a stable structural arrangement. For pig skin (2.5 %wt) at *T* = 10°C the gel structure reaches a stable organization after 120 minutes. *κ*-carrageenan (1.0 %wt) and gellan gum (1.0 %wt) reach stability after a longer time. A comprehensive data base on the duration of the increasing phase can be found in Tosh et al. [2003]. Once structural stability is reached, samples preserve it for a limited interval depending on composition, concentration and temperature before the moduli are irreversibly modified. Measurements of *G'* were performed 6, 24, 48 and 96 hours after the sample preparation. *G'* decreases with the sample ageing (*G'* ~ 1.1×10^4 Pa and ~ 930 Pa after 6 and 24 hours, respectively) and reaches, after 48 hours, an asymptotic value (*G'* ~ 500 Pa) that is lower than one order of magnitude of the value after 6 hours. Longer intervals enhance the development of fungal formations which can destroy the gelatin structure. Hence, precise rules have to be followed to prepare gelatins with stable and reproducible properties (see Appendix).
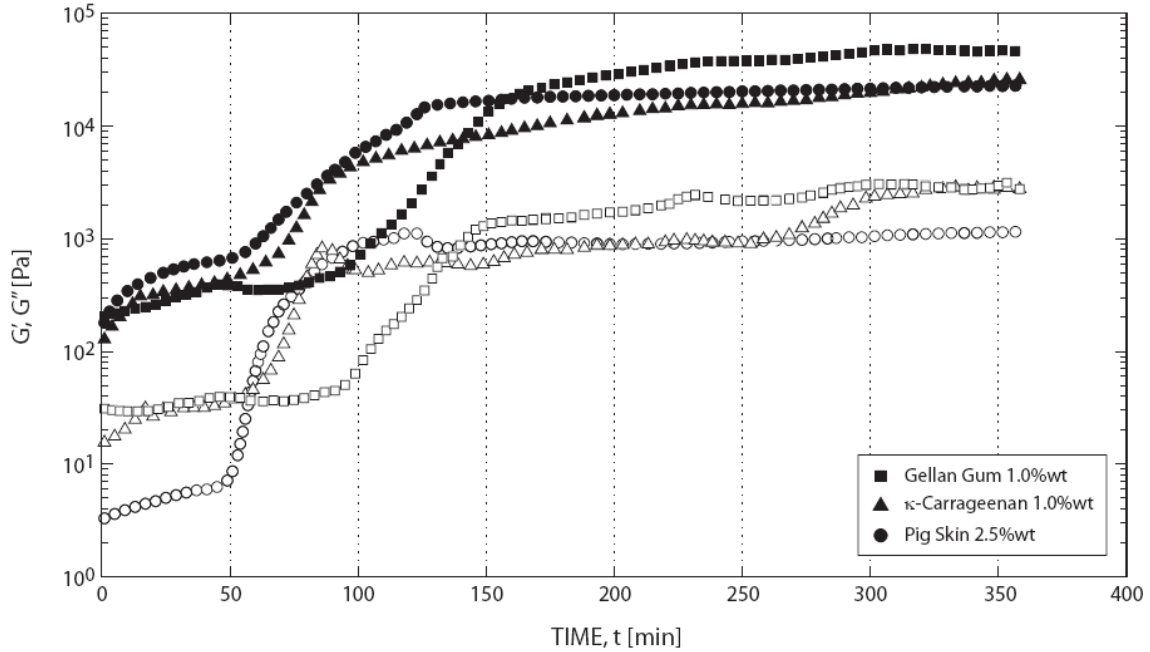
Figure 9: Effects of ageing on storage and loss moduli as obtained from measurements at 10°C. Filled and empty symbols as in Fig. 5.

4.4.3 Other physical properties

Other physical properties of interest for modeling purposes are density, transparency, thermal expansivity, thermal conductivity, and specific heat. Results are shown in Table 6.

Density measurements are performed using two different methods for gelatins in sol- and gel-state, respectively. The density of gelatins in fluid state is measured with the densimeter DMA 38 Paar at $T = 40.0°C$. Accuracy is of ±0.0001 g/cm^3. For gelatins in solid state a pycnometer is used at $T = 4°C$. Accuracy is of ±0.001 g/cm^3. Density values of gellan gum, κ-carrageenan and xanthan gum, are similar and higher than those of pig skin at the same concentration and temperature. The similarity may be due to the fact that gellan gum, κ-carrageenan and xanthan gum powders are extracted from plants, while pig skin is derived from animal protein. The transparency of the samples is a necessary property in models that require three-dimensional visual inspections. It is determined by positioning a reference grid below each sample of standard dimensions and

evaluating qualitatively, the easiness of visualizing it from above the sample. Both pig skin and κ-carrageenan gelatin show good transparency, while gellan gum and xanthan gum are rather cloudy.

Thermal expansivity has been measured by heating overnight at 80°C a fixed quantity of material inside a reference capillary tube, then removing the sample and measuring its volume at regular intervals while cooling from 80°C to room temperature (24°C). The measurement has been possible only for gelatins with highest concentration or strongest behavior. The thermal expansivity increases with the strength of the gelatin and/or its concentration. Its value ($\sim 3 \times 10^{-4}$ K^{-1}) is about one order of magnitude higher than the thermal expansivity of the Earth's upper mantle [e.g. Parsons and Sclater, 1977; Craig and McKenzie, 1986]. A good analog material should show the same relative change in volume as its natural prototype over equivalent temperature variations. The higher thermal expansivity of gelatins compensates for the smaller experimental temperature ranges with respect to the natural prototype.

The thermal conductivity and the specific heat of gelatins have been extensively studied in the literature. Values are close to those of pure water (0.607 Wm^{-1}K^{-1} and 4.186 kJ kg^{-1}K^{-1}, respectively; e.g. Williams and Mittal, 1999, Rahman, 1995].

4.5 Gelatins as rock analogs for upper crustal deformations

Similarity analysis is the central step in analog model design, helping to select analog materials, experimental dimensions and rate of deformation. In order to scale a laboratory model to a natural process, the model should be geometrically, kinematically, dynamically and rheologically similar to the prototype [e.g. Hubbert, 1937; Ramberg, 1981]. The application of similarity analysis begins with the identification of the most relevant physical parameters acting into the natural system. Then each variable (e.g., length, velocity, force and material moduli) is normalized, resulting in a set of dimensionless parameters [e.g. Cobbold, 1975; Ramberg, 1981; Weijermars and Schmeling, 1986]. Each set defines a family of equivalent solutions, differing only by a scale factor. The solution characterized by the most relevant scaling can be used to identify the most suitable material analog.

In this section, we investigate the potential use of the visco-elastic-brittle properties of gelatins to provide a mechanical model of upper crustal deformation. Temperature is not considered in the scaling procedure. Gelatins can potentially be used in sandbox-type models without an applied temperature gradient. However, a temperature gradient can be used to control the variation in vertical strength of the model, and therefore the rheological layering of the lithosphere. Work on this topic is in progress. Extension to a reasonably scaled sub-lithospheric mantle is not possible since the Reynolds number of gelatins in the sol state is too high (10^2-10^3).

We use amplitude sweep data (Figure 5, Table 1) to select gelatins samples exhibiting a) G' and G'' of the same order of magnitude and b) $G' > G''$. These conditions guarantee we are selecting a solid visco-elastic sample. Many samples fall in this category (Table 1). The following detailed analysis is carried out on pig skin 2.5 %wt in order to present a concrete example.

A reasonable experimental temperature range is between 5 and 60°C. We choose $T = 10$°C at which gelatins, included pig skin 2.5 %wt, are always in their gel-state (Table 1, Figure 5c). The experimental strain rate is selected to ensure that the sample is in the *VE* range. This condition guarantees that the behavior of the material is independent of its deformation history, and therefore allows the correct determination of storage and loss moduli. When using pig skin 2.5 %wt the strain rate should be below 0.147 s^{-1}, after which the material behaves quasi-linearly (Figure 5c, Table 1). At a strain rate of 10^{-2} s^{-1} the complex viscosity of pig skin 2.5 %wt is of about 50 Pa s.

It is now possible to estimate the length scaling factor that should be adopted in order to use pig skin 2.5 %wt to model the upper crust, assumed to have thickness $h = 15$ km, density $\rho = 2700$ kg m^{-3} and viscosity $\eta = 10^{20}$ Pa s at a strain rate of 10^{-15} - 10^{-14} s^{-1}. Assuming that viscous stress in the analog material scales with lithostatic stress, the dimensionless stress parameter σ^* is:

$$\sigma^* = \sigma_n/\sigma_m = (\eta_n \cdot \dot{\gamma}_n) / (\eta_m \cdot \dot{\gamma}_m) = (\rho_n \cdot g_n \cdot h_n) / (\rho_m \cdot g_m \cdot h_m) \qquad (7)$$

where σ denotes stress, $\dot{\gamma}$ strain rate and g the acceleration of gravity. The subscripts n and m refer to the natural prototype and the laboratory model respectively. Since models are executed in the field of gravity, $g_n = g_m$ and equation (7) gives:

$$(\eta_n \cdot \dot{\gamma}_n)/(\eta_m \cdot \dot{\gamma}_m) = (\rho_n \cdot h_n) / (\rho_m \cdot h_m) \tag{8}$$

Using the relevant parameters for the model material ($\eta = 50$ Pa s, $\dot{\gamma} = 10^{-2}$ s^{-1} and $\rho = 996$ kg/m^3), the experimental layer thickness is $h_m = 20$ cm and $h_m = 2.0$ cm for natural strain rates of 10^{-15} s^{-1} and 10^{-14} s^{-1} respectively. This range of length scales is reasonable for laboratory models.

The stress scale is defined as the dimensionless ratio between the normal isostatic stress acting at the base of the upper crust in nature and in models (cf. eq. 7). With the proper length scale, we have $\sigma_n = 3.97 \times 10^8$ Pa, $\sigma_m = 1.95$ x 10^2-10^3 Pa, and therefore, $\sigma^* = 2.04$ x 10^5-10^6. Using this value to infer the experimental shear modulus, we obtain $\mu_m = 4.9$ x 10^3-10^4 Pa for a natural shear modulus $\mu_n = 10^{10}$ Pa. The complex shear modulus G^* of pig skin 2.5 %wt shows a plateau at about 10^3 Pa (Figure 5c), suggesting that it is appropriate to model the elastic component of the upper crust.

In order to see whether pig skin 2.5 %wt scales properly with the ductile behavior of rocks, we determine its creep activation parameters. The general form of the creep equation is:

$$\dot{\gamma} = A \, \sigma^n \, exp(-E \, /RT) \tag{9}$$

and, therefore, the effective viscosity is

$$\eta = \sigma / \dot{\gamma} = A^{-1/n} \, \dot{\gamma}^{(1-n)/n} \, exp(E \, /nRT) \tag{10}$$

where E is the activation energy for creep, R the universal gas constant, T the absolute temperature, n the stress exponent, and A a material constant [see Ranalli, 1995 and references therein]. The stress exponent, n, can be obtained from flow test data by measuring viscosity $\eta(\dot{\gamma})$ at constant temperature. When plotted on logarithmic coordinates, the experimental data fall on straight parallel lines with slope $(1-n)/n$:

$$ln \, (\eta) = [-(1/n) \, ln \, (A) + (E \, /nRT)] + [(1-n)/n] \, ln \, (\dot{\gamma}) \tag{11}$$

where *ln* is the natural logarithm. We use data obtained at $T > Tg$ to ensure that the sample is in the sol-state and at temperature low enough ($T \leq 50°C$) to exclude water evaporation from modifying the rheological properties of the sample. Our results (for $T = 30\text{-}40°C$) show that the material is nonlinear with the stress exponent $n \approx 5.0$ (Figure 10). The larger value than commonly assumed in nature ($n = 2.5 \text{ - } 3$) enhances the localization of deformation but does not alter the applicability of the gelatins to modeling purposes.
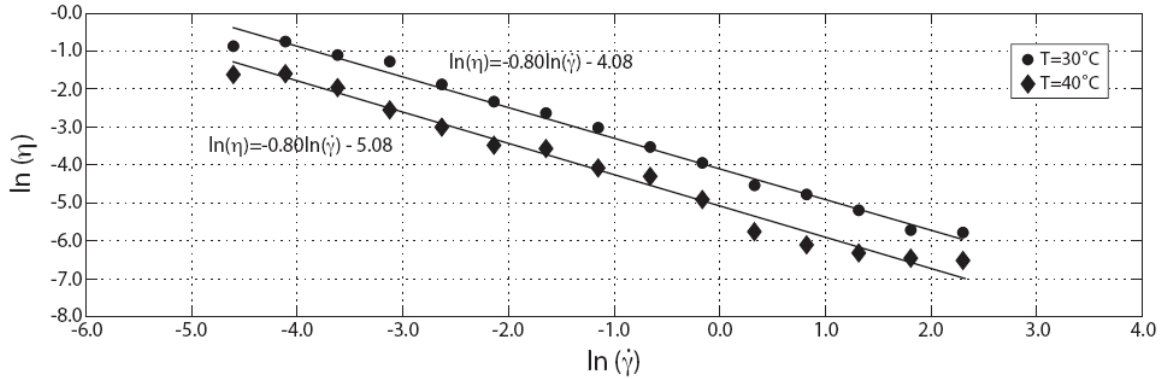
Figure 10: Viscosity of pig skin 2.5 %wt sample as a function of strain rate at two different temperatures. The slope of the curves (-0.80) gives $n = 5.0$.

The creep activation energy is obtained by plotting $\log(\eta)$ as a function of $1/T$, at constant $\dot{\gamma}$. The data fall on a straight line with slope *E/nR:*

$$ln\ (\eta) = [(1/n)\ ln\ (A) + [(1\text{-}n)/n]\ ln\ (\dot{\gamma}\ )]+ E\ /nRT \qquad (12)$$

Results show that pig skin 2.5 %wt at $\dot{\gamma}$ of 10^{-2} s^{-1} has an activation energy of 500 kJ mol^{-1} (Figure 11). If the analysis is limited to the temperature range 30 - 40°C in order to limit the evaporation problem, the value of the activation energy is 450 kJ mol^{-1}.
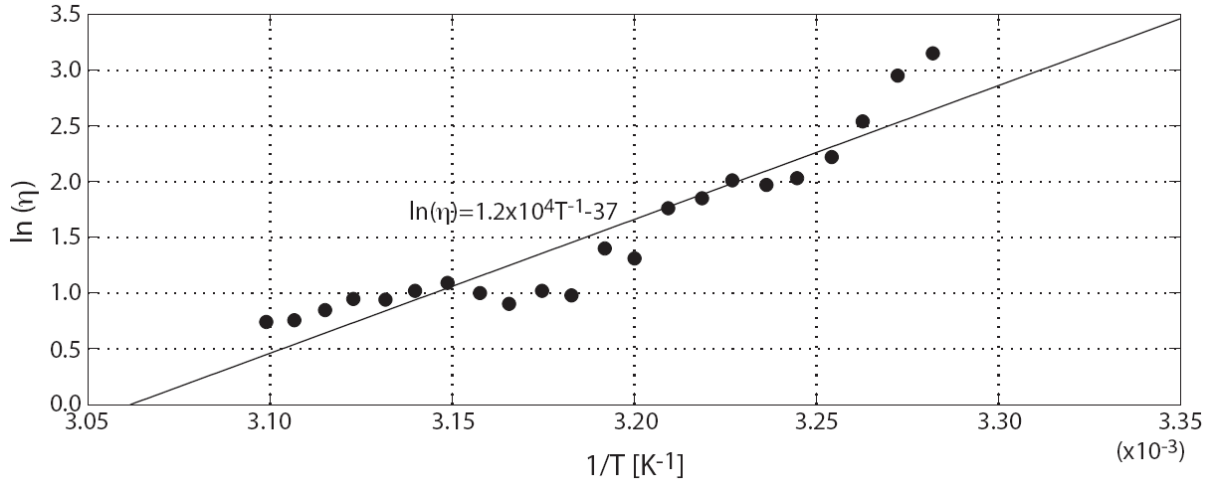
Figure 11: Viscosity of pig skin 2.5 %wt as a function of inverse temperature. The slope of the curve (1.2 x 10^4) gives E = 450 kJ mol^{-1}.

Average crustal composition can be represented by quartz-rich or feldspar-rich rocks, with n and E ranging between 2 - 3.5 and 150-250 kJ mol^{-1}, respectively [cf. Ranalli, 1995]. Taking for instance $n = 2.5$, $E = 200$ kJ mol^{-1} and a reference temperature of 300°C for the upper crust, we see that a decrease in viscosity of 1 o.o.m. requires a temperature increase $\Delta T \approx 90$°C in nature and ≈ 20°C in pig skin 2.5 %wt at $T = 10$°C. This range is appropriate for laboratory models.

The characterization of a visco-elastic-brittle material requires also the determination of the yield stress. In nature, the critical stress difference for frictional failure is given by [e.g. Ranalli, 1995]:

$$\sigma_c = \alpha \times \rho \times g \times z \times (1-\lambda) \tag{13}$$

where α is a parameter depending on the frictional properties of the material and on the orientation of the stress field, ρ is the density of the material above the depth z, and λ is the pore fluid factor. Assuming that deformation occurs in the wet upper crust ($\lambda = 0.4$), with friction coefficient 0.75, σ_c = 178, 285 and 714 MPa for normal, transcurrent and thrust faulting, respectively, if cohesion is negligible, or higher for finite cohesion. Since the strength scales with the stress, the properly scaled analog material should have a yield stress of at least 10^2 - 10^3 Pa. This is precisely the range of values for yield stress obtained from controlled stress tests (refer back to Figure 7).

Finally, the timescale is set using the relation:

$$t^* = t_n/t_m = (\sigma_m/\sigma_n) \times (\eta_n/\eta_m) = [(\rho \times g \times h)_m/(\rho \times g \times h)_n] \times (\eta_n / \eta_m) \tag{14}$$

where t is time. Using the abovementioned natural and experimental parameters, the time scaling factor is $\approx 10^{12} - 10^{13}$ for thin and thick models, respectively. Hence, 1 min in the model corresponds to 1.9 – 19 Ma in nature. Laboratory models lasting few minutes can consequently model processes taking tens of million years in nature.

4.6 Conclusions

The rheological and physical measurements presented in this paper characterize the complex mechanical behavior of a wide range of gelatins, ranging from hard to weak. Results show that their behavior changes gradually from a purely elastic to visco-elasto-brittle to a purely viscous (nonlinear) rheology going from the gel- to the sol-state. The rheological transition is strongly dependent on gelatins composition, concentration, temperature, ageing and applied strain rate. In view of the possible use of gelatins in analog models of geological processes, it is essential that all the parameters are accurately determined. One advantage is that the microstructure of gelatins can be efficiently manipulated by calibrating the setting parameters as a function of the experimental purposes.

Although pure gelatins cannot be used in their viscous form because they have too high Reynolds numbers (10^2-10^3), their visco-elasto-brittle rheology appears promising for the purpose of scaling crustal and lithospheric behavior. We found that pig skin 2.5 %wt at 10°C has the required rheological properties for a suitable experimental set-up to model crustal deformation. This material properly scales elastic (G^* of about 10^3 Pa), viscous ($n = 5.0$, $E = 450 - 500$ kJ mol^{-1}) and yield properties ($\sigma_c \approx 10^3 - 10^4$ Pa) of the natural prototype at the selected strain rates.

The rheological variability of gelatins highlighted by the present study strengthens the potential use of these analog materials to simulate the rheological structure of the lithosphere.

The use of a whole range of gelatins for modeling purposes could be further optimized by using *ad hoc* mixtures. For instance, xanthan gum, with its peculiar non-gelling behavior, can be used to control viscosity, without marked effects on the other properties. The natural rheological layering of the crust and lithosphere is usually modeled using different materials (i.e. sand and silicone putty, for brittle and ductile behaviour, respectively). However, in nature the rheology of a given material changes with temperature. Successful previous attempts to model the effects of a temperature gradient have involved the use of gums and paraffins, but these materials do not reproduce elastic-brittle behavior [Cobbold and Jackson, 1992; Rossetti et al., 1999]. The use of gelatins has the advantage to reproduce the full range of rheological behavior from elastic-brittle to viscoelastic to viscous.

4.7 APPENDIX: 'Cookbook' for preparing gelatins

Gelatins have been extensively used in geosciences experimental works [e.g. Fiske and Jackson, 1972; McGuire and Pullen, 1989; Takada, 1990, 1994; Hyndman and Alt, 1987; McLeod and Tait, 1999; Watanabe et al., 1999, 2002; Ito and Martel, 2002; Menand and Tait, 2001, 2002; Walter and Troll, 2003; Acocella and Tibaldi, 2005; Keep and McClay, 1997; Richard et al., 1995; Rivalta et al., 2005; Kavanagh et al., 2006]. However, they have been always prepared without following accurate and rigorous rules. In this section we will illustrate the common rules to correctly prepare gelatins showing stable and reproducible properties.

To achieve the desired gels properties, the samples have to be prepared following rigorously these steps.

Distilled water has to be gradually heated in a glass beaker by a hot plate and simultaneously mixed to make it homogenous. With the same tool we are able to control instantaneously the water solution temperature and to keep this constant until the set mixing value of the sample is reached. The mixing T for each gelatine is suggested by the product data sheets. Hence, κ-carrageenan and pig skin gelatin have to be dissolved in hot water at 60°C, gellan gum has to be dissolved at 70°C

and xanthan gum coddled (~90-100°C). Mixing gelatin at the set temperature allows a perfect dissolution of the powder, and avoids the creation of lumps and structure discontinuities once the sample is solidified. As the set mixing value is reached gelatin can be dissolved in the water. Due to small-size particles, κ-carrageenan and gellan gum tend to form lumps in hot water, but raising the mixing speed, the lumps can be broken ensuring dissolution.

The solution has to be mixed until all the powder is dissolved in water.

Once ready, the solutions have to be gradually brought at the desired working temperature that has to be maintained for a minimum of 6 hours and a maximum of 24 hours. In case working temperatures are lower than 25°C, an early cooling of the sample at room temperature before introducing it in a refrigerator avoids too sharp T-variations dangerous for the gelatin structure. Moreover, it is extremely important that the refrigerator temperature is always higher than 4°C: gelatin is basically made up of water and the reaching of the water freezing point can destroy permanently the gelatin structure. The minimal time required to have a complete formation of the gelatin is at least 24 hours.

In general, it may happen that the preparation is good but not the cooling conditions and vice versa, e.g. some gelatin samples are cooled for too short an interval [e.g. Water and Troll, 2003; Acocella and Tibaldi, 2005; Kavanagh et al., 2006], others are kept at the incorrect temperature [e.g. Fiske and Jackson, 1972; Menand and Tait, 2002], and others skip duration or temperature of the solidification phase, or both [e.g. Ito and Martel, 2002; Bons et al., 2001; Koyaguchi and Takada, 2004; Boudreau et al., 2005]. Consequently all the rheological properties of the sample are problematic and results can be considered only qualitative. Covering samples in the refrigerator with plastic wrap or with silicon oil [e.g. Menand and Tait, 2002; Kavanagh et al., 2006] guarantees a good isolation of the gelatin and avoids the water loss. Further, shrewdness germicide or sodium hypoclorite [e.g. Bot et al., 1996a; McLeod and Tait, 1999; Menand and Tait, 2002] can be added during the dissolution of the gelatin for preventing fungal formations.

Once the gelatin is ready, experiments should be carried out in a water saturated atmosphere. The model duration should never exceed a few hours to avoid measurable ageing of the sample.

Notation

γ	[%]	deformation or strain
γ_o	[%]	maximum amplitude of the strain
γ_L	[%]	threshold of the LVE range
$\dot{\gamma}$	[s^{-1}]	shear rate
σ	[Pa]	shear stress
$\sigma*$	[-]	dimensionless number for stresses
σ_c	[Pa]	critical stress difference
ω	[s^{-1}] or [rad/s]	angular frequency
η	[Pa·s]	shear viscosity
$\eta*$	[Pa·s]	complex viscosity
η_o	[Pa·s]	zero-shear viscosity
G'	[Pa]	storage modulus
G''	[Pa]	loss modulus
G_o	[Pa]	plateau value of the relaxation modulus
λ	[s]	relaxation time
δ	[°] or [rad]	phase shift angle or loss angle
Q^{-1}	[-]	damping factor, loss factor or internal friction
t	[s]	time
$t*$	[-]	timescale
ρ	[kg/m^3]	density
α	[K^{-1}]	thermal expansion coefficient
k	[W·m^{-1}·K^{-1}]	thermal conductivity
κ	[m^2·s^{-1}]	thermal diffusivity
C_p	[J·kg^{-1}·K^{-1}]	specific heat capacity
h	[m]	crustal thickness
$l*$	[-]	
T	[K]	temperature
T_m	[K]	solidus temperature
T_g	[K]	gel temperature
E	[J/mol]	activation energy for creep
n	[-]	stress exponent
A	[Pa^{-n}·s^{-1}]	material constant
R	[J·K^{-1}·mol^{-1}]	universal gas constant

TABLE 1. Amplitude Sweep data

GELATIN [%wt]	T [°C]	G' [Pa]	G'' [Pa]	γ_L [%]	
Pig skin 1.0	10	7.0	0.2	<68	$G' > G''$
	30	0.03	$2.9 \cdot 10^{-8}$	$0.1\text{-}10^2$	$G' \ll G''$
	50	0.05	$4.5 \cdot 10^{-8}$	$0.1\text{-}10^2$	$G' \ll G''$
Pig skin 2.5	10	500	6.0	<20	$G' > G''$
	30	0.04	$3.0 \cdot 10^{-8}$	$0.1\text{-}10^3$	$G' \ll G''$
	50	0.04	$3.0 \cdot 10^{-8}$	$0.1\text{-}10^3$	$G' \ll G''$
Pig skin 3.0	10	1100	15.0	<14	$G' > G''$
	30	0.03	$3.0 \cdot 10^{-8}$	$0.1\text{-}10^3$	$G' \ll G''$
	50	0.03	$3.0 \cdot 10^{-8}$	$0.01\text{-}10^3$	$G' \ll G''$
Pig skin 4.0	10	1570	39.8	<5	$G' > G''$
	30	$2.8 \cdot 10^{-8}$	0.03	$0.1\text{-}10^2$	$G' < G''$
	50	$2.8 \cdot 10^{-8}$	0.03	$0.1\text{-}10^2$	$G' < G''$
Gellan gum 0.5	10	1.82	2.74	$<10^2$	$G' < G''$
	20	0.4	1.0	$<10^2$	$G' < G''$
	30	$4.0 \cdot 10^{-8}$	0.04	$<10^2$	$G' \ll G''$
Gellan gum 1.0	10	25	14.4	<20	$G' > G''$
	20	15.9	12.1	<10	$G' > G''$
	30	2.24	0.7	<2.2	$G' > G''$
	40	$5.8 \cdot 10^{-8}$	0.06	<2.2	$G' \ll G''$
	60	$4.0 \cdot 10^{-8}$	0.04	<2.2	$G' \ll G''$
Gellan gum 1.5	10	832	164	<2.2	$G' > G''$
	30	203	62	<3.2	$G' > G''$
	50	16.4	5.13	<6.8	$G' > G''$
	80	0.01	0.05	$<10^2$	$G' < G''$
κ-carrageenan 0.5	10	0.8	2.26	$<10^2$	$G' < G''$
κ-carrageenan 1.0	10	107	1.5	<40	$G' > G''$
	30	$1.2 \cdot 10^{-3}$	0.11	20-55	$G' < G''$
	50	$2.7 \cdot 10^{-3}$	$6.3 \cdot 10^{-2}$	15-28	$G' < G''$
κ-carrageenan 1.5	10	550	68.4	<10	$G' > G''$
	30	100	7.6		$G' > G''$
	50	$1.3 \cdot 10^{-7}$	0.014		$G' \ll G''$
Xanthan gum 1.0	10	5.73	2.62	<14.7	$G' > G''$
	30	6.51	3.02	<14.7	$G' > G''$
	50	5.93	3.92	<14.7	$G' > G''$
Xanthan gum 1.5	10	5.88	2.7	<21.5	$G' > G''$
	30	8.09	3.41	<31.6	$G' > G''$
	50	9.92	4.59	<33.6	$G' > G''$

Table 1: Amplitude Sweep data. Loss modulus, storage modulus and *VE* threshold *(γ_L)*, are shown for each gelatin, concentration and temperature.

TABLE 2. Frequency Sweep data

GELATIN [%wt]	T [°C]	G' [Pa]	G'' [Pa]
Pig skin 1.0	10	17.6	0.3
	30	$2.3 \cdot 10^{-8}$	0.025
	50	$2.3 \cdot 10^{-8}$	0.025
Pig skin 2.5	10	642	5.7
	30	$4.9 \cdot 10^{-8}$	0.02
	50	$7.6 \cdot 10^{-8}$	0.03
Pig skin 3.0	10	1230	13
	30	$3.0 \cdot 10^{-8}$	0.02
	50	$3.0 \cdot 10^{-8}$	0.02
Pig skin 4.0	10	2150	23.4
	30	$3.0 \cdot 10^{-8}$	0.04
	50	$3.0 \cdot 10^{-8}$	0.03
Gellan gum 0.5	10	4.7	4.7
	20	1.3	2.53
	30	$1.2 \cdot 10^{-7}$	0.13
Gellan gum 1.0	10	42	20.3
	20	29.8	20.3
	30	4.9	1.8
	40	$9.1 \cdot 10^{-8}$	0.1
	60	$9.1 \cdot 10^{-8}$	0.1
Gellan gum 1.5	10	943	173
	30	272	75.4
	50	19.7	7.1
κ-carrageenan 0.5	10	0.8	2.0
	30	0.5	1.4
	40	$1.3 \cdot 10^{-6}$	1.3
κ-carrageenan 1.0	10	120	28
	30	$1.3 \cdot 10^{-6}$	1.4
	50	$9.7 \cdot 10^{-7}$	1.1
κ-carrageenan 1.5	10	368	85.2
	30	55	25.2
	50	$1.3 \cdot 10^{-6}$	0.94
Xanthan gum 1.0	10	10.9	5.82
	30	11.0	5.82
	50	13.0	7.02
Xanthan gum 1.5	10	8.22	4.2
	30	8.26	4.6
	50	8.35	4.9

Table 2: Frequency Sweep data. The parameters G' and G'' are shown for each gelatin, concentration and temperature.

TABLE 3. Temperature Sweep data

GELATIN	Concentration [%wt]	T_g [˚C]	γ [%]	ω [rad/s]
Pig skin	1.0	5.7	10	10
	2.5	15.8	5	10
	4.0	19.9	10	10
Gellan gum	1.0	27.9	1	10
	1.5	44	1	10
κ-carrageenan	1.0	26	10	10
	1.5	32	10	10

Table 3: Temperature Sweep data. Gel temperature T_g is shown for each gelatin and concentration. The experimental frequency and strain are also included.

TABLE 4. Viscosity curve/Flow tests

GELATIN [%wt]	T [˚C]	$\dot{\gamma}$ [s^{-1}]	η [Pa·s]
Pig skin 1.0	60	0.01-100	0.3-0.002
	50	0.01-100	0.3-0.002
	40	0.01-100	0.6-0.002
	30	0.01-100	0.8-0.003
Pig skin 2.5	60	0.01-1000	0.1-0.002
	50	0.01-1000	0.1-0.002
	40	0.01-1000	0.2-0.002
	30	0.01-1000	0.4-0.003
Pig skin 3.0	50	10-100	0.3-0.003
	30	10-100	0.5-0.004
Pig skin 4.0	60	0.01-1000	1.2-0.02
	50	0.01-1000	1.2-0.02
	40	0.01-1000	2.0-0.03
	30	0.01-1000	2.0-0.03
Gellan gum 1.0	60	0.1-1000	0.5-0.02
	50	0.1-1000	1.4-0.02
	40	0.1-1000	2.2-0.02
Gellan gum 1.5	60	0.01-1000	5.0-0.05
	50	0.01-1000	5.0-0.06
Xanthan gum 1.0	50	0.1-1000	181-1.0
	30	0.1-1000	173-1.0
	10	0.1-1000	150-1.0
Xanthan gum 1.5	50	0.1-1000	174-1.0
	30	0.1-1000	154-1.0
	10	0.1-1000	133-0.04

Table 4: Viscosity curve/Flow tests data. Viscosity and strain rate are shown for each gelatin, concentration, and temperature.

TABLE 5.

GELATIN [%wt]	Q^{-1} (T=10°C)	Q^{-1} (T=30°C)	Q^{-1} (T=50°C)	δ[°] (T=10°C)	δ[°] (T=30°C)	δ[°] (T=50°C)
Pig skin 1.0	0.014	$1.1\cdot10^6$	$1.1\cdot10^6$	0.80	90	90
2.5	0.012	$1.1\cdot10^6$	$1.1\cdot10^6$	0.69	90	90
3.0	0.011	$1.1\cdot10^6$	$1.1\cdot10^6$	0.63	90	90
4.0	0.011	$1.1\cdot10^6$	$1.1\cdot10^6$	0.63	90	90
Gellan gum 0.5	1.50	3.134	$1.1\cdot10^6$	56.31	72.3	90
1.0	0.50	0.36	$1.1\cdot10^6$	26.43	20.0	90
1.5	0.18	0.26	0.30	10.09	14.6	16.65
κ-carrageenan 0.5	3.73	$1.1\cdot10^6$	-	75.00	90	90
1.0	0.34	$1.1\cdot10^6$	$1.1\cdot10^6$	18.93	90	90
1.5	0.41	0.53	$1.1\cdot10^6$	22.49	27.8	90
Xanthan gum 1.0	0.53	0.53	0.54	27.9	27.9	28.4
1.5	0.56	0.56	0.58	29.2	29.2	30.1

Table 5: Internal friction $Q^{-1} = G''/G'$ and damping factor δ for different gelatins and concentrations at fixed temperature and frequency (1 rad/s).

TABLE 6. Physical properties of gelatins.

GELATIN [%wt]	ρ (T=40°C) [g/cm^3]	ρ (T=4°C) [g/cm^3]	α [K^{-1}]	K [W/mK]	Transparency
Pig skin 1.0	0.9951	0.992		0.607	yes
2.5	0.9992	0.996	$2.88\cdot10^{-4}$	0.607	yes
3.0	1.0017	0.999		0.607	yes
4.0	1.0031	1.003	$3.16\cdot10^{-4}$	0.607	yes
Gellan gum 0.5	0.9941	0.994		0.607	yes
1.0	0.9960	0.997		0.607	cloudy
1.5	0.9982	1.000	$3.29\cdot10^{-4}$	0.607	cloudy
κ-carrageenan 0.5	0.9946	0.997		0.607	yes
1.0	0.9966	0.998		0.607	yes
1.5	0.9982	1.000		0.607	yes
Xanthan gum 1.0	0.9966	0.997		0.607	cloudy
1.5	0.9995	1.007		0.607	cloudy

Table 6: Physical properties of gelatins. Density in the sol-state (T = 40°C) and in the gel-state (T = 4°C), thermal expansivity, thermal conductivity and transparency.

Chapter 5

Seismic variability of subduction thrust faults: insights from laboratory models

Abstract

Laboratory models are realized to investigate the role of interface roughness, driving rate, and pressure on friction dynamics. The setup consists of a gelatin block driven at constant velocity over sand paper. The interface roughness is quantified in terms of amplitude and wavelength of protrusions, jointly expressed by a reference roughness parameter obtained by their product. Frictional behavior shows a systematic dependence on system parameters. Both stick-slip and stable-sliding occur, depending on driving rate and interface roughness. Stress drop and frequency of slip episodes vary directly and inversely, respectively, with the reference roughness parameter, reflecting the fundamental role for the amplitude of protrusions. An increase in pressure tends to favor stick-slip. Static friction is a steeply decreasing function of the reference roughness parameter. The velocity strengthening/weakening parameter in the state- and rate-dependent dynamic friction law becomes negative for specific values of the reference roughness parameter which are intermediate with respect to the explored range. Despite the simplifications of the adopted set-up, which does not address the problem of off-fault fracturing, a comparison of the experimental results with the depth distribution of seismic energy release along subduction thrust faults leads to the hypothesis that their behavior is primarily controlled by the depth- and time-dependent distribution

of protrusions. A rough subduction fault at shallow depths, unable to produce significant seismicity because of low lithostatic pressure, evolves into a moderately rough, velocity-weakening fault at intermediate depths. The magnitude of events in this range is calibrated by the interplay between surface roughness and subduction rate. At larger depths, the roughness further decreases and stable sliding becomes gradually more predominant. Thus, although interplate seismicity is ultimately controlled by tectonic parameters (velocity of the plates/trench), the direct control is exercised by the resulting frictional properties of the plate interface.

5.1 Introduction

Subduction thrust faults are the largest natural example of failure surface (Figure 1). Most of the global seismic energy is released by discontinuous slip along the frictional interface between the subducting and the overriding plate [e.g. Scholtz, 1990; Pacheco and Sykes, 1992]. The mechanical foundation of frictional behavior is the formula known as the da Vinci-Coulomb-Amontons friction law [Amontons, 1699; Coulomb, 1785], according to which friction is proportional to the applied normal load and independent of the apparent area of contact. Within this simple frictional model, the static friction coefficient (μ_s) is larger than the dynamic friction coefficient (μ_d) leading to a possibly unstable slip between the interacting moving surfaces.

However, standard frictional models need to be revised to properly describe the behavior characterizing subduction thrust faults. The interplate contact is seismogenic only in a specific depth interval [Scholz, 1998], which globally is comprised between 11±4 km and 51±9 km [Heuret et al., 2011; Figure 1a,b]. In several subduction zones, slow slip events are recognized just below the limit of the seismogenic zone, even if their physical mechanism still remains elusive [e.g. Schwartz and Rokosky, 2007; Gomberg et al., 2010]. Moreover, cumulative seismic moment (M') is not homogeneously distributed along the seismogenic zone, but shows an approximately Gaussian distribution with a peak around 20 – 30 km of depth (Figure 1c). The description of the

system requires a rate- and state- dependent frictional model where μ_d and μ_s depend upon velocity and ageing, respectively [Dieterich, 1979; Ruina, 1983]. Friction as a function of sliding velocity can be described using two parameters a, b, and a state variable θ accounting for memory effects at the contact surface, according to the relation

$$\mu = \mu_o + a \ln (V/Vo) + b \ln (V \theta/d_c) \tag{1}$$

where μ_o is the friction at the reference velocity V_o, V is the imposed velocity and d_c the critical slip distance [i.e. the slip distance necessary to change contact junctions; Dieterich, 1981]. When $a\text{-}b > 0$, the system is characterized by a velocity strengthening behavior with frictional resistance increasing with any applied velocity increase. Hence, a seismic rupture cannot propagate in this field. Earthquakes, in contrast, can nucleate if $a\text{-}b < 0$, which results in velocity weakening behavior [e.g. Scholz, 1998]. In the velocity-weakening field and at constant driving velocity, the stiffness of the system, K, should obey to the following relation to ensure stick-slip dynamics

$$K < K_c = W (b\text{-}a)/ d_c \tag{2}$$

where W is the normal load exerted on the sample and K_c is a critical stiffness value below which stick-slip oscillations can occur [e.g. Voisin et al., 2007].

While the rate- and state- friction law offers a simple mechanical explanation of intraplate earthquake nucleation, the exact physical basis controlling this behavior is still an argument of debate. It is generally accepted that the temperature range at which interplate seismogenic zones develop is from 100-150°C to 350-450°C [i.e. Hyndman and Wang, 1993; Wang, 1995, Hyndman et al., 1997; Currie et al., 2002]. On this basis, the updip limit of seismogenic thrust faulting is alternatively explained by the transition illite-smectite [Pytte and Reynolds, 1988] or by fault gouge lithification processes [Saffer and Marone, 2003; Marone and Saffer, 2007], while the downdip limit is possibly controlled by the brittle–ductile transition of the crustal material [i.e. Brace and Kohlstedt, 1980] or by the intersection of the slab with the forearc mantle wedge [Peacock and Hyndman, 1999].

The dynamical behavior of the seismogenic thrust fault, as of any other seismogenic fault, can also be described by the "asperity model" [Lay and Kanamori, 1981; Lay et al., 1982], according to which asperity size correlates positively with earthquake magnitude. Although the term "asperity" originally denoted a physical entity (a bulge on an otherwise smooth surface), it is often thought as a conceptual entity, i.e. a region of increased strength on the fault plane [Byerlee, 1970; Scholz and Engelder, 1976] dominated by stick-slip behaviour, and/or a location of high slip during an earthquake [Lay and Kanamori, 1981; Lay et al., 1982]. What can cause an asperity is even more elusive: upper plate strength, frictional variation within the fault zone, and subducting plate features have all been considered valid ingredients [see Bilek et al, 2007 for a review]. While the importance of protrusions in controlling the behavior of the subduction thrust fault is generally recognized, there is still relatively little understanding of the way frictional motion varies with asperity size and distribution.

In this paper, we present a laboratory study of the role played by the distribution of contact roughness in friction dynamics. We show how it is possible to reconcile the physical and the seismological meaning of asperity, combining experimental observations into a simple description of subduction thrust fault behavior. For this purpose, spring-block-like models [e.g. Burridge and Knopoff, 1967; Voisin et al., 2008] have been realized as analogs of the subduction thrust fault. Our models introduce the following new features: (a) using a gelatin slider reproducing the complex visco-elasto-brittle rheology representative of a properly scaled crustal/lithospheric behavior [Di Giuseppe et al., 2009] and, therefore, specifically taking into account the time-dependence of the interseismic deformations; (b) testing a wide range of contact materials with roughness profiles characterized by well-sorted protrusions; (c) investigating the effect of lithostatic pressure at seismogenic depths; d) exploring both frictional static and rate- and state- effects.

After a description of the experimental procedure, we show how the static friction depends on the real contact surface (i.e. the small portions of the area where roughness irregularities are in contact with the gelatin sample) and how the velocity dependence of the steady-state friction varies

98

with the spacing and amplitude of the geometric irregularities distributed along the rupture surface. Moreover, we show that the maximum characteristic stick-slip event obtained in each experimental run depends both on the roughness of the contact surface and the mass and velocity of the slider. Our experimental results are used to propose a physical interpretation of the seismic regimes along the subduction thrust plane [as described e.g. by Scholz, 1998].
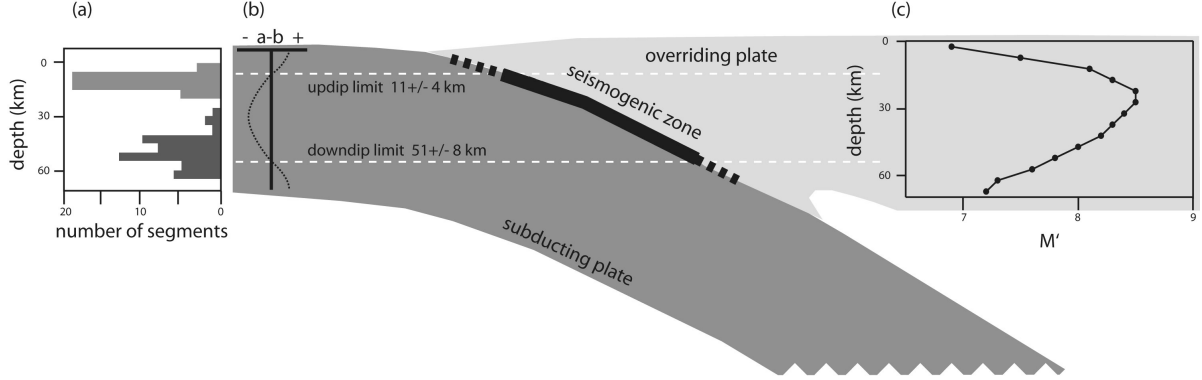
Figure 1: Schematic representation of a subduction fault with: (a) histogram showing the seismogenic zone depth limits (worldwide statistics from 46 subduction segments based on thrust event hypocenters distribution; Heuret et al., 2011); (b) model for the friction stability parameter, *a-b*, as a function of depth [e.g. Scholz 1998]; (c) cumulative moment (converted to a magnitude-like value M' using the Kanamori 1977 moment-magnitude relation) for thrust events with $5.5 \leq Mw \leq 7.5$ as a function of depth for the 1976 – 2007 period. Subduction thrust events have been extracted from the CMT Harvard catalog [Dziewonski et al., 1981]. Location of the Harvard events has been improved using the EHB hypocenter catalog [Engdahl et al., 1998]. See Supplementary material for a comprehensive description of sampling criteria and details on data processing.

5.2 Experimental setup

5.2.1 Apparatus

Spring-blocks [e.g. Burridge and Knopoff, 1967; Baumberger et al., 1994; Vargas et al., 2008] are simplified models reproducing the seismic cycle, where the block-basement interface represents a generic fault and the spring stiffness represents the elastic properties of the surrounding medium. In this work, we used a spring-block-like setup where the elastic strain is directly stored in the

gelatin block without the necessity to include a real spring. The experimental setup thus consists of an isothermal device in which a gelatin block of mass 182 g is forced to slide over a 30 cm long frictional horizontal surface with protrusions. For clarity, we hereafter use the term "protrusions" to describe the geometrical irregularities on the contact surface (see discussion in Section 2.2) while the term "asperities" is used in the seismological sense (i.e. referring to areas of large slip). A schematic view of the system is shown in Figure 2. After its preparation, the gelatin block is shaped as a parallelepiped ($8.5 \times 5.3 \times 4$ cm^3) and positioned in a rigid holder. The bottom layer of the gelatin (thickness 0.2 cm) is left free, allowing the localization of the deformation related to sliding. This configuration has been selected as giving the best control of the frictional contact surface, minimizing possible boundary effects and ensuring the most regular and reproducible dynamical behavior of the experimental system. The gelatin-holder is coupled by means of a steel cable to a stepping motor moving at a constant velocity. The shear force required to move the gelatin block is measured through a digital force sensor characterized by an accuracy of 0.02 N and a sampling rate of 1 Hz. Since the steel cable can be assumed to be inextensible and the digital force sensor stiffness is much higher with respect to the gelatin sample, the elastic strain is stored in the sand paper-gelatine contact characterizing the bottom layer of the system.
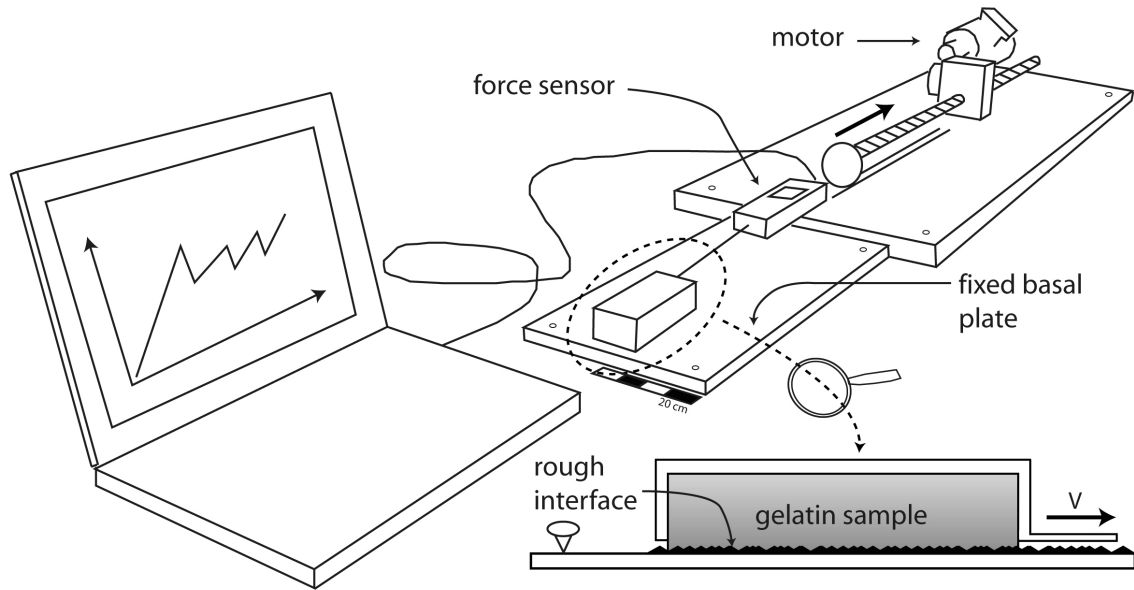
Figure 2: Line drawing of the experimental setup. A gelatin slider of size $8.5 \times 5.5 \times 4$ cm^3, in contact with a rough surface with variable spacing and amplitude of irregularities, is driven at constant velocity V. A digital force sensor measures the shear force exerted on the slider.

5.2.2 Materials

We use gelatin and sand paper as analogs of lithosphere and subduction fault, respectively. The selected gelatin is prepared diluting small percentages (2.5%wt) of pig skin powder, an animal biopolymer, in distilled water which is stirred for 30 min at the preparation temperature of 60°C. The mixture is then poured in the mould and left for 24 hours at the temperature of 10°C, resulting in the formation of a gel (i.e. solid) state. This material properly scales for length, density, stress, and viscosity in the natural gravity field [cf. Weijermars and Schmeling, 1986 for a discussion of scaling procedure].

In particular, pig skin 2.5%wt gelatin at 10°C satisfies two necessary conditions characterizing a viscoelastic solid: (a) G' and G'', which are standard rheological quantities defining the stored

and dissipated energy respectively [e.g. Nelson and Dealy, 1993], are about the same order of magnitude (i.e. the elastic deformation counterbalances the viscous one); and (b) G' > G'' [cf. Di Giuseppe et al., 2009 for a detailed discussion].

The spring-block model is designed using a nature/model length scale, L^*, of 6.4 x 10^5 (i.e. 1 cm in the model corresponds to 6.4 km in nature). This scaling factor is derived by assuming that viscous stress in the analog material scales with lithostatic pressure [see eq. 7 in Di Giuseppe et al., 2009]. For models performed in natural gravity field, the stress scaling factor, σ^*, can be obtained from the relation

$$\sigma^* = \rho^* \bullet L^* \tag{3}$$

where ρ^* is the nature/model density scale factor. Since pig skin 2.5%wt gelatin density is about 1000 kg m^{-3} and the average upper crustal density is 2700 kg m^{-3}, we have $\sigma^* = 1.7$ x 10^6 (1 Pa in the model corresponds to 1.7 MPa in nature).

For the above stress scaling factor the experimental shear modulus, ranging between $10^3 - 10^4$ Pa depending on material ageing, is properly scaled with the natural prototype (~ 10^{10} Pa). The experiments are therefore appropriate to model the elastic component of the lithosphere.

The timescale is set using the relation

$$t^* = (t_n/t_m) = (\sigma_m/\sigma_n) \cdot (\mu_{n/}\mu_m) = [(\rho \cdot g \cdot L)_m/(\rho \cdot g \cdot L)_n] \cdot (\mu_n/\mu_m) \tag{4}$$

which gives $t^* = 1.2*10^{11}$ assuming a lithospheric viscosity of 10^{19} Pa s and considering the model complex viscosity of 50 Pa s [Di Giuseppe et al., 2009]. Hence, the experimental time of few seconds corresponds to thousands of years in nature. The resulting velocity scaling factor, V^* (derived as the length scaling factor L^* divided by the time scaling factor t^*), is $5.5*10^{-6}$ so that the experimental loading rate (0.2-2 cm/min) scale to approximately $0.6 - 6$ cm/yr in nature. This timescale confirms that the model material is correctly scaled for the relatively long sticking/interseismic period, while a secondary scaling should be adopted to properly define the coseismic time [Rosenau et al., 2009]. The gelatin is characterized by a Maxwell time of ~45 s. The material thus responds as a viscoelastic solid during the interseimic phase, and it is mainly elastic

during the few seconds characterizing the slip phase. The rheological properties of gelatin are a fundamental factor to obtain a comprehensive model throughout the entire earthquake cycle including the interseismic viscoelastic deformation [e.g. Rice, 1993; Lapusta, et al. 2000].

The fixed basal plate, analog of the subduction fault, is covered by various types of sand paper. Sand paper has been selected from a variety of contact materials for the regularity and reproducibility of its frictional properties. This choice allows the study of frictional behavior as a function of the size and distribution of contact protrusions. For this purpose, we prepared a wide range of sand papers using classed abrasive material (silicon carbide) glued to impermeable paper. The roughness of the contact material is quantified as a deviation from straightness consisting of amplitude (i.e. topographical variations of peaks and valleys) and wavelength (i.e. distance between peaks). Both parameters are crucial to a quantitative description of surface roughness when studying frictional constitutive parameters [Marone and Cox, 1994]. To account for topographical variations, we adopt the peak-to-valley mean height roughness Rmh, defined as [Choi et al., 2007]

$$Rmh = \frac{1}{Mp}\sum_{i=1}^{Mp} Zi - \frac{1}{Mv}\sum_{k=1}^{Mv} Zk \tag{5}$$

where Mp and Mv are the total number of peaks and valleys respectively, and Z is the corresponding height. The wavelength λ has been characterized measuring the average distance between peaks. Data are collected along 5 cm long linear profiles parallel to the direction of sliding using microscopic analysis (resolution 2.6 μm) and post-processed with an ad-hoc commercial software (Optimas 6.5). Rmh in the selected sand papers ranges between 0.100 ±0.011 and 0.013 ±0.001 mm, while λ is comprised between 0.714 ±0.068 and 0.029 ±0.002 mm (Table 1). In sandpapers, the size and wavelength of protrusions are usually positively correlated (Table 1). However, deviation from this trend are available (samples #3 and 6), providing important additional constraints. To describe univocally both the amplitude and the wavelength of the protrusions with a single parameter, we define the reference roughness parameter, $Rmh*\lambda$. Adopted $Rmh*\lambda$ values range between 0.0714 and 0.0004 (Table 1). For crustal faults, field studies suggest that geometrical irregularities are

103

characterized by a wavelength which relates to amplitude with a ratio of 100 – 1000 [e.g. Power et al., 1988; Renard et al., 2006; Sagy et al., 2007]; however, no strict geometrical relationship can be assumed between the experimental roughness and the weakly constrained natural prototype. The experimental subduction fault simulates a natural prototype characterized by protrusions of vertical height varying from a few to about one hundred meters, representing a pervasive small-scale roughness. Our choice is supported by the recognized role of small-scale features in tuning the overall bathymetry [Jordan, et al., 1983; Abers et al., 1988; Smith and Jordan 1988] and, in turn, the "characteristic" seafloor roughness, which is estimated to be in the 100 – 300 m range [Hayes & Kane, 1991]. As a counterpart, we are forced to consider only moderately sized earthquakes since greater events are supposed to require either the rupture of larger asperities [e.g. Cloos, 1992; Seno 2003] and/or along-strike rupture propagation [e.g. Ruff, 1989; McCaffrey, 2007, 2008].

Table 1: Parameters characterizing the experimental materials: sand-paper asperity distribution (means ± standard errors) and gelatin physical/rheological properties.

material properties				
Sand paper	sample n.	Rmh [mm]	λ [mm]	Rmh * λ [mm^2]
	1	0.100 ±0.011	0.714 ±0.068	0.0714
	2	0.093 ±0.009	0.373 ±0.023	0.0347
	3	0.068 ±0.006	0.202 ±0.016	0.0137
	4	0.038 ±0.004	0.143 ±0.009	0.0054
	5	0.029 ±0.003	0.087 ±0.007	0.0025
	6	0.018 ±0.002	0.103 ±0.006	0.0019
	7	0.021 ±0.002	0.040 ±0.003	0.0008
	8	0.016 ±0.001	0.035 ±0.002	0.0006
	9	0.013 ±0.001	0.029 ±0.002	0.0004
Pig skin 2.5%wt gelatin	sample n.	density [kg/m^3]	shear modulus [Pa]	temperature [°C]
	1	~1000	~1000	10

5.2.3 Experimental procedure

Models are run in a thermally insulated room maintaining constant working temperature (10°C) and humidity, necessary conditions for the rheological control of gelatins. Since the models are designed to study the dependence of friction on the contact surface roughness, we systematically vary the fixed basal plate using nine different sand papers (Table 1). A new gelatin sample is used for each run in order to minimize possible ageing and wear effects (a specific experimental study on these effects has been presented by Voisin et al., 2007).

The experimental procedure consists of pulling the slider at a constant velocity, increasing the shear force until the gelatin block begins to slide. As a characterization of the tribological properties of the system, we measure the static and kinetic coefficients of friction (μ_s and μ_d, respectively) and *a-b* (see equation 1). The reading on the force gauge when the block begins to slide is a measure of μ_s, while the reading while the block is sliding is a measure of μ_d. Moreover, in order to correlate experimental observations with seismological quantities, we determine stress drop $\Delta\sigma$ and number of stick-slip phases (i.e. earthquakes) occurring within a fixed sliding distance once the steady-state regime is reached. The stress drop is obtained by dividing the experimental force drop by the gelatin trailing edge area.

A first set of models is used to measure μ_s on the contact surface between the gelatin and the different sand papers. Each model consists of a set of three runs performed with different masses of the sliding block (Table 2). The fixed mass of the gelatin is increased by adding calibrated masses atop the slider. We choose additional masses to scale the pressure acting at the interface with the lithostatic pressures operating at shallow, intermediate and deep depths along the subduction thrust fault (24 km, 43 km, and 64 km, respectively; Table 2), neglecting the contribution of the pore fluids pressure. We verified that under these conditions, the plastic yield stress of the gelatin is never exceeded. The static friction coefficient μ_s is determined for each sand paper, by measuring the force required for moving the sample under the applied normal pressure (i.e. from the slope of

the regression line between shear stress and normal stress, normalized by the sample's areas on which these forces act).

In a second set of models, the influence of the contact roughness profile on *a-b* was investigated by performing dynamic friction (i.e. velocity stepping) tests at variable normal loads (381 Pa, 675 Pa, 991 Pa; Table 2) and variable driving rates (four velocities tested: 0.2 cm/min, 0.6 cm/min, 1.2 cm/min, and 2 cm/min, corresponding to 0.6 cm/yr, 1.8 cm/yr, 3.6 cm/yr and 6 cm/yr in nature; Table 2). The *a-b* value is derived from the log-linear correlation between dynamic friction coefficient (estimated on the basis of the residual stress) and velocity [Scholz, 1998; Rosenau et al., 2009].

At the end of each run, the morphological evolution of the gelatin contact surface is examined using a 3D laser scan, to verify that wear did not affect the sample.

Table 2: Experimental conditions: velocity and normal pressure ranges.

experimental conditions				
	V 1	V 2	V 3	V 4
velocity range [cm/min]	0.2	0.6	1.2	2.0
	NP 1	NP 2	NP 3	
normal pressure range [Pa]	381	675	991	

5.3 Experimental results

The common behavior of each model shows an initial linear increase of the shear force while the slider is at rest ("initial stick-phase"; Figure 3). This phase corresponds to the elastic response of the gelatin. When the critical value is reached, the shear force suddenly drops while the block starts to move. Once the sliding is initiated, the system can exhibit two dynamical regimes:

(a) Stick-slip behavior, where the shear force shows a see-saw profile characterized by increases occurring when the gelatin block "sticks" on the contact sand paper, and abrupt decreases when the block slides (Figure 3). Slip phases are associated with the propagation of self-healing

pulses originated at the trailing edge of the gelatin slider and emerging at the leading edge [cf. e.g. Rubio and Galeano, 1994; Baumberger et al., 2003].

(b) Stable sliding, characterized by a continuous sliding of the gelatin sample over the sand paper (Figure 3).
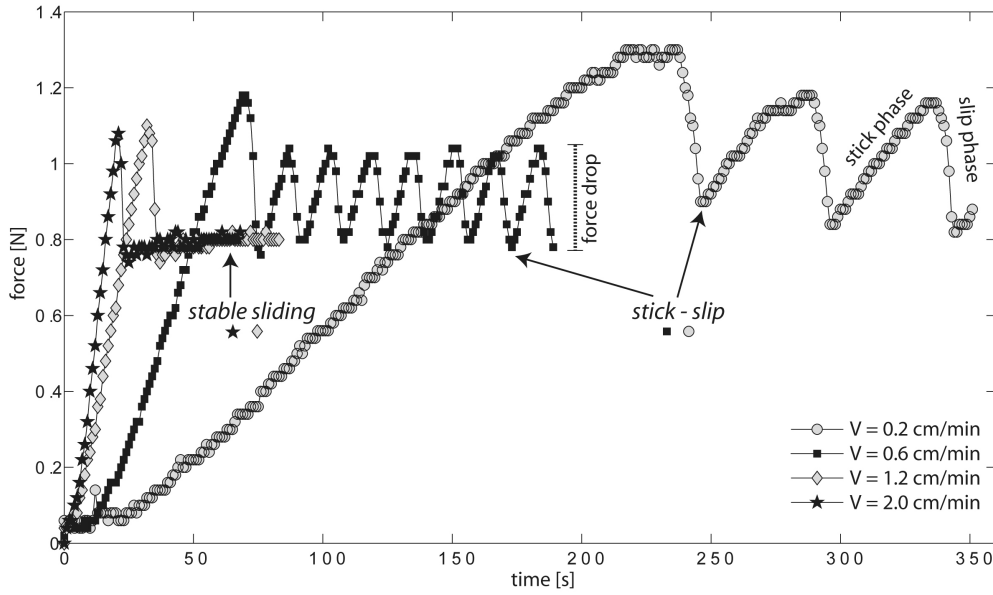
Figure 3: Typical time series of shear force values recorded by the digital force sensor for a gelatin-sand paper system characterized by $Rmh*\lambda = 0.0714$ mm^2, a normal load of 381 Pa, and variable driving velocities indicated by different markers. The dynamical behavior of the system shows a bifurcation as a function of driving rate: stick-slip at low driving velocity (V=0.2-0.6 cm/min); stable sliding at high velocity (V=1.2-2.0 cm/min). The stable sliding regime occurs when the recorded force readings do not change within a range of ±0.02 N in the sampling window (1 s).

The controlled asperity distribution of each sand paper and the lack of wear on the gelatin contact surface result in reproducible behavior over the imposed deformation cycle. For stick-slip behavior, the initial shear force peak is consistently higher than the following ones (Figure 3). Spring-block models focused on friction at gel-glass interface show that there exists a logarithmic dependence of the yield strength on the sticking time [i.e. interfacial ageing; Baumberger et al., 2002]. During the sticking phase, polymer chains get pinned to the track through adhesive bonds resulting in a strength increase. Upon sliding, bonds have only a finite lifetime and their number

107

decreases resulting in a weakening. A similar behavior has been observed in granular media/natural rocks where strain hardening occurs prior to failure and is followed by strain softening as result of compaction–decompaction cycles [Lohrmann et al., 2003].

For any given gelatin-sand paper system, the driving rate is an important controlling factor (Figure 3). Increasing driving rate increases the frequency of slip episodes, tending to stable sliding after a single shear force drop. For a given block mass and driving rate, the magnitude of characteristic events and their recurrence time scale directly and inversely, respectively, with the reference roughness parameter, $Rmh*\lambda$, with a major control exerted by the size of protrusions (Figure 4a-d). In particular, the amplitude and frequency of stick-slip episodes change by ~ -60% and +50%, respectively, for a $Rmh*\lambda$ decreasing from 0.0714 to 0.00056 mm^2 (Figure 4e-f). The inverse correlations between the magnitude of characteristic events and their recurrence time (Figure 4a-d) highlights the invariance of the seismic coupling during the evolution of the model.
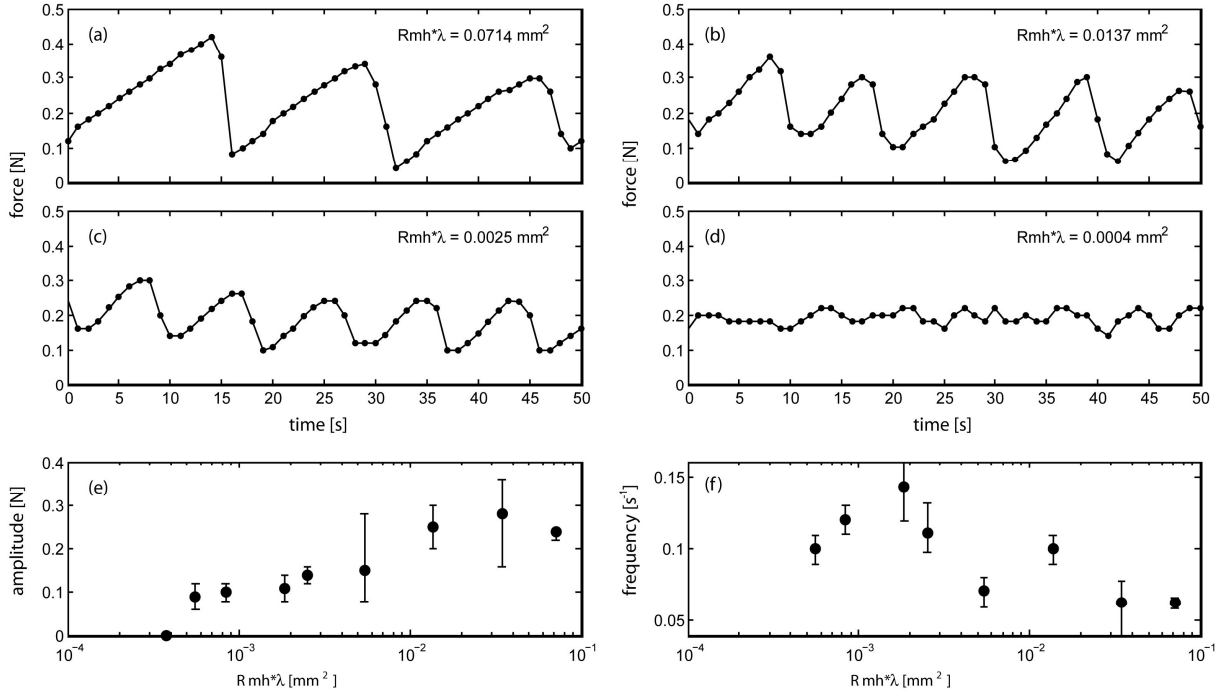
Figure 4: (a-d) Typical time series of shear force values for a gelatin-sand paper system characterized by a normal load of 381 Pa, driving rate of 0.6 cm/min, and variable $Rmh*\lambda$ (arranged in the order of decreasing $Rmh*\lambda$). (e-f) Variations of stick-slip amplitude (i.e force drop) and frequency with $Rmh*\lambda$ under the same experimental conditions.

The overall behavior, however, is more complex when all the system variables are taken into account. Figure 5 shows the dependence of stress drop, $\Delta\sigma$, and dynamical regime on the mass of the sliding block and its velocity for six reference sand papers. While $\Delta\sigma$ is usually largest for sand papers characterized by the highest Rmh, it is clear that Rmh is not the exclusive controlling factor. The largest $\Delta\sigma$ (278 Pa) is observed for $Rmh = 0.068$ mm and $\lambda = 0.202$ mm, highlighting the importance of the interplay between amplitude and wavelength of asperity distribution along the contact surface in tuning stick-slip behavior. This observation is supported by the fact that a contact surface characterized by a comparable Rmh but sparser asperites results in lower $\Delta\sigma$ (see Table 1).

An increasing stress drop with increasing normal load is commonly observed, and follows from the stability criterion (eq. 2), In particular, experimental results confirm that $\Delta\sigma$ increases with increasing normal load and decreasing driving rate for 0.0019 mm^2 $< Rmh*\lambda < 0.0714$ mm^2. In the

same roughness range, increasing the driving rate and/or decreasing the normal load cause the sliding dynamics of the system to shift from the stick slip to the stable sliding regime. For $Rmh*\lambda <$ 0.0019 mm^2, the behavior of the system becomes independent of both the mass and velocity of the gelatin block and shows stable sliding (within instrumental resolution) at all experimental conditions.
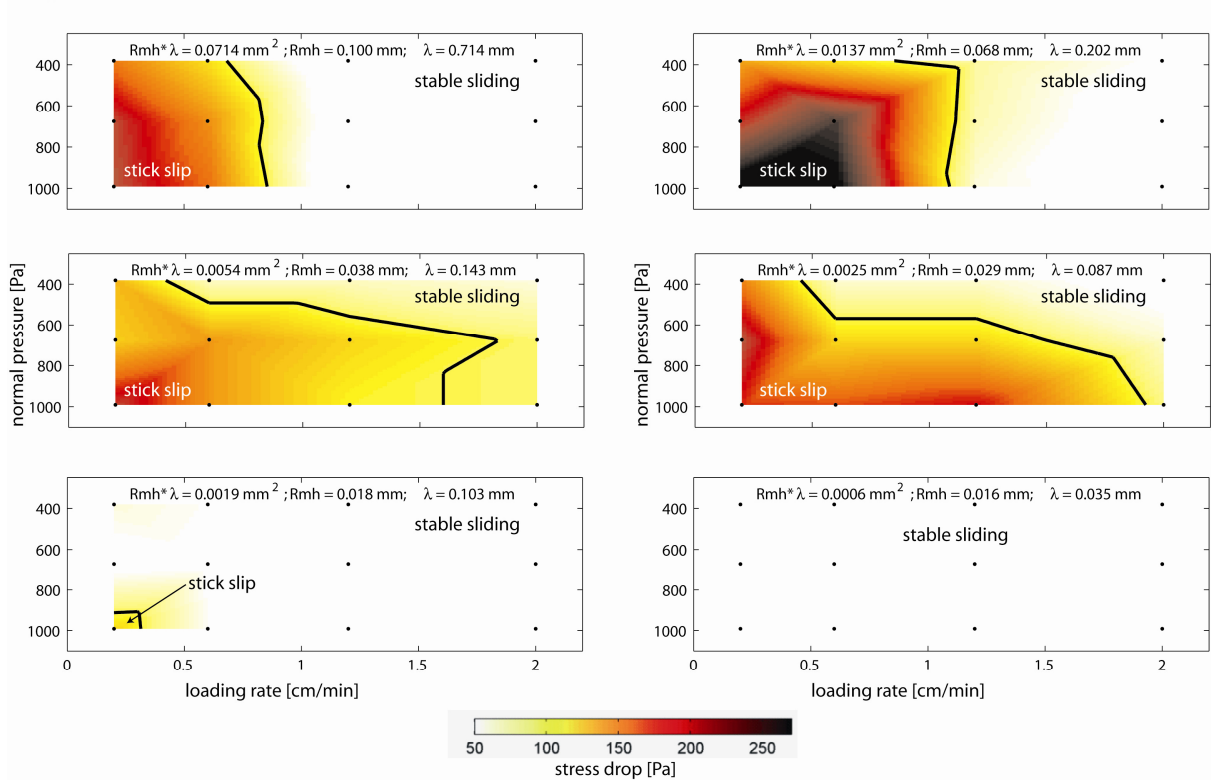
Figure 5: Phase maps of frictional dynamics in the driving rate-normal load space for gelatin-sand paper systems characterized by different roughness profiles. Panels are arranged in the order of decreasing $Rmh*\lambda$. Small black dots indicate measurement steps. Stress drop scale at the bottom.

From the typical time series recorded in the experiments, we quantify the frictional process by measuring μ_s, μ_d and a-b (Figure 6). We find that μ_s is strongly dependent on the roughness parameter, rapidly increasing from 0.24 to ~ 1 for $Rmh*\lambda < 0.0006$ mm^2 and decreasing to $\mu_s <$ 0.22 for $Rmh*\lambda > 0.0025$ mm^2 (Figure 6a). In the same range, the frictional parameter a-b in the rate and state friction law varies from 0.099 to $-$ 0.08, showing a nonlinear dependence on the contact surface roughness profile (Figure 6 panels b and d). The difference is negative (i.e. unstable

velocity weakening regime) for $Rmh*\lambda \geq 0.0054$ mm^2, and becomes positive (stable velocity strengthening regime) values for $Rmh*\lambda \leq 0.0054$ mm^2 (Figure 6b).
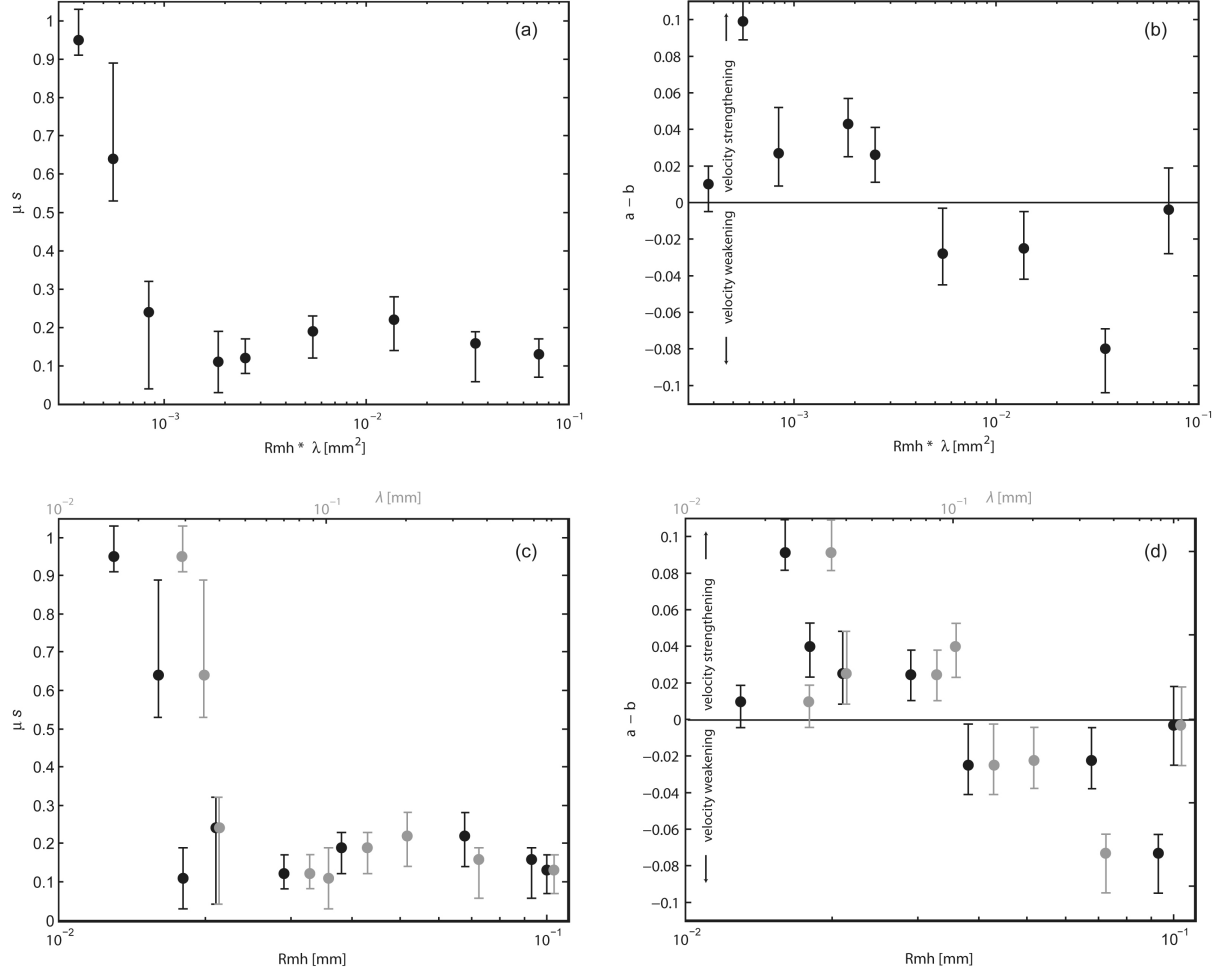
Figure 6: Diagrams showing the relations between: (a) static friction μ_S and $Rmh*\lambda$; (b) friction velocity dependence parameter a-b and $Rmh*\lambda$; (c) μ_S and Rmh (black dots) and μ_S and λ (gray dots plotted on the supplementary horizontal axis on the top of the panel); (d) a-b vs. Rmh (black dots) and λ (gray dots plotted on the supplementary horizontal axis on the top of the panel). Panels c and d are show the individual role of Rmh and λ in tuning the frictional parameters. The error bars are constrained by the minimum and maximum values obtained from different (at least four) runs. The parameter a-b is measured in the 1.78 – 4.63 N normal load range.

5.4 Discussion: relevance to seismic behavior

5.4.1 Control of experimental parameters on slip regime

We have tested how interface roughness (i.e., size and wavelength of protrusions), mass (i.e., pressure) and velocity of a sliding block of gelatin over sand paper affect frictional behavior. The analysis gives some general insights into salient features of low-velocity frictional dynamics. The magnitude of the static friction, the character of the frictional motion, and the magnitude of the stress drop are sensitive to the system parameters.

Static friction is inversely related to $Rmh*\lambda$ (Figure 6a; Table 1). The smoothest interfaces show the highest static friction and the greatest tendency for unstable slip [e.g. Marone and Cox, 1994]. This confirms the adhesion friction model [also called plastic junction model; Bowden and Tabor, 1950] which assumes that static friction is related to the real contact area (i.e. asperity contact characterizing irregular surfaces). A similar behavior, occurring when several frictional resistances - shear friction, indentation and plounghing force to groove the contact surface [e.g. Byerlee, 1967; Scholz and Engelder, 1976 for description of mechanisms related to rock friction] - are active, reduces to the classic da Vinci-Coulomb-Amontons friction law for undeformable surfaces. In this view, a perfectly flat and undeformable contact surface (i.e. glass) would produce the highest static friction [Baumberger et al., 2002]. However, the frictional strength in our experiments is also inversely related to the driving rate [Figure 4; Heslot et al., 1994; Baumberger et al., 2003]. Following Baumberger et al. [2003], we speculate that the static friction of our gelatin-on-sand paper system is tuned by the intrinsical nature of the physical contact and, in particular, by the capability of the gelatin polymeric chains to establish and maintain adhesive bonds with the underlying material. For comparable sample ageing, the density/unit area of the polymeric chains forming bonds with the sand paper increases with the number of contact points. This process is controlled by the roughness contact profile, but is also favored by slow driving rate applied to the system [e.g. Engelder and Scholz, 1976; Charitat and Joanny, 2000]. The increase of the threshold

stress with time necessary to overcome the static frictional resistance (Figure 3) is the clearest manifestation of this ageing effect and can be speculatively compared to natural faults ageing/healing (e.g. Marone et al., 1995).

The models exhibit two different dynamical regimes, stick-slip and stable sliding, once the static frictional resistance is overcome (Figures 4 and 5). Stick-slip is enhanced by sharper contact surfaces (i.e. higher $Rmh*\lambda$), lower sliding velocities and higher pressures (Figure 5). In particular, we verified that the stiffness of the system, K, is lower than the critical value Kc (see equation 2) only for a specific interval of $Rmh*\lambda$. In the same interval, a-b is negative.

The transition from stick-slip to stable sliding appears to be primarily controlled by Rmh, which tunes the maximum stress drop possible in the system. Regular stick-slip instabilities occur only for contact surfaces with $Rmh > 0.018$ mm. In this field, slips can nucleate and easily propagate (i.e. a-$b < 0$) only when 0.03 mm $< Rmh < 0.095$ mm, otherwise the propagation is rapidly inhibited (i.e. a-$b > 0$; Figure 6b). The dynamic regime switches to stable sliding and velocity strengthening behavior for $Rmh < 0.03$ mm.

The role played by pressure and driving rate seems to be secondary, although not negligible. Independently from the roughness of the contact surface, stable sliding is always achieved for the lowest normal loads and the highest sliding velocities. This behavior can be interpreted by assuming that Rmh and the vertical pressure are factors controlling the magnitude of adhesive bonds of the gelatin polymeric chains. The influence of the normal stress in tuning the stress drop changing from stable sliding to stick-slip behavior is similar to what is observed for rock-rock friction [e.g. Byerlee, 1970; Scholz et al., 1972; Engelder, 1978].

The effect of the driving rate is probably linked to the finite lifetime of the adhesive bonds and their potential to re-stick after the occurrence of self-healing slip pulses [Baumberger et al., 2002]. At large velocities adhesive bonding becomes negligible and the dynamics of the system is determined by the viscous drag of the gelatin [Bird et al., 1987].

Another important observation is the nonlinearity of *a-b* (Figure 6b), already recognized in rock friction [e.g. Dieterich. 1981; Biegel et al., 1989; Marone and Kilgore, 1993]. We interpret the nonlinearity of *a-b* as depending on the relative weight of two competing factors, amplitude and spacing of protrusions, which in nature can be viewed as two aspects of the time dependence of rock strength. The former tunes the magnitude of the slip event [e.g. Ruff and Kanamori, 1983], the latter controls the capability to transmit the triggered deformation along the rupture plane and is linearly related with the critical slip distance [Ohnaka, 2003]. In this view, we speculate that just after the initiation of the slip phase, the geometry of the contact surface determines whether protrusions behave as "asperity-like" or "barrier-like" structures [Aki, 1984], promoting or inhibiting slip propagation, respectively. In the upper limit, a large amplitude and long wavelength roughness profile generates an initial large slip which propagates for a relatively long distance before reaching the neighboring protrusion. The initial signal is unable to overcome the resistance offered by this protrusion, which behaves as a barrier. In the lower limit, a low amplitude and short wavelength roughness profile tends to a flat surface, having a number of contact points above a critical frictional threshold and, consequently, favoring stable sliding. Hence, only surfaces having intermediate amplitude and wavelength roughness profiles can properly simulate a self-sustaining stick-slip process. In particular, we find experimentally that the protrusions amplitude and spacing for stick-slip ranges between 0.10 - 0.038 mm (which is equal to 65 – 25 m in nature) and 0.714 – 0.143 mm (which is equal to 450 – 90 m in nature), respectively.

5.4.2 Implications for subduction zone seismogenesis

Although our simplified models are not intended to reproduce the detailed seismic record of any particular fault and do not address the significant effects of off-fault fracturing on the seismic processes (Wang et al., 2010a), the experimental observations are qualitatively applicable at all scales, highlighting some key features of the seismogenic process. We concentrate our attention on

the depth-dependent behavior of the subduction fault, for which the models have been specifically designed and scaled.

Figure 7 shows the cumulative magnitude of moderately sized earthquakes (M_w 5.5-7.5) occurring along worldwide subduction interplate faults in the 1976 – 2007 period, as a function of depth and subduction velocity [Heuret et al., 2011; see the Supplementary Material for a comprehensive description of sampling criteria and details on data processing]. Despite the short length of the time record [McCaffrey, 2008; see Supplementary Material], this information catches the essence of subduction fault behavior. Seismic energy release is maximum in the 20-35 km depth interval. Moreover, seismic energy release is systematically lower for slower subduction velocities.

A qualitative comparison between experimental and natural data (Figures 5 and 7) shows interesting similarities. Low energy release correlates with low normal load. This suggests that low overburden pressure can be a factor controlling the updip limit of significant subduction seismicity. Moreover, the experimental negative relation between energy release (i.e. stress drop) and driving rate (Figure 3) for intermediate-high values of the latter parameter is consistent with the nonlinear relation between seismicity in subduction zones and relative plate velocity. This observation highlights the complex role played by subduction velocity in tuning seismic interplate behavior, explaining why faster subduction zones (i.e. Tonga, New Hebrides) are not associated with powerful activity [Pacheco and Sykes, 1992; Pacheco et al., 1993; Gutscher and Westbrook, 2009; Heuret et al., 2011].

The lack of correspondence between natural and experimental frictional behavior for low sliding/subduction velocities is probably related to the impossibility for the real case to sample a complete seismic cycle (>100 Myr long, Gutscher & Westbrook, 2009; see Supplementary material). Additional problems are represented by our experimental limitations which neglect the role of temperature, and by the impossibility for our gelatin-sand paper system to reproduce the depth variations of seismogenic behavior by varying only normal load and driving rate for a single roughness profile. If the roughness profile of the subduction fault is an ingredient for interplate

seismic activity, its properties must change with depth (and possibly with time and plate subduction; i.e. with total accommodated displacement) to justify the observations. A qualitative account of subduction thrust seismicity would consist of the following elements:

(1) A rough fault at shallow depths, unable to produce significant seismicity because of low lithospheric pressure [see Figure 5; Das and Scholz, 1983], with a seismologically conditionally stable roughness profile (Figure 6b);

(2) A moderately rough, velocity-weakening fault at intermediate depths, able to produce seismic events whose magnitude is calibrated by the interplay between Rmh, λ, normal load, and subduction velocity;

(3) A smooth, velocity-strengthening fault at larger depth, showing transitional behavior from shallower stick-slip to deeper stable sliding.

We thus suggest that the change from stable sliding to stick-slip and, again, to stable sliding observed in natural subduction zones (Figure 1 and 7) can be a consequence of simple frictional processes driven by the characteristics of depth- and time-dependent subduction fault protrusions. The proposed interpretation seems feasible since the frictional contact properties between the subducting and the overriding plates depend on deformation, temperature and pressure, which lead to downdip changes in porosity, permeability, pore-fluid pressure and comminution. These factors result in changes in the roughness profile of the subduction fault.

A similar model has been proposed by Voisin et al. [2007], who using frictional salt-on-glass models found a progressive change from stick-slip to stable sliding occurring over several deformation cycles, concomitant with the morphological evolution of the contact surface produced by physico-chemical aging. In nature, progressive rock comminution during the evolution of active faults has been observed and constrained at smaller scales [Storti et al., 2007; Sagy et al., 2007; Balsamo et al., 2010; Brodsky, 2010]. Its relation with stress drop has been experimentally simulated with granular flow models [e.g. Higashi and Sumita, 2009]. Similar factors can play a role in subduction thrusts, favored by dehydration reactions in the subducting lithosphere [e.g. Pytte

and Reynolds, 1988], changes in lithification state [Marone and Scholz, 1988, Marone and Saffer, 2007] and diagenetic processes [Moore and Saffer, 2001]. Thus, the initially rough profile of the lithosphere at the trench will be gradually smoothed as subduction evolves, minimizing roughness fluctuations with depth [Wang, 2010a]. However, this process is controlled not only by the inherited seafloor topography of the slab's surface and trench fills [see Bilek, 2007 for a review] but also by the geometry and kinematics of the subducting system. The dip of the slab and the velocity of subduction regulate the state of stress on the interplate thrust fault. This interpretation is confirmed by an analysis of 100 years of global seismicity, showing that velocity of subduction and seismogenic zone geometry and energy release are correlated [Heuret et al., 2011].

The interpretation proposed here qualitatively accounts also for the capability of the subduction fault to reproduce the Gutenberg-Richter magnitude-frequency law [Gutenberg and Richter, 1954]. Events of different size are characterized by different temporal cycles (Figures 3 and 4). This results confirm a common feature of frictional dynamics observed in laboratory models [e.g., Baumberger et al., 1994; Vargas et al. 2008] and theoretical calculations of fault slip rates [Molnar, 1979; McCaffrey, 1997]. Moreover, this observation is consistent with the nonlinear relation found by Bird et al. [2009] between earthquake production and relative plate velocity in subduction zones (slower subduction zones with subduction velocity ≤ 66 mm yr^{-1} are found to represent only 20% of earthquake productivity and 35% of the cumulative tectonic moment rate). Obviously, the experimental b-exponent is not related to the b-exponent of real seismicity because of the simplified (quasi two-dimensional) experimental setting which considers only a discrete variability of roughness heterogeneities [see Vargas et al., 2008 for quantitative details]. However, this additional observation strengthens the hypothesis that a common frictional root controls the physics of stable/unstable sliding.

Finally, the experimental results emphasize the nonlinearity of a-b (Figure 6b, d), which we ascribe to the competing role played by amplitude and spacing of protrusions, calibrating the magnitude of the slip event and the ease to transmit the triggered deformation, respectively. This

behavior may be applicable to other scales and tectonic settings, even if the physical environment of the subduction thrust fault is different from those of normal and transform faults [see Scholz, 1998 for a comprehensive review]. In particular, a similar mechanism may also be behind the occurrence of subduction mega-earthquakes. It is commonly accepted that mega-events cannot be produced by the rupture of an isolated asperity, as seismic moment is a function of the event rupture area [cf. e.g., Hanks and Kanamori, 1979]. Hence, the potential earthquake magnitude is a function of the maximum possible width and the maximum along-trench length of the rupture zone [Ruff, 1989; McCaffrey, 2007, 2008; Hayes and Conrad, 2007]. An analysis of the behavior of subduction interface seismogenic zones has recently recognized that the tectonic regime of the overriding plate (determined from the focal mechanisms of shallow earthquakes occurring at depths less than 40 km from the surface of the upper plate, far from the subduction interface) is likely to play a fundamental role in triggering mega-earthquakes [Heuret et al., 2011]. The statistical results presented in Heuret et al. (2011) show that 85% of the recorded M ≥ 8.5 events occurred in areas that are characterized by a neutral back-arc regime (i.e. no significant deformation or strike slip in the upper plate; sensu Lallemand et al. 2008; Wang, 2010b), challenging the common idea that mega-earthquakes are generally associated with compressive back-arc deformations [e.g. Uyeda and Kanamori 1979]. It has been thus proposed that the statistical association of mega-earthquakes with neutral subduction zones can be explained as being related to the most favorable interplay between a significantly large initial released seismic moment and a low critical stress for lateral rupture propagation [Hayes and Conrad, 2007; Rosenau and Oncken, 2010; Heuret et al., 2011].

In view of our experiments, we can suggest that a neutral tectonic regime in the overriding plate favors the accumulation of sediments along the subducting fault, which helps reducing the seafloor roughness, creating a smooth coupling capable to localize the deformation and rupture of a large area [Wang, 2010a, 2010b].
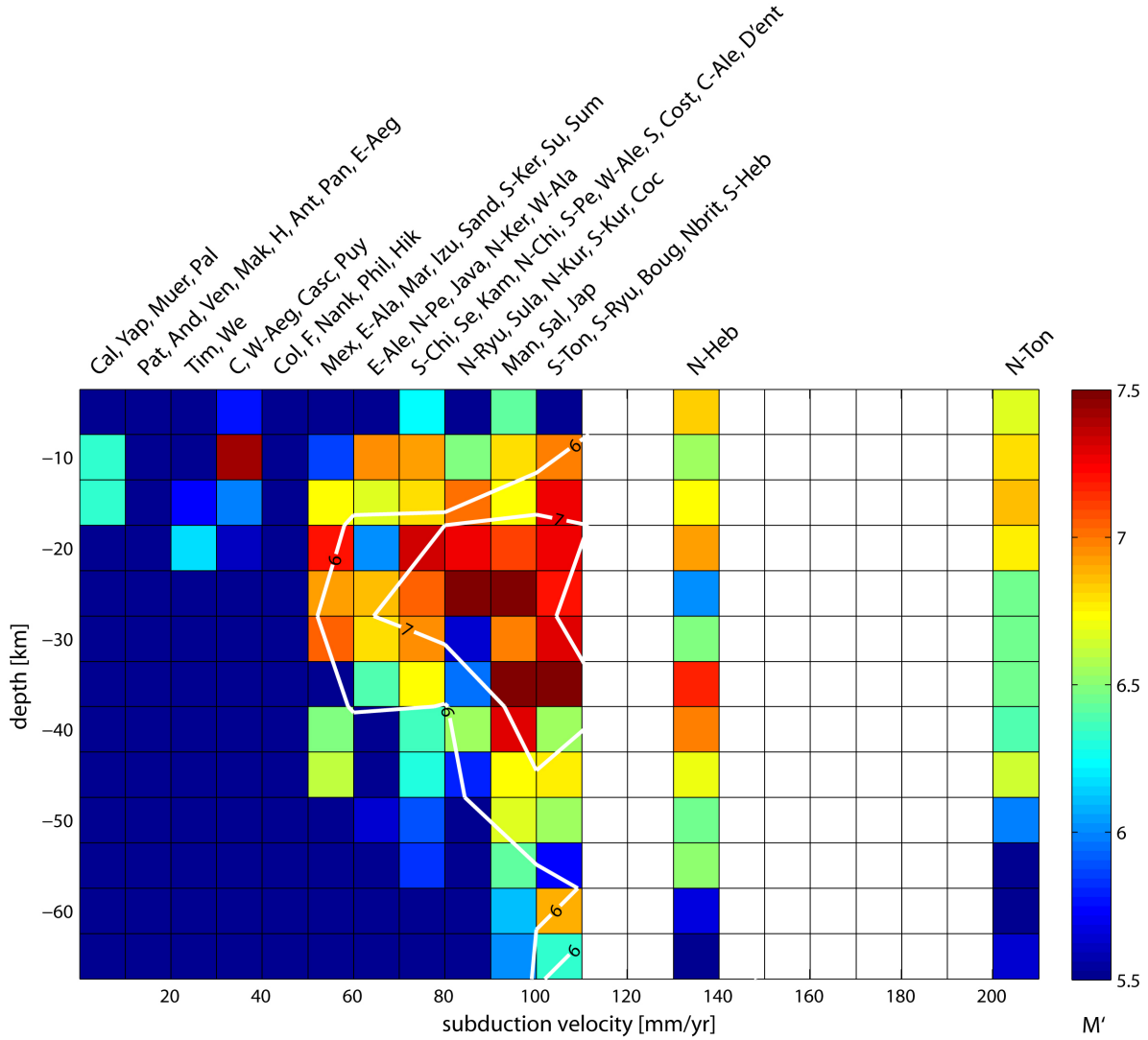
Figure 7: Figure 7: Magnitude *M'* obtained from cumulative moment [Kanamori, 1977] at a subduction fault as a function of subduction velocity and depth. Worldwide subduction zones are divided into 61 segments and M_w 5.5 - 7.5 events are extracted from CMT [Dziewonski et al., 1981] and EHB [Engdahl et al., 1998] global seismicity catalogs (1976-2007 time period; see Heuret et al., 2011 and Supplementary Material). $M_w > 7.5$ events are not sampled so that we explore a typical background seismicity of the subduction fault, characterized by trench-normal rupture propagations and relatively limited along-strike propagations. Seismic moments are grouped into 10 mm/yr subduction velocities vs 5 km depth cells. Isomagnitudes (grouped into 20 mm/yr subduction velocities vs 10 km depth cells) are shown by white lines. White cells denote lack of data. Subduction zones: Cal = Calabria; Yap = Yap; Pal = Palau; Pat = Patagonia; And = Andaman; Ven = Venezuela; Mak = Makran; H = Halmahera; Ant = Antilles; Pan = Panama; E-Aeg = Eastern Aegean; Tim = Timor; We = Wetar; C = Cotobato; W-Aeg = Western Aegean; Casc = Cascadia; Puy = Puysegur; Col = Colombia; F = Flores; Nank = Nankai; Phil = Philippines; Hik = Hikurangi; Mex = Mexico; E-Ala = Eastern Alaska;

119

Mar = Marianas; Izu = Izu-Bonin; Sand = Sandwich; S-Ker = Southern Kermadec; Su = Sulu; Sum = Sumatra; E-Ale = Eastern Aleutians; N-Pe = Northern Peru; Java = Java; N-Ker = Northern Kermadec; W-Ala = Western Alaska; S-Chi = Southern Chile; Se = Seram; Kam = Kamchatka; N-Chi = Northern Chile; S-Pe = Southern Peru; W-Ale = Western Aleutians; S = Sangihe; Cost = Costa-Rica; C-Ale = Central Aleutians; D'Ent = D'Entrcasteaux; N-Ryu = Northern Ryukyu; Sula = Sulawesi; N-Kur = Northern Kuriles; S-Kur = Southern Kuriles; Coc = Cocos; Man = Manila; Sal = Salomon; Jap = Japan; S-Ton = Southern Tonga; S-Ryu = Southern Ryukyu; Boug = Bougainville; Nbrit = New Britain; S-Heb = Southern New Hebrides; N-Heb = Northern New Hebrides; N-Ton = Northern Tonga.

5.5 Conclusions

We have used spring-block-like gelatin-sand paper models as analogs of the subduction thrust fault, and have analyzed the role played by sliding velocity (i.e. subduction rate), normal stress on the sliding surface (i.e. lithospheric pressure), and roughness of the interplate contact (i.e. "interplate protrusions") speculating about the slip behavior characterizing convergent margins. Our experimental results illustrate the usefulness of the conceptual seismological asperity model, and highlight the competing role played by size and distribution of protrusions in determining frictional contact properties.

Two important conclusions that can be drawn from our experiments are:

(1) If surface roughness is taken as the fixed variable of the system, changes from stick-slip to continuous sliding can be tuned by variations in the driving velocity and in the normal load;

(2) Interface geometrical irregularities control both the static friction and the rate friction parameter a-b, the latter showing negative values (i.e. seismic) only for a specific roughness amplitude and spacing values. This observation, in combination with an analysis of global seismicity, can be speculatively used to support a wear-controlled hypothesis for the downdip limit of the seismogenic zone.

5.6 Supplementary Material

5.6.1 Sampling methodology of the subduction seismogenic zone: assumptions and limitations

Three complementary global earthquakes catalogs were used to accurately describe the location, geometry and seismic activity of the subduction interplate seismogenic zone: the Harvard CMT catalog [Dziewonski and Woodhouse, 1981], the EHB catalog [Engdahl et al., 1998] and the Centennial catalog [Engdahl and Villasenor, 2002]. Thrust earthquakes were identified from the Harvard CMT catalog (see details below), which is the largest complete and uniform source of focal mechanism solutions and seismic moments available for $Mw \geq 5.5$ events. However, this catalog often suffers from non-negligible earthquake mislocations [i.e., Engdahl et al., 1998] and has limited time coverage (31 years in this study, from 1976 to 2007) with respect to large earthquake seismic cycles. To prevent potentially inaccurate seismogenic zone mapping due to CMT event mislocations, each identified plate interface thrust event was matched to the EHB catalog of relocated earthquakes, which is the most relevant global source for earthquake locations. Ideally, the time period used to study the seismic energy release along a given subduction thrust fault should be long enough to cover at least one seismic cycle of large earthquakes and preferably several to ensure reliable estimates. Because the average recurrence interval for large earthquakes along any particular plate boundary is on the order of several decades or centuries, at best only one seismic cycle (and often less) has been recorded during the years covered by the Harvard CMT catalog. To extend the time period of our study to the year 1900, we used the complete Centennial catalog [Engdahl and Villasenor, 2002], which is a self-consistent database of global seismicity spanning the 20th century, down to a magnitude of 7.0. As the Centennial catalog does not provide any information concerning the faulting mechanism of earthquakes, we assumed for the 1900-1975 period that any large-size earthquake ($Mw \geq 7.0$) located near or on the plate interface was a thrust event that occurred along the plate boundary. Because event locations are often poorly constrained,

the Centennial data were only used to assess the seismic energy released at the subduction seismogenic zone, and not used to map its extent.

For each subduction zone, a set of 2°-wide trench-normal transects were built, spaced by 1° intervals along the trench. Degrees are in latitude or in longitude, as a function of the trench azimuth. For each of the resulting 505 transects, the seismogenic zone of the subduction plate interface was mapped by analyzing the distribution of shallow (depth ≤ 70 km) and moderate- to large-size thrust earthquakes (Mw ≥ 5.5) from the Harvard CMT catalog, for which one nodal plane is consistent with the plate interface geometry and orientation. The plate interface earthquakes were identified in two steps. Firstly, only shallow thrust events were retained for each transect. The events were removed if one of the following conditions applied: negative slips (i.e., "normal faults"), both nodal planes with dip values ≥ 45° (i.e., "strike-slip" faulting), centroid depth > 70 km (i.e., "deep" events), centroid located more than 50 km seaward from the trench (subducting plate outer rise events) or backwards from the volcanic arc (i.e., backarc events). Then, for each selected thrust event, we checked to ensure that one of the focal mechanism nodal planes was consistent with the plate interface local geometry and orientation, requiring that the following conditions were verified [McCaffrey, 1994]: 1) one nodal plane was oriented toward the volcanic arc, 2) the strike azimuth of this nodal plane was between ± 45° with respect to that of the trench, and 3) the dip of this nodal plane was between ± 20° with respect to that of the slab. The EHB hypocenter catalog was then used to search for each plate interface event resulting from this selection, and the corresponding EHB location was associated with the CMT catalog earthquake parameters. The seismogenic zone sampling was then repeated for each transect, using the EHB improved locations associated with the CMT parameters. The tests were independently performed on both the original CMT data and the CMT + EHB data (with more reliable locations). The selection of events from the Centennial catalog included all the shallow (depth ≤ 70 km) and Mw ≥ 7.0 events for the 1900-1975 time period that were located between the volcanic arc and 50 km before the trench on the

subducting plate. All of these events were thought to occur along the plate interface, though this hypothesis cannot be tested for all events.

The 505 transects were then merged into 62 segments classified in terms of seismogenic zone characteristics. The criteria adopted to combine the original transects are: 1) the rupture area inferred for Mw $\geq$ 8.0 earthquakes must be included in a single segment; 2) transects with homogeneous activity on the seismogenic zone (largest magnitude, seismic rate) are grouped; 3) transects with homogeneous geometry of the seismogenic zone (dip, downdip length and downdip limit) are grouped.

Since the available database satisfies the Frohlich and Davies (1999) statistical requirements, thus confirming the good selection of interplate events (Heuret et al., 2011), our major uncertainty derives from the limited time interval of the seismic data. The time span is relatively short compared to the earthquake recurrence time observed along most subduction thrust faults [e.g., McCaffrey, 1997, 2008]. The short catalog time window effect is difficult to quantify, and it likely leads to incomplete pictures of the seismogenic zones, both in terms of the downdip extent and total seismicity. In this sense, our estimates must be considered as lower bounds.

Chapter 6

Gel-quakes: laboratory modeling of the subduction interplate seismic behavior

6.1 Introduction

The majority of global seismicity occurs at convergent margins either within each deforming plate (i.e. subducting and overriding) or along the plate interface [Scholz, 1990; Dixon and Moore, 2007, McCaffrey, 2007, 2008]. In particular, most of the large (Mw ≥ 7.0) and devastating (Mw ≥ 8.0) earthquakes are shallow depth events originating along the frictional interface between the subducting and the overriding plates [e.g. Scholz, 1990]. The seismic coupling along the subduction fault results from several factors; these include changes of the large-scale tectonic forces in the subduction zone, a decrease in slab dip resulting from changes in mantle flow, subducting plate and trench morphology, subducting sediments, the frictional properties of subducted material, and a variation in the coherency of slab produced by phase transformations and/or fluid pressure.

The understanding of the physics behind the behaviour of the interplate seismic events has not only scientific but also societal interest since their activity represents among Earth's most powerful and deadly natural hazards (e.g. the catastrophic event of Sumatra, December 2004).

Scientists have a general understanding of the process occurring along the subduction fault and recognized fundamental similarities between seismic cycles of different convergent margins. The basics of interplate seismicity can be described adopting the elastic rebound model, where the ongoing convergence of the subducting plate results in the elastic bending/buckling of the

continental crust and in the accumulation of elastic stress close to the locked part of the subduction fault. When the accumulated stress exceeds the sliding strength of the fault, an abrupt slip occurs and the stored elastic energy radiates as seismic waves. However, the interplate contact is seismogenic only in a specific interval (Scholz, 1998), which updated global analysis recently identified to arise between 11±4 km and 51 $\pm$ 9 km depths [Heuret et al., 2009] corresponding to a temperature range which is comprised between 100° - 150°C at the updip end and 350°- 450°C at the downdip end [Hyndman and Wang, 1993; Hyndman et al., 1995, 1997; Wang et al., 1995; Currie et al., 2002]. "Slow earthquakes" are often detected below this limit, testifying the lack of an abrupt transition between the end-member behaviors of stick-slip and steady creep [e.g. Schwartz and Rokosky, 2007; Gomberg et al., 2010]. To explain this peculiar behaviour, a more sophisticated rate- and state- dependent friction model is needed, including the dependency of μd and μs to the velocity and ageing, respectively [Dieterich, 1979; Ruina, 1983; see section 5.1 for additional details]. In this view, the system is described by an unstable region - failing with a velocity weakening behavior (i.e. once rupture initiates, slip accelerates because frictional strength decreases as slip velocity increases) - comprised by aseismic portions of the fault updip and downdip [e.g. Sholz, 1998; Marone and Saffer, 2003]. These two regions are considered to be velocity strengthening (i.e. frictional strength increases as slip velocity increases) and, therefore, unable to nucleate earthquakes. One peculiarity of subduction thrust fault consists in its length. Interplate earthquakes, in fact, have the opportunity to rupture hundreds of kilometers along trench resulting in megaevents if large asperities are present along the thrust plane [e.g. Plafker, 1972; Lay and Kanamori, 1981; Lay et al., 2005; Ammon et al., 2005; Stein and Okal, 2005; McCaffrey, 2008]. The seismic behavior of subduction thrust faults, in fact, has been successfully described by the "asperity model" [Lay and Kanamori, 1981; Lay et al., 1982]. In this view, seismic asperities are patches of the overall area of rupture showing large displacements, while barriers are areas inhibiting slip propagation [e.g. Lay and Kanamori, 1981; Lay et al., 1982, Seno, 2003]. As a

direct consequence, asperity size is very large where great earthquakes recur (e.g. Chile) and viceversa (e.g. Marianas).

Even if the overall behaviour of subduction faults seems satisfactory, many critical points remain obscure, mainly because of two reasons: a) most of what we know of the seismogenic zone has come from remote observables (i.e. land geodetic data, seismic reflection, exhumed subduction thrusts) providing only a "snapshot" of a long-term process; b) written and instrumental records of the past few centuries span too little time to provide enough perspective on great earthquake recurrence [e.g. Satake & Atwater, 2007; Mc Caffrey, 2008].

One of the most intriguing and unclear characteristics of the interplate thrust faults consists in the wide worldwide magnitude variability of current subduction zones. As we know, some subduction zones generated interplate events greater than Mw 9 (e.g. Chile, southern Alaska, Cascadia, northern Sumatra [Plafker, 1969, 1972; Abe and Kanamori, 1980], whereas others has been limited to Mw 7-7.5 (e.g. Izu-Bonin-Marianas subduction zones; Pacheco and Sykes, 1992; Pacheco et al., 1993). In general, continental subduction zones tend to have large maximum thrust earthquake magnitude [Hyndman, 2007].

The strain accumulation process in the post/inter-seismic period represents another stimulating, unexplained argument. The complex deformation pattern (e.g. coastal uplift) recorded within days or months after a great earthquake appears much faster than afterward [Thatcher and Rundle, 1984; Cohen and Freymueller, 2001], reflecting a strong time dependency of the system. This is due to post/inter-seismic transients, possibly related to the lithospheric viscoelastic rheology [Wang, 2007]. It is still poorly known if and how these transients can affect the tectonic and seismic evolution of subduction zones.

What is locking the subduction thrust and which is the reason of the strong variability in interplate locking? Some subduction thrust are inferred to be fully locked while other appear to be

only partially coupled [Hyndman and Wang, 1995; Hyndman et al., 1995; Brooks et al., 2003]. It is also possible that a single subduction zone shows both creeping and locking regions (e.g. Alaska – Aleutinan subduction zone; Freymueller et al., 2008). The simple and generally adopted "asperity model" can justify the variability of the subduction thrust fault behavior but there is still relatively little understanding of the way frictional motion varies with asperity size and distribution [e.g. Seno, 2003] and, in particular, there is still a great debate on the physical nature of asperities [see Bilek, 2005 for a comprehensive review]. Upper plate strength, frictional variation within the fault zone, and subducting plate features have all been considered valid ingredients. Recently, large asperities are associated with smooth interplate coupling producing large events [Wang, 2010], whereas rough interfaces, including seamounts or fracture zones where stress is concentrated, usually have relatively smaller/more frequent thrust earthquakes [e.g. Bilek et al., 2003]. In this framework, irregularities along the subduction thrust plane can result in seismic barriers [Kodaira et al., 2002; Wang, 2010]. Another very interesting and unsolved point is if these asperity pattern persists during different seismic cycles. It seems that in some cases asperities may be similar for repeating earthquakes, but it is not the rule for all the subduction zones [Mori, 2010].

One of the approach adopted to unravel the subduction thrust controlling factors consists in describing the seismic variability of interplate earthquakes in terms of parameters such as age of the subducting plate [Ruff and Kanamori, 1980; Peterson and Seno, 1984; Kanamori, 1986; Pacheco et al., 1993], convergence rate [Ruff and Kanamori, 1980; Peterson and Seno, 1984; Kanamori, 1986; Pacheco et al., 1993], upper plate kinematics [Uyeda and Kanamori, 1979; Peterson and Seno, 1984; Scholz and Campos, 1995], amount of subducted sediments [Ruff, 1989], thermal regime of the thrust zone [Shimamoto et al., 1993; Hyndman et al., 1997; Oleskevich et al., 1999], and combinations of these. Unfortunately, only weak correlations exist between previous parameters [Hayes & Conrad, 2007; Heuret et al., 2009, 2010], highlighting the possible leading role played by the subduction velocity in controlling the seismogenic zone geometry and energy release [Heuret et

al., 2010]. Moreover, it has been proposed that a large rupture (and, in turn, magnitude) should be promoted at the edge of neutral regime subductions [Heuret et al. 2010].

The persistence of many first-order ranking open points mirrors the complexities controlling the interplate seismicity of convergent margins. This pushed to study convergent margin dynamics using elastic and viscoelastic/elastoplastic analogue and numerical models [e.g Wang, 2007; Rosenau et al., 2009, 2010]. In particular, Rosenau et al., [2009] used an hybrid approach combining numerical elastic dislocation models to elastoplastic analogue models to obtain a residual plastic deformation signal and linking short- and long-term seismotectonic evolution of convergent margins. In these models, strain localizes at the rupture edges resulting in a segmented forearc which includes a stable shelf and coastal high overlying the seismogenic zone. Segmented wedges show a characteristic episodic slip behavior while deforming wedges (i.e. models that have not an updip limit of the seismogenic zone) follow a Gutemberg-Richter like distribution [Rosenau and Onken, 2009]. The potentiality to experimentally model interplate seismicity allowed also to translate the analog surface deformation associated with earthquakes to tsunami runup of the natural prototype [Rosenau et al., 2010].

Using three dimensional finite element models including viscoelastic mantle relaxation Wang and co-workers [2001] highlighted the strong time dependency of deformation rates during the seismic cycle. In particular it has been found that the deformation rate decreases through the interseismic period and that a seaward motion is predicted for inland sites early in the interseismic period due to effect of postseismic creep of the mantle.

In this Thesis I introduce a novel laboratory model of subduction which implements the analysis of earthquake cycles along the interplate thrust fault. The experimental setting includes tectonic loading, rate-dependent friction at the subducting-overriding plate interface and viscoelastic stress relaxation of the analog material. The model is able to generate deformation time series directly comparable to the prototype interplate earthquakes. The main advantage of using a

128

properly scaled viscoelastic material accounts, for the first time in analogue modeling, for the time dependence aspects of post/inter-seismic deformations [e.g. Rice 1993; Lapusta et al. 2000; Wang 2007], permitting to test this signal on recurrence time and on hypocenter distribution of events. In order to precisely detect the seismic signal, the model includes an accurate digital force gouge and up to date image analysis techniques (i.e. Feature Tracking and Photoelasticity). The goal of this study is to systematically test the influence of different factors in tuning the seismic behavior of subduction thrust faults: subduction velocity, dip of the subducting plate, depth and extent of the seismogenic zone, presence of topographical perturbation on the subducting plate. The characteristics of these models allow to detect the stress evolution during the full seismic cycle and the rupture dynamics. This approach, which includes a complex rheological response of the system, makes possible to test cause-effect relationships between governing parameters. Experimental results will be compared with the mode complete and updated available interplate earthquakes database [Heuret et al., 2010] aiming to close the gap between a natural too short time record and analogue long-term evolution.
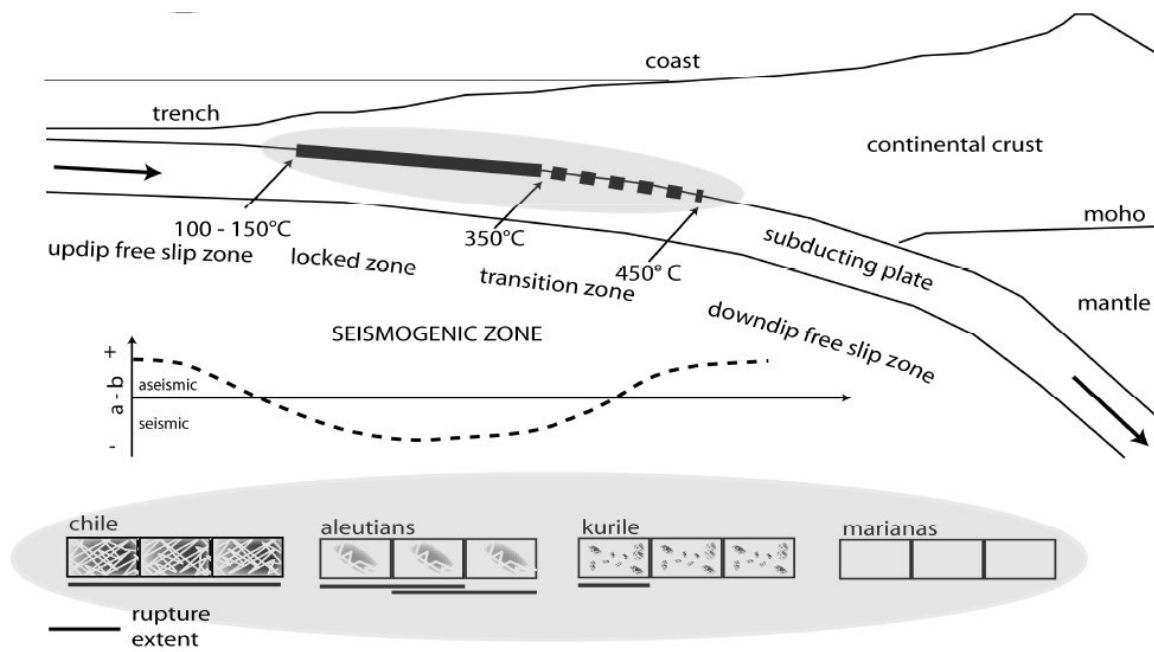
Figure 1: Schematic cross section of a convergent margin. In the upper panel, the seismogenic zone is highlighted by black bold line, moreover a friction rate parameter *a-b* model is proposed following Scholz [1998]. "Asperity model" [Lay et al., 1982] is illustrated in the grey-shaded area (bottom panel).

6.2 Laboratory approach

6.2.1 Experimental setup

The experimental setup used in this Thesis is a modification of the original viscous orogenic wedge apparatus built up by Rossetti and coworkers [2000]. The apparatus consists of a Perspex box 60 cm long, 40 cm high and 34 cm wide where a gelatin wedge (previously cooled at 10°C inside a wedge shaped module for 12 hours; see Chapter 4, supplementary material for gelatin preparation) is placed (Figure 2). An undeformable basal conveyer plate is driven by means of a screw jack connected to a computer controlled stepping motor. The dip of the basal plate can vary from 0° to 25°. A rigid vertical backstop is placed at the rear of the gelatin wedge.

According to scaling analysis (see Chapter 4 and 5), this subduction model is representative of about 380 km long section of forearc lithosphere. The megathrust reaches 64 km depth (for a dip of 10°) and its geometry is oversimplified using a planar surface. The seismogenic zone of the subduction thrust fault is realized using sandpaper (see details in Chapter 5) at the gelatin-plate interface. We consider a seismogenic zone characterized by stick-slip velocity weakening behaviour in a specific depth interval, updip and downdip limited by the material transition from sandpaper to stable sliding aluminium. Analogue earthquakes nucleate spontaneously within the seismogenic zone during loading and release part of the elastic strain energy stored in the system.
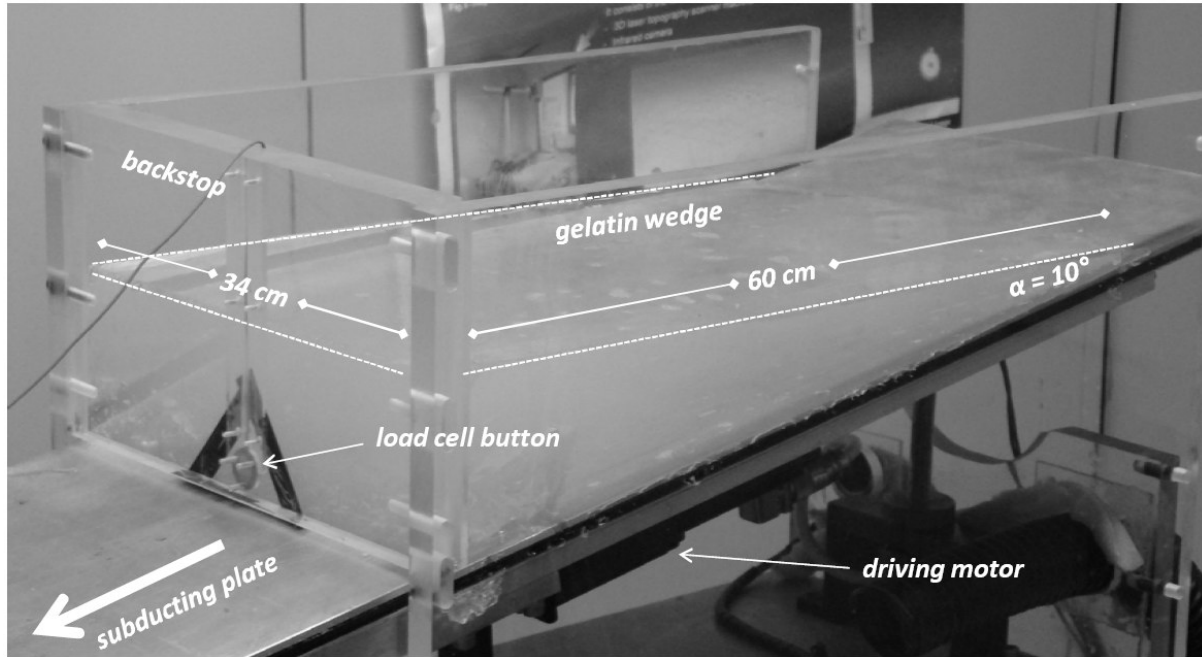
Figure 2: The experimental apparatus.

6.2.2 Material properties and scaling

The subduction interplate seismic model includes a preliminary extensive study of rheological and frictional properties of the analog materials.

A viscoelastic Pig Skin gelatin wedge is used as analogue of the lithosphere. The rheological properties of gelatin is characterized using a parallel plate rheometer (Anton Paar MCR 301) equipped with a Peltier element in order to control the temperature during the measurements. Pig Skin gelatin is selected from a wide range of gelatins. Thanks to an extensive study of rheological and physical properties of gelatins (see Chapter 4) it has been found that Pig Skin 2.5% wt at 10°C has the right properties to downscale for length, density, stress and viscosity upper crustal rock in the natural gravity field [DiGiuseppe et al., 2009]. In particular, the resulting nature/model scale factors are 6.4 x 10^5 for length (1 cm in the model corresponds to 6.4 km in nature), 1.7 x 10^6 for stress (1 Pa in the model corresponds to 1.7 MPa in nature) and 5.5 x 10^{-6} for velocities (1cm/min in the model corresponds to 2.9 cm/yr in nature; see Chapter 4 for a complete discussion on scaling). The main advantages of using gelatin can be schematically listed as: a) having viscoelastic

rheology to better reproduce the behavior of the natural prototype (including the time dependence of deformation); b) being transparent to track passive tracers included in the model and extrapolate its velocity field during the evolution of the model; c) being photoelastic to visualize its stress pattern when using a polariscope.

The seismogenic and aseismic zones of subduction thrust fault are modelled using sand-paper and aluminium, respectively. The frictional properties of the gelatin-sandpaper or gelatine-aluminium interfaces are investigated using a linear device similar to spring block model (see Chapter 5, for a complete description of the experimental apparatus used). The setup, allows to measure both the static friction coefficient μ_s and the friction rate parameter a-b thanks to a digital dynamometer (AFG-Mecmesin). Sand paper is selected among several materials tested (e.g. glass, plastic, aluminium, gelatin, rubber) because is surface is made of well sorted particles (silicon carbide) and allows a good calibration and reproducibility of the frictional properties. Chapter 5 includes an extensive quantification of roughness (expressed in terms of amplitude and wavelength) of nine sandpapers with different grit. The frictional properties of the gelatin-sandpaper is explored as a function of sliding velocity, normal pressure and roughness. In particular it has been found that: a) for most of the tested sandpapers the frictional behaviour is stick slip; b) the static friction coefficient is variable with values in the 0.2 - 1 range similarly to illite shale or quarz/smectite 50% mixture for normal pressure up to 150 MPa [Saffer and Marone 2003]; and that c) the friction rate parameter a-b is negative (seismic velocity-weakening behaviour), with values of the same order of magnitude of natural clay under condition representative of subduction thrust fault [e.g. Scholz, 1998; Saffer and Marone, 2003], for roughness amplitude which is scaling to nature from 25 to about 60 m. These results highlight the possibility to include a realistic stick-slipping velocity weakening zone in the subduction thrust fault.

The stable aseismic updip and downdip zones are modelled using aluminium. Frictional behavior of gelatin-aluminium interface is stable sliding (figure 3). Measurement of the frictional rate parameter a-b highlights a velocity strengthening behaviour (a-b ~ 0.01).

133
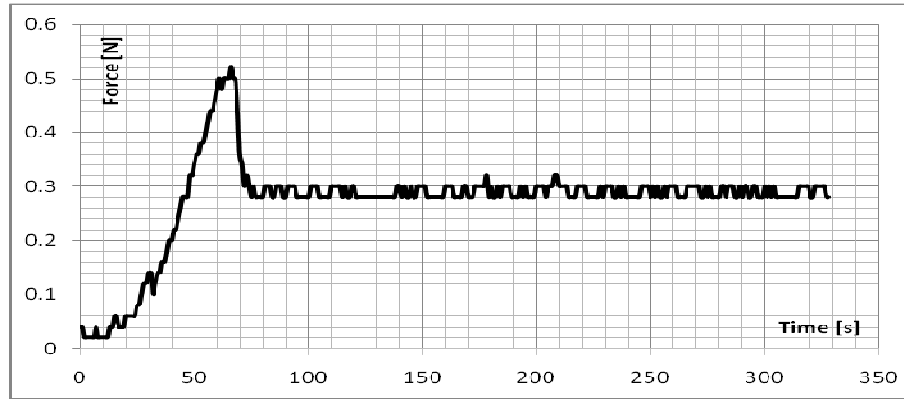
Figure 3: Force time series of sable sliding regime of a gelatin-aluminum interface (sliding velocity is 0.6 cm/min).

6.2.3 Experimental monitoring

Wedge models are monitored using a sequence of images taken in time intervals in the lateral and top view using two computer-controlled synchronized video cameras. The detection of gel-quakes is performed using a two-fold approach. Stress and deformations are inferred using the Feature tracking/Particle Imaging Velocimetry and the Photoelastic techniques (see details on image analysis techniques in Chapter 2). The formers allow to track and quantify also the velocity field of the model.

The Feature Tracking technique [Miozzi, 2004; Moroni and Cenedese, 2006; see Chapter 2 for details] is a robust tool used to monitor deformation and flow pattern in nature and analogue models [e.g. Funiciello et al., 2006; Guillaume et al., 2010]. It allows a Lagrangian description of the velocity field providing sparse velocity vectors with application points coincident with large luminosity intensity gradients (likely located along tracer particles boundaries). The system include a 60 cm long linear UV light in order to produce a planar uniform radiation focused onto a single cross section placed in the centerline of the model. The gelatin wedge is preliminary seeded with passive neutrally-buoyant tracers (50μm). The thickness of the light sheet focuses only 2 millimeters. Images of the bright reflecting particles used as passive tracer are recorded by the two cameras, set to acquire up to 30 frames a second. In our preliminary tests, top view images have

been analyzed using PIV, a basic cross correlation software accounting for optical deformation monitoring.

The Photoelastic technique (see details in Chapter 2 for the polariscope configuration and physical basics) is used complementary to Feature Tracking. Photoelastic technique is a robust stress analysis technique already used in analogue modeling of earthquake dynamics (e.g. Rubio and Galeano 1994; Lykotrafitis et al., 2006; Baumberger et al., 2008). Adopting the Photoelastic technique entail a twofold advantage: a) it allow to directly visualize the stress value at each point (integrated on a line which is perpendicular to the polarizer plane) in side view; and b) it allows to study the dynamics of rupture when combined with spatio-temporal evolution analysis [e.g. Rubio and Galeano, 1994; Baumberger et al., 2008]. In particular, this application could shed light on the mode stress is accumulated and released during seismic cycles at seismogenic depth.

In order to better control the results coming from these two image analysis techniques, and to have a direct measurement of force drop associated with analogue earthquakes, a digital force sensor is placed at the base of the backstop. The resolution of the force gauge is 0.02 N, well over the force drop associated with analogue earthquakes.

6.3 Preliminary results

In this paragraph preliminary modelling results are compared with general natural observation of the interplate thrust behavior. Subduction interplate model is preliminary tested using the easiest configuration consisting of a gelatin wedge overlying a 10° dipping, 0.6 cm/min fast, subducting plate. Wedge topography is oversimplified using a flat surface. In order to minimize deformation of the gelatin wedge during the model preparation, a plastic sheet, previously glued to the bottom of the shaping module, is used to remove the sample from the shaping module before placing it over the wedge machine. The plastic sheet includes a 20 cm wide adhesive sandpaper along the centerline of the model (i.e. from the base of the backstop to the trench). The result of this procedure is a "ideally undeformed" and completely coupled/locked gelatin wedge overlying a velocity-weakening zone as long as the base of the model. A total of 10 models have been performed to minimize initially induced deformation of the system. Monitoring of the models is performed both from top view (using the FT/PIV techniques) and from sideview (using the FT and the Photoelastic techniques). The experimental procedure forces to run three times the same model to obtain data analyzable with each technique.

At the beginning, the model starts to load elastically as plate convergence proceeds. Since the interplate contact is imposed to be fully coupled the interseismic phase begins. The top view image shows that interseismic deformation is dominated by a landward motion with faster velocities at the trench as respect to landward area. At the beginning of this stage, top view PIV vectors (which provide information comparable to those coming from GPS in nature) demonstrate that surface velocity is comparable with that of the subducting plate at the trench and progressively slows down going toward the backstop (Figure 4, panel a). Additional information is provided by sideview Feature Tracking analysis. A general landward motion is depicted together with an uplift component that gradually spreads from the backstop towards the trench (Figure 4, panel d). During this phase, the photoelastic technique shows a peculiar evolution: a series of photoelastic fringes

concave toward the backstop appear at the base of the backstop. During the evolving subduction process, the number of fringes increases testifying the stress building up (Figure 4, panel g). From top/side views the horizontal motion is close to be in critical deformation state after 9 minutes, and, simultaneously no more photoelastic fringes appear. The system at this point reaches a threshold and no more elastic deformation can be stored. Strating from this moment the rupture is ready to start. Rupture nucleates at the base of the backstop, where the majority of photoelastic fringes (i.e. stress) were concentrated, and progressively propagates updip enhanced by the diminished lithostatic pressure gradient [e.g. Das and Sholz, 1983]. Looking at the coseismic phase as depicted by the photoelastic technique, it seems that rupture speeds up while travelling towards the trench reflecting the velocity weakening frictional behavior of the plate interface (Figure 4, panel h). When the rupture starts to propagate updip there is few number of photoelastic fringes that are leading the rupture possibly highlighting a compressive stress associated to residual resistance to slip at the outer wedge [e.g. Wang and Hu, 2006]. At the back of the rupture tip, no more photoelastic fringes are observable testifying that the stress drop already occurred and the area is possibly under extension (Figure 4, panel h1). Information coming from side view Feature Traching and topview PIV are matching with the picture depicted by photoelasticity. It clearly appears that the coseismic stage is characterized by a seaward motion where most of the deformation occurs near the rupture area. Strong subsidence and limited uplift occur landward and close to the trench, respectively (Figure 4, panel b and e). Moreover, the top view of the coseismic phase shows that the fastest velocities are recorded near the rupture area and close to the trench, in agreement with the imposed velocity weakening frictional behavior of the gelatin-sandpaper contact (Figure 4, panel b). The rupture takes about a minute to reach the trench which is unrealistically too long if compared to the interseismic phase of the natural prototype. However, it is possible to calculate the timescale using a dimensionless number (Froude number) which relates gravitation and inertia forces. So, under the assumption that inertia may play no role during slow interseismic stage, it is justifiable to use an interseismic timescale separately with a factor more suitable for laboratory realization [e.g. Rosenau

et al., 2009]. The limitation of this procedure is that viscosity is not properly scaled for fast deformations (e.g. coseismic stage) where the main response is elastic [e.g. Wang, 2007].

Once the rupture reaches the trench, the postseismic phase initiates. The system reaches a relaxed state and the number of photoelastic fringes reduces to zero (Figure 4, panel i). However, a sideview Feature Tracking analysis highlights that small patches close to the backstop are still slowly moving toward the trench, possibly testifying a viscoelastic relaxation of the wedge (Figure 4, panel f). Topview image shows a stable picture where no significant horizontal motion is detected (Figure 4, panel c). The described fully coupled setup allows to model a single subduction interplate seismic cycle, in fact, any successive locking is observed.

In nature crustal deformation associated with rupture and locking of subduction thrust faults is mainly constrained by geodetic and geological observables. The basic idea is that stress and strain evolve in earthquake cycles and that the presently observed deformation provide just a snapshot of an evolving deformation field [Wang, 2007]. Combining information coming from multiple subduction zones that are presently at different phases of earthquake cycle allows to understand the full cycle. Figure 5 shows the main observables of the interplate earthquake cycle combining common features that are similar for the majority of subduction zones (i.e. schematic cross sections) including ideal natural cases.

GPS velocities demonstrate that the interseismic phase is characterized by a diffuse landward motion of the coastal regions reflecting the locked state of the subduction thrust fault [e.g. Dixon, 1993; Norabuena et al., 1998; Wang et al., 2003]. Plate locking can also promote subsidence of the area close to the trench, while a small uplift is depicted in the inland areas with amplitude decreasing with time after the earthquake.
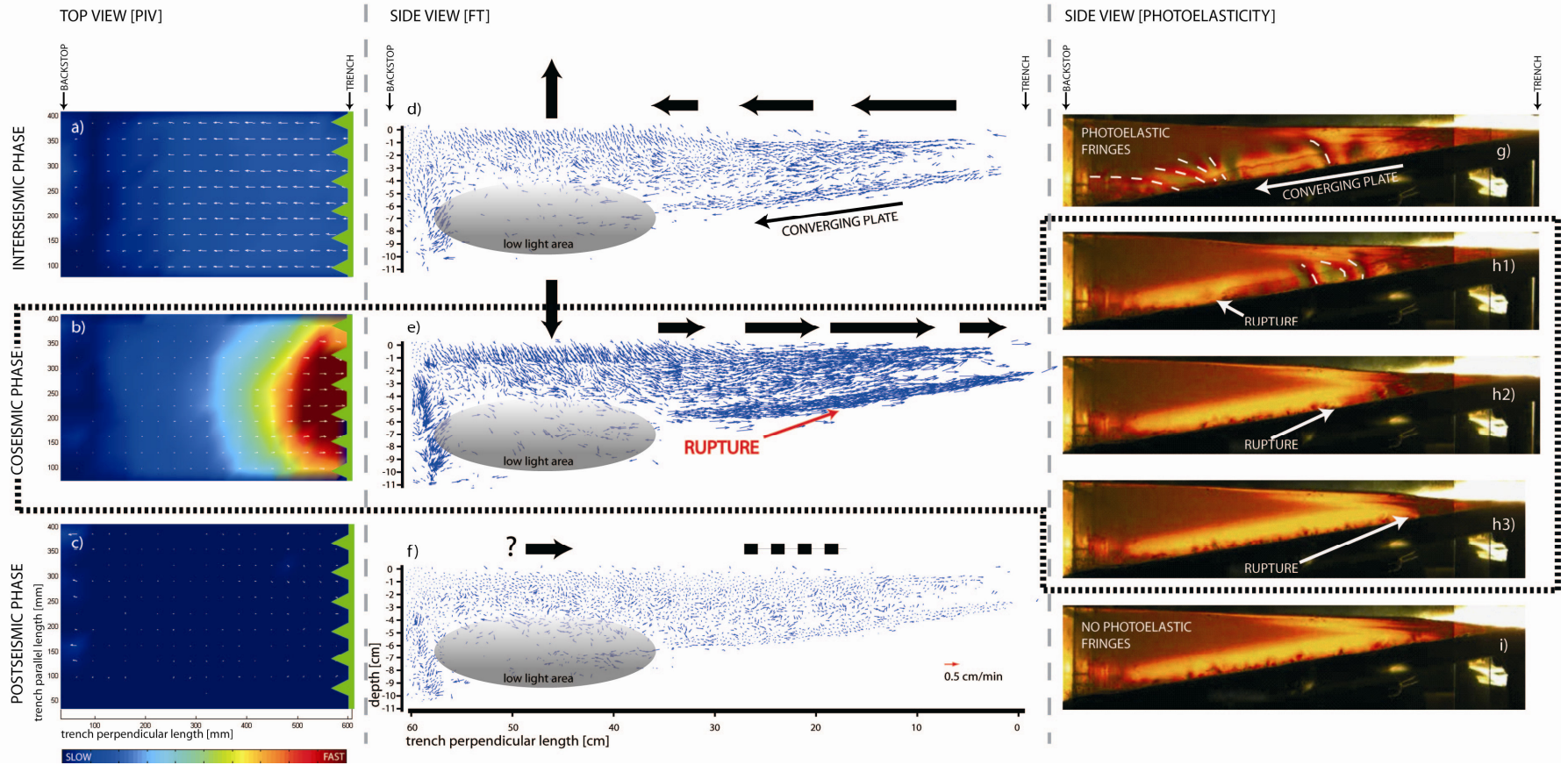
Figure 4: Summary of the preliminary experimental results. Each column represents top/side view and a different monitoring technique (specified in square brackets), while each line represent a different stage in the subduction interplate earthquake cycle. The length of white arrows in the first column are representative of velocity in a couple of subsequent photos while background color is representative of velocity magnitude normalized for all the experimental duration. The second column shows "raw" output of the Feature Tracking analysis (red reference vector is placed in the lowest panel). Overlying black arrows are used to summarize the main model features. The deepest part of the wedge is not sufficiently illuminated to track passive markers (gray shaded area). In the photoelastic analysis column, three pictures are used to depict the coseismic phase.

At the coseismic stage a characteristic reversal of the GPS velocities (i.e. toward the trench) is observed. Velocities are generally faster moving closer to the trench, highlighting that most of the deformation is localized near the rupture area. Maximum of subsidence is observed roughly above the downdip limit of the fault area while uplift occur in the area close to the trench [e.g. Plafker and Savage, 1970; Plafker, 1972; Atwater, 1987; Atwater and Hemphill-Haley, 1997].

Within days to months after the earthquake the deformation is much faster as respect to decades or centuries after [Burgmann et al., 2001; Melbourne et al., 2002; Yagi et al., 2003]. Postseismic deformation include two peculiar features of the seismic cycle: a) regions of maximum coseismic subsidence (e.g. coastal areas) bounce back becoming region of uplift [Thatcher, 1984; Plafker, 1971; Cohen and Freymueller, 2001]; and b) while coastal region moves landward (reflecting the onset of plates interface coupling), slow seaward motion of the backarc region is detected reflecting the viscoelastic relaxation of the system [e.g. Khazaradze and Klotz, 2003;

Wang, 2007].
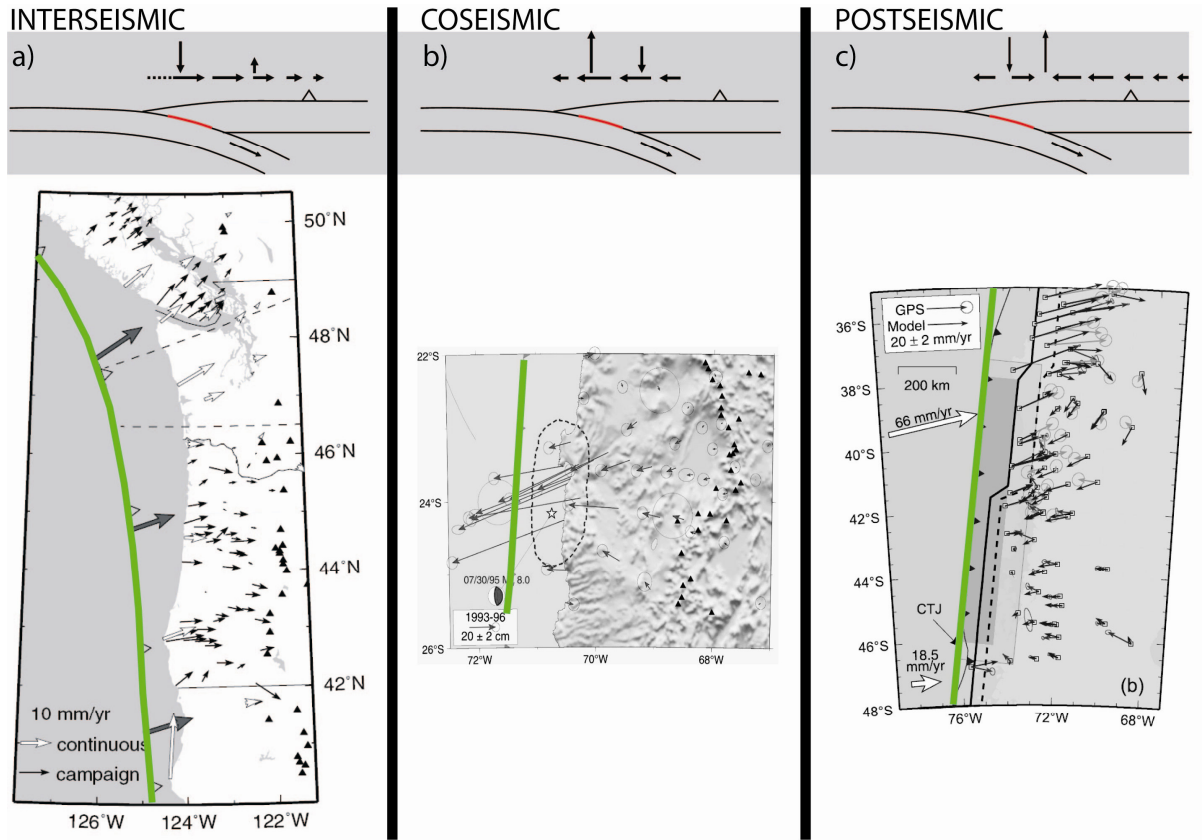
Figure 5: Summary of important features observed during subduction interplate earthquake cycle. Upper, grey-shaded panel shows schematic cross section of a convergent margin where the red line represents the seismogenic zone, black arrows represents simplified horizontal and vertical ground motion, green line is highlighting the trench (subduction thrust fault dipping toward East). Lower panel shows ideal natural cases. The three steps are representative of the main seismic cycle phases: a) during the interseismic phase (few decades to centuries after the earthquake) the plate interface is possibly locked and "corrected" GPS velocities (small black arrows) are directed away from the trench. An ideal picture representative of the elastic interseismic deformation of the Cascadia subduction zone is shown. Vectors offshore show the direction of Juan De Fuca plate motion relative to Cascadia forearc [from Wang et al., 2003]. b) at the coseismic phase, most of the deformation occurs near the rupture area. GPS velocities are directed- with magnitude increasing- toward the trench. The figure represents an ideal case of displacement dominated by coseismic phase (1995 Antofagasta earthquake, N. Chile Mw = 8.0 [from Klotz et al., 1999]); c) postseismic phase (days to few years after the earthquake) of the 1960 Chile rupture area where GPS measurements show landward motion of the coastal region (reflecting a new interseismic locking) and some inland areas still move slowly seaward few years after the event [GPS velocities and model from Klotz et al. 2001 Wang et al., 2007, respectively].

Our preliminary analogue models of subduction interplate behaviour mimic the major features of the seismic cycle if compared with ideal natural cases [e.g. reversal of horizontal velocities or subsidence associated with the coseismic stage]. However, there are some small

differences mainly in the vertical deformation. In particular, using the fully locked configuration either evident uplift of the coastal area is not observed, or it is not possible to identify precisely a region of maximum coseismic subsidence. Moreover, differently from natural cases, the model is not showing a significant postseismic coastal uplift. Both features can found an explanation in lacking of a localized deformation in a precise area along the thrust fault [e.g. an updip and downdip confined seismogenic zone].

Currently, the modelling technique is improved adopting an undeformable device (e.g. a 40 cm wide 60 cm long aluminum plate including a cutting edge) which is used to remove the gelatin wedge from the shaping module and to locate it over the apparatus, minimizing initial artificial deformations. Moreover, the analogue subducting plate is including an updip and downdip confined velocity weakening seismogenic zone. Using this configuration the gelatin wedge is behaving in a more realistic way as respect to the "fully coupled" setting. A preliminary test is performed using the same geometrical and kinematical conditions and visualization techniques. This more sophisticate configuration allows to recognize a sequence of seismic cycles. In particular, we found that the model experienced 30 earthquakes during a 13 minutes long run. As in the previous set of models the gelatin wedge require a couple of minutes to organize itself inside the apparatus than it starts to cyclically tectonically loading and slipping. The recurrence time is about 30 seconds and the coseismic time duration is about 1 second.

The goal of future work will be to continue improving the latter configuration (overcoming last technical difficulties) and start to systematically test governing parameters (e.g. subduction velocity, dip of the subducting plate, seafloor roughness) controlling the subduction thrust behavior, searching for possible cause-effect relationship (see also paragraph 7.4).

Chapter 7

Conclusions

New insights on the complex processes of interacting plate at subduction zones have been proposed on the base of a multidisciplinary approach combining analogue modeling, rheometry and worldwide statistics of subduction interplate earthquakes. In the following the basic findings are summarized and open issues highlighted, suggesting rooms for possible future directions.

7.1 Long-term role of mechanical coupling in convergent margins

The 3-D experimental models of subduction described in Chapter 3 have been designed to investigate the role of lateral mechanical coupling variation in shaping convergent margins. To test this hypothesis, two end member models have been used, characterized by a variable distribution of coupling at the plate interface : a) uniform low coupling; b) central portion of the margin strongly coupled and lateral limbs lubricated. The dynamic resisting contribution of the subduction thrust fault as respect to driving forces varies from 5% to ~37% in the former and latter setup, respectively. An homogeneously low mechanical coupling between the subducting and overriding plates produces a slightly upper plate shortening (less than 60 km in nature) while most of the driving velocity is transferred into trench advancement . As consequence, the resulting trench shape preserves its initial straight shape.

The variably distributed degree of mechanical coupling at the plate interface causes a maximum upper plate shortening of about 4 cm (about 240 km in nature) in the highly coupled center of the system, accompanied by a 1.5 – 2 mm high plate bulging (equivalent to 8-12 km in nature). At the slightly coupled wings of the system, the overriding plate experiences only 2.5 cm

of shortning, which is equivalent to about 180 km in nature. The lateral variations in shortening determine the convergent margin to assume a pronounced curvature, concave to the subducting plate).

Under the assumption of a simplified purely viscous deformation and considering that erosive processes are not implemented in this type of models, experimental results with variable distribution of coupling at the plate interface have been speculatively compared to the Andean case. Experimental shortening values compare well to field estimates along the Andean belt. In fact, it has been estimated that ~300 km of shortening are required to account for the topographic volume of the central Andes, but only ~150 km are needed in the northern and southern limbs [Klay & Monaldi, 1998; Hindle et al., 2005]. Lateral shortening gradients produced a pronounced curvature of the margin which is matching with the Andean case. Moreover, the topographic uplift obtained in the models falls within an acceptable range for the high Andean plateau.

Even if other parameters (i.e. subducting plate in terms of width, age and laterally buoyancy/strength variations) may play a role influencing the evolution of Andean margin [e.g. Schellart et al., 2007; Molnar & Atwater, 1978; Gorbatov & Kennett, 2003; Capitanio et al., submitted] in this Thesis it has been demonstrated that the peculiar shape of the Andean margin (including shortening and topography of the upper plate) can be reconciled also if the central portion of the margin is more strongly coupled than the northern and southern limbs.

7.2 Role of interplate roughness on seismic behavior of convergent margins

A first-order importance in controlling the seismogenic potential of subduction megathrust lies in geometrical protrusion of plates interface. The role of protrusions along plate interface in controlling the slip propagation is debated. It was alternatively proposed that they act as asperities [i.e. enhancing the seismic rupture, e.g. Cloos, 1992] or as barriers [i.e. blocking the seismic rupture e.g. Wang, 2010].

Spring-block models have been realized to investigate the effect of small scale roughness (meters to hundred of meters in amplitude and wavelength) on frictional behavior of a gelatin (analogue of the Earth's crust/lithosphere)-sandpaper (analogue of the rough interface) system. These models have the advantage to use tribological properties which take into account the visco-elastic response of the gelatin layer. Models demonstrated that the static friction is a steeply decreasing as a function of the ratio between protrusions separation and amplitude. The velocity strengthening/weakening parameter (*a-b*) in the state- and rate-dependent dynamic friction law becomes negative (i.e. seismic) for intermediate values of asperity amplitude (scaling to 25 - 60 meters in nature). On the contrary, very large (i.e. hundreds of meters) or very small (i.e. meters or less) geometric protrusions show a velocity strengthening behavior and act as barriers inhibiting slip propagation. Comparing laboratory results to natural data of subduction interplate events, it has been pointed out that if the roughness profile of the subduction fault is an ingredient for interplate seismic events, its properties must change with depth to justify the observations of aseismic updip and downdip margins of the seismogenic zone. A qualitative model reconciling the downdip seismic variability of subduction thrust faults would consist of: a) a rough megathrust at shallow depths, unable to produce significant seismicity because of low lithospheric pressure [e.g. Das and Scholz, 1983]; b) a moderately rough, velocity-weakening fault at intermediate depths, able to produce earthquakes whose magnitude is calibrated by the interplay between protrusion amplitude and wavelength, normal load, and subduction velocity; c) a smooth, velocity-strengthening fault at

larger depth, showing transitional behavior from shallower stick-slip to deeper stable sliding. These results confirm the important role of roughness as a key ingredient controlling seismic behavior of a given subduction zone.

7.3 Role of subduction velocity on seismic behavior of convergent margins

The subduction velocity is one of the first-order controlling parameter of plate interfaces physical characteristics influencing both the geometry and the seismic behavior of convergent margins. As a rule of thumb, fast subducting plates are associated with large seismic rates [Heuret et al., in press]. In particular, there has been much discussion about the possible linkages between maximum sizes of subduction interplate earthquakes and subduction velocity.

Advanced spring-block models (including a properly scaled viscoelastic rheology of the lithosphere) have been used to investigate the role of sliding velocity (i.e. subduction rate) on the interface seismic behavior. Experimental results demonstrated that the system encounters a bifurcation at around 1 cm/min: stable sliding (i.e. aseismic creep) predominates at higher velocities and stick-slip (i.e. seismic) predominates at lower velocities. Time intervals between slip episodes increase with decreasing velocity. On the contrary, increasing sliding velocity increases the frequency of slip episodes, but in the limit it tends to stable sliding after a single shear force drop. Those results have been fruitfully compared to worldwide statistics of interplate seismicity [Heuret et al., in press]. This procedure allowed to highlight the complex role played by subduction velocity in tuning seismic interplate behavior, explaining why fastest subduction zones (i.e. Tonga, New Hebrides) are not associated with a predictable powerful activity [Pacheco and Sykes, 1992; Pacheco et al., 1993; Gutscher and Westbrook, 2009; Heuret et al., in press]. A lack of correspondence between natural and experimental frictional behavior has been found for the slowest subduction where possibly the natural prototypes have not experienced a complete seismic cycle, yet [>100 Myr long, Gutscher & Westbrook, 2009].

7.4 Suggestion for future work

While the present study shed light on most of the questions addressed in the introduction, it also opens new avenues for future investigation. Present limitations of analogue models of subduction at the mantle scale have to be seen as potential avenues of future development. A realistic model of subduction should enter in a more global view, considering thermal aspects and including the contribution of mantle convection. Mantle convection and plate tectonics are, for simplicity, too often studied as independent systems, while it is not the case in the Earth prototype. In the future, the gap between large scale and small scale observations must be filled, having the possibility to simulate complex 3D scenarios to study the mechanisms producing a convection with a self-sustained plate tectonics (i.e. plate circuit). This work should be principally directed towards the selection of new analogue materials with a temperature-dependent rheological behavior able to simulate 1) the Earth's stratification; 2) both deep mantle convection and surface plate dynamics.
 Hence, combining material science to analogue modeling should represent a promising area for future work.

- It has been already demonstrated the strong potentiality of modelling interplate subduction earthquakes for civil purposes [e.g. relationship with tsunamis runup; Rosenau et al., 2010]. Future strategy plans to complete the set of gelatin wedge models and validate analogue results with numerical simulation (work in progress in collaboration with Y. van Dinther, ETH Zurich, Switzerland) and with geodynamic observables from Heuret et al., [in press] database. This ambitious plan should permit to characterize subduction zone seismicity and long-term hazard. The general assessment could be tested adapting subduction features (i.e. subduction velocity, dip, interplate roughness) to end member natural cases (i.e. low seismogenic potential: Tonga; high seismogenic potential: Chile).

- It should be possible to export the well constrained rheological and frictional properties of gelatins to develop crustal/lithospheric models to the study of other tectonic scenarios (i.e.

148

strike-slip or normal faults). These models can take the advantage of introducing a proper visco-elatic relaxation for post-seismic deformations and, in turn, to better constrain the long-term seismic behaviour. In particular, developed image analysis solutions (i.e. photoelastic technique) allows to easily compare model results to natural observables (i.e. interferometric images). An intriguing natural application could be unraveling the westward unzipping of the North Anatolian Fault.

References

Chapter 1

Aki, K., Asperities, barriers, characteristic earthquakes and strong motion prediction, *Journal of Geophysical Research*, 89, 5867-5872, 1984.

Allmendinger, R.W., Smalley, R. Jr, Bevis, M., Caprio, H., and Brooks, B., Bending the Bolivian orocline in real time: *Geology*, v. 33, p. 905-908, 2005.

Bilek, S. L., Influence of subducting topography on earthquake rupture, in *The seismogenic zone of subduction thrust fault*, edited by T. Dixon and C. Moore, pp. 123-146, Columbia University Press, New York 2005.

Bird, P., Y. Y. Kagan, D. D. Jackson, F. P. Schoenberg and M. J. Werner, Linear and Nonlinear Relations between Relative Plate Velocity and Seismicity, *Bull. Seismol. Soc. Am.*, 99(6), 3097-3113, doi:10.1785/0120090082, 2009.

Brace, W. F. and D. L. Kohlsted, Limits on lithospheric stress imposed by laboratory experiments, *Journal of Geophysical Research*, 85, 6248-6252. 1980.

Burridge, R. and L. Knopoff, Model and theoretical seismicity, *Bull. Seismol. Soc. Am.*, 57, 341-371, 1967.

Capitanio, F.A., Stegman, D.R., Moresi, L.N. and Sharples, W., Upper plate controls on deep subduction, trench migrations and deformations at convergent margins, *Tectonophysics*, doi:10.1016/j.tecto.2009.08.020, 2010.

Currie, C. A., R. D. Hyndman, K. Wang and V. Kostoglodov Thermal models of the Mexico subduction zone: Implications for the megathrust seismogenic zone, *Journal of Geophysical Research [Solid Earth]*, 107(B12), 2370, doi:10.1029/2001jb000886, 2002.

Di Giuseppe, E., F. Funiciello, F. Corbi, G. Ranalli and G. Mojoli, Gelatins as rock analogs: A systematic study of their rheological and physical properties, *Tectonophysics*, 473(3-4), 391-403, doi:10.1016/j.tecto.2009.03.012, 2009.

Ericksson, S.G., and Arkani-Hamed, J., Subduction initiation at passive margins: The Scotian Basin, Eastern Canada as a potential example, *Tectonics*, *12*, 678-687, 1993.

Espurt, N., Funiciello, F., Martinod, J., Guillaume, B., Regard, V., Faccenna, C., Brusset, S., Flat subduction dynamics and deformation of the South American plate: Insights from analog modeling. *Tectonics* 27. doi:10.1029/2007TC002175, 2008.

Funiciello, F., Faccenna, C., Giardini, D., and Regenauer-Lieb, K., Dynamics of retreating slabs: 2. Insights from three-dimensional laboratory experiments, *Journal of Geophysical Research*, 108, B4, 2207, doi:10.1029/2001JB000896, 2003.

Funiciello F., M. Moroni, C. Piromallo, C. Faccenna, A. Cenedese, and H. A. Bui, Mapping mantle flow during retreating subduction: Laboratory models analyzed by feature tracking, *J. Geophys. Res*, 111, B03402, doi:10.1029/2005JB003792, 2006.

Gorbatov, A., and Kennett, B.L.N., Jount bulk-sound and shear tomography for Western Pacific subduction zones, *Earth and Planetary Science Letters*, v. 210, 527-543, 2003.

Guillaume B., J. Martinod and N. Espurt, Variations of slab dip and overriding plate tectonics during subduction: insights from analogue modelling Tectonophysics 463, 167–174, 2009.

Heuret, A., S. Lallemand, C. Piromallo and F. Funiciello, Physical properties of subduction type seismogenic zones revisited, *Eos Trans*. AGU, San Francisco, 2009.

Heuret, A., S. Lallemand, F. Funiciello, C. Piromallo, and C. Faccenna, Physical properties of subduction-type seismogenic zones revisited, *Geochem. Geophys. Geosyst., i*n press.

Hyndman, R. D., M. Yamano and D. A. Oleskevich, The seismogenic zone of subduction thrust faults, *Isl. Arc*, 6(3), 244-260, 1997.

Hyndman, R. D. and K. Wang, Thermal Constraints on the Zone of Major Thrust Earthquake Failure - the Cascadia Subduction Zone, *Journal of Geophysical Research [Solid Earth]*, 98(B2), 2039-2060, 1993.

Isacks, B.L., Uplift of the central Andean plateau and bending of the Bolivian orocline, *Journal of Geophysical Research*, 93, 3211-3231, 1988.

Lay, T., H. Kanamori and L. Ruff, The asperity model and the nature of large subduction zone earthquakes, *Earthquake Pred. Res.*, 1, 3-71, 1982.

Maffione, M. Speranza, F., and Faccenna, C., Bending of the Bolivian orocline and growth of the central Andean plateau: Paleomagnetic and structural constraints from the Eastern Cordillera (22-24 degrees S, NW, Argentina): *Tectonics*, 28, 2009.

Marone, C. and D. M. Saffer, Fault friction and the upper transition from seismic to aseismic faulting, in *The seismogenic zone of subduction thrust fault*, edited by T. Dixon and C. Moore, 346-369, Columbia University Press, New York, 2005.

Marques, F.O., and Cobbold, P.R., Effects of topography on the curvature of fold-and-thrust belts during shortening of a 2-layer model of continent lithosphere, *Tectonophysics*, 415, 65-80, 2006.

Mart, Y., Aharonov, E., G., Mulugeta, W., Ryan, T., Tentler, and L., Goren, Analogue modelling of the initiation of subduction, *Geophysical Journal International*, 160, 1081-1091, 2005.

McKenzie, D.P., The initiation of trenches: A finite amplitude instability, in *Island Arcs Deep Sea Trenches and Back-Arc Basins*, edited by M. Talwani, and W.C. Pitman, pp. 57-61, Maurice Ewing Ser. Vol. 1, 1977.

Molnar, P., and Atwater, T., Interarc spreading and cordilleran tectonics as alternates related to the age of subducted oceanic lithosphere, *Earth and Planetary Science Letters*, 41, 330-340, 1978.

Mueller, S., and Phillips R., On the initiation of subduction, *Journal of Geophysical Research*, *96*, 651-665, 1991.

Peacock, S. M. and R. D. Hyndman, Hydrous minerals in the mantle wedge and the maximum depth of subduction thrust earthquakes, *Geophysical Research Letters*, 26(16), 2517-2520, 1999.

Pytte, A. and R. C. Reynolds, The thermal transformation of smectite to illite, in *Thermal Histories of Sedimentary Basins*, edited by T. H. McCulloh and N. D. Naeser, 133-140, 547 Springer, New York, 1988.

Saffer, D. M. and C. Marone, Comparison of smectite- and illite-rich gouge frictional properties: application to the updip limit of the seismogenic zone along subduction megathrusts, *Earth Planetary Science Letters*, 215(1-2), 219-235, doi:10.1016/S0012-821X(03)00424-2, 2003.

Schellart, W.P., Freeman, J., Stegman, D.R., Moresi, L., and May, D., Evolution and diversity of subduction zones controlled by slab width, *Nature*, 446, 308-311, 2007.

Scholz, C. H., Earthquakes and friction laws, *Nature*, 391, 37-42, 1998.

Voisin, C., J. R. Grasso, E. Larose and F. Renard, Evolution of seismic signals and slip patterns along subduction zones: Insights from a friction lab scale experiment, *Geophysical Research Letters*, 35(8), L08302, doi:10.1029/2008GL033356, 2008.

Wang, K., Coupling of tectonic loading and earthquake fault slips at subduction zones, *Pure Appl. Geophys.*, 145(3/4), 537-559. 1995.

Weijermars, R. and H. Schmeling, Scaling of newtonian and non newtonian fluid dynamics without inertia for qantitative modelling of rock flow due to gravity (including the concept of rheological similarity), *Physics of the Earth and Planetary Interiors*, *43*, 316-330, 1986.

Chapter 2

Acocella, V., Faccenna, C., Funiciello, R., Rossetti, F., Analogue modelling of extensional transfer zones. *Bollettino Societa' Geologica Italiana* 119, 85–96, 2000.

Aki, K., Asperities, barriers, characteristic earthquakes and strong motion prediction, *J. Geophys. Res.*, 89, 5867-5872, 1984.

Basile, C., Brun, J.P., Transtensional faulting patterns ranging from pull-apart basins to transform continental margins, an experimental investigation. *J. Struct. Geol.*, 21, 23–37, 1998.

Baumberger, T., F. Heslot, and B. Perrin, Crossover from creep to inertial motion in friction dynamics, *Nature*, 367, 544–546, doi:10.1038/367544a0, 1994.

Baumberger, T., C. Caroli and O. Ronsin, Self-healing slip pulses and the friction of gelatin gels, *Eur. Phys. J. E: Soft Matter Biol. Phys.*, 11(1), 85-93, doi:10.1140/epje/i2003-10009-7, 2003.

Becker, T., C. Faccenna, D. Giardini, and R. O'Connell, The development of slabs in the upper mantle: Insights from numerical and laboratory experiments, *J. Geophys. Res.,* 104, 15,207– 15,226, 1999.

Bellahsen, N., Faccenna, C., Funiciello, F., Dynamics of subduction and plate motion in laboratory experiments: Insights into the "plate tectonics" behavior of the Earth. *J. Geophys. Res,* 110. doi:10.1029/2004JB002999, 2005.

Bijwaard, H., W. Spakman, E.R. Engdahl. Closing the gap between regional and global travel time tomography. *J. Geophys. Res.*, 103 (B12), 30,055 - 30,078, 1998.

Bonini, M., Souriot, T., Boccaletti, M., Brun, J.P., Successive orthogonal and oblique extension episodes in a rift zone, laboratory experiments with application to the Ethiopian Rift. *Tectonics* 16, 347–362, 1997.

Boutelier, D., C. Schrank, and A. Cruden, Power-law viscous materials for analogue experiments: New data on the rheology of highly-filled silicone polymers, *J. Struct. Geol.*, 30,341–353, doi:10.1016/j.jsg.2007.10.009, 2008.

Boutelier, D. A. and A. Cruden, Impact of regional mantle flow on subducting plate geometry and interplate stress: insights from physical modelling, *Geophys. J. Int.,* 174, 719–732, doi:10.1111/j.1365-246X.2008.03826.x, 2008.

Brace, W. F. and D. L. Kohlsted, Limits on lithospheric stress imposed by laboratory experiments, *Journal of Geophysical Research*, 85, 6248-6252. 1980.

Brun, J.P., Sokoutis, D., van den Driessche, J., Analogue modeling of detachment fault systems and core complexes. *Geology* 22, 319–322, 1994.

Brune, J. N., Particle motion in a physical model of shallow angle thrust faulting, Proc. Indian Acad. Sci., 105(2), 197–206, 1996.

Buckingham, E.: On physically similar systems; Illustrations of the use of dimensional equations, *Phys. Rev*., 4, 345–376, 1914.

Burridge, R. and L. Knopoff, Model and theoretical seismicity, *Bull. Seismol. Soc. Am*., 57, 341-371, 1967.

Buttles, J., and P. Olson, A laboratory model of subduction zone anisotropy, *Earth Planet. Sci. Lett.*, 164, 245– 262, 1998.

Corti G., Bonini M., Conticelli S., Innocenti F., Manetti P., Sokoutis D., Analogue modelling of continental extension: a review focused on the relations between the patterns of deformation and the presence of magma. Earth-Science Reviews, 63, 169-247, 2003.

Davy, P., Cobbold, P.R., Indentation tectonics in nature and experiment. 1. Experiments scaled for gravity. *Bulletin of the Geological Institute of Uppsala*, New Series 14, 129–141, 1988.

Davy, P., and P.R. Cobbold, Experiments on shortening of a 4-layer continental Lithosphere, *Tectonophysics*, 188, 1-25, 1991.

Dixon, J.M. &Liu, S. Centrifuge modelling of the propagation of thrust faults. In:Thrust Tectonics (Ed. by K.McClay), pp. 53-69. Chapman &Hall, London, 1992.

Eberle, M.A., Grasset, O., and Sotin, C., A numerical study of the interaction between the mantle wedge, subducting slab and over-riding plate: *Physics of the Earth and Planetary Interiors*, v. 134, p. 191–202, 2002.

Faccenna, C., P. Davy, J.P. Brun, R. Funiciello, D. Giardini, M. Mattei, and T. Nalpas, The dynamic of backarc basins: an experimental approach to the opening of the Tyrrhenian Sea, *Geophysical Journal International*, *126*, 781-795, 1996.

Faccenna, C., D. Giardini, P. Davy, and A. Argentieri, Initiation of subduction at Atlantic-type margins: Insights from laboratory experiments, *Journal of Geophysical Research*, *104* (B2), 2749-2766, 1999.

Fukao, Y., Obayashi, M., Inoue, H., and Nenbai, M., Subducting slabs stagnant in the mantle transition zone. *J. Geophys. Res*., 97, 4809-4822, 1992.

Funiciello, F., C. Faccenna, D. Giardini, and K. Regenauer-Lieb, Dynamics of retreating slabs (part 2): Insights from 3-D laboratory experiments, *J. Geophys. Res.*, 2003.

Funiciello, F., Faccenna, C., Giardini, D., Role of lateral mantle flow in the evolution of subduction system: insights from 3-D laboratory experiments. *Geophys. J. Int.* 157, 1393–1406, 2004.

Funiciello, F., Moroni, M., Piromallo, C., Faccenna, C., Cenedese, A., Bui, H.A., Mapping the flow during retreating subduction: laboratory models analyzed by feature tracking. *J. Geophys. Res*. 111, B03402 03410.01029/02005JB003792, 2006.

Funiciello F., Faccenna C., Heuret A., Lallemand S., Di Giuseppe E., Becker, T.W. Trench migration, net rotation and slab - mantle coupling, *Earth and Planetary Science Letters*, 271 233–240. 2008.

Griffiths, R. W., R. I. Hackney, and R. D. van der Hilst, A laboratory investigation of effects of trench migration on the descent of subducted slabs, *Earth Planet. Sci. Lett*., 133, 1 – 17, 1995.

Guillou-Frottier, L., J. Buttles, and P. Olson, Laboratory experiments on structure of subducted lithosphere, *Earth Planet. Sci. Lett.*, 133, 19– 34, 1995.

Gutenberg, B., and C. F. Richter, Seismicity of the Earth and Associated Phenomena, 310 pp., *Princeton Univ. Press*, Princeton, N. J, 1954

Hall Sir, J., On the vertical position and convolution of certain strata, and their relation with granite. *Trans R. Soc. Edin*. 7, 79–108, 1815.

Hatzfeld, D., Martinod, J., Bastet, G., Gautier, P., An analog experiment for the Aegean to describe the contribution of gravitational potential energy. Journal of Geophysical Research 102, 649–659, 1997.

Heuret A. et S., Lallemand, Plate motions, slab dynamics and back-arc deformation. *Physics of the Earth and Planetary Interiors*, 149, 31-51, 2005.

Heuret, A., Funiciello, F., Faccenna, C., and Lallemand, S., Plate kinematics, slab shape and back-arc stress: A comparison between laboratory models and current subduction zones: *Earth and Planetary Science Letters*, v. 256, p. 473–483, doi: 10.1016/j.epsl.2007.02.004, 2007.

Horsfield W.T., An experimental approach to basement controlled faulting, *Geologie en Mijnbouw,* 56, 363-370, 1977.

Hubbert, M.K., Theory of scale models as applied to the study of geologic structures. *Bull. Geol. Soc. Am*. 48, 1459–1520, 1937.

Keep, M., McClay, K.R., Analogue modelling of multiphase rift systems. *Tectonophysics* 273, 239–270, 1997.

Kincaid, C., Griffiths, R.W., 2003. Laboratory models of the thermal evolution of the mantle during rollback subduction. *Nature* 425, 58–62.

Kincaid, C., Olson, P., An experimental study of subduction and slab migration. *J. Geophys. Res*. 92 (B13), 13832–13840, 1987.

Krantz, R.W., Measurements of friction coefficients and cohesion for faulting and fault reactivation in laboratory models using sand and sand mixtures. *Tectonophysics* 188, 203–207, 1991.

Lallemand, S.E., Malavieille, J., Calassou, S., Effects of oceanic ridge subduction on accretionary wedges: experimental modeling and marine observations. *Tectonics* 11, 1301–1313, 1992.

Lin, J., and R. S. Stein, Stress triggering in thrust and subduction earthquakes and stress interaction between the southern San Andreas and nearby thrust and strike-slip faults, J. Geophys. Res., 109, B02303, doi:10.1029/2003JB002607, 2004.

Liu, S. & Dixon, J.M., Centrifuge modelling of thrust faulting: structural variation along strike in fold-thrust belts. *Tectonophys*, 188, 39-62, 1991.

Lykotrafitis, G., et al., Self-healing pulse-like shear ruptures in the laboratory, *Science*, 313, 1765– 1768, doi:10.1126/science.1128359, 2006.

Mart Y., E. Aharonov, G. Mulugeta, W. Ryan, T. Tentler, L.Goren, Analogue modelling of the initiation of subduction *Geophysical Journal International*, 160, (3), 1081–1091, 2005.

McClay, K.R., Deformation mechanics in analogue models of extensional fault systems. *Geological Society of London Special Publications* 54, 445– 453, 1990.

Mulugeta, G., Squeeze box in a centrifuge. *Tectonophysics*, 148, 323–335, 1988.

Naylor M.A., G. Mandl, C.H. Sijpesteiln, Fault geometries in basement-induced wrench faulting under different internal states, *J. Struct. Geol.*, 8 737-752, 1986.

Nieuwland D.A. and J.V. Walters, Geomechanics of the South Furious field. An integrated approach towards solving complex structural geological problems, including analogue and finite-element modelling, *Tectonophysics* 226, pp. 143–166, 1993.

Pacheco, J. F. and L. R. Sykes, Seismic Moment Catalog of Large Shallow Earthquakes, 1900 to 1989, *Bull. Seismol. Soc. Am.*, 82(3), 1306-1349, 1992.

Ratschbacher, L., Merle, O., Davy, P., Cobbold, P., Lateral extrusion in the Eastern Alps, part 1: boundary conditions and experiments scaled for gravity. *Tectonics* 10, 245–256, 1991.

Ramberg, H., Gravity, Deformation and the Earth's Crust. *Academic Press, London*, 1967.

Ribe N.M., Stutzmann E., Ren Y., van der Hilst R., Buckling instabilities of subducted lithosphere beneath the transition zone. *Earth Planet Sci Lett*, 254:173–179, 2007.

Richard, P., Experiments on faulting in a two-layered cover sequence overlying a reactivated basement fault with oblique-slip. *Journal of Structural Geology* 13, 459–469, 1991.

Richard, P., Krantz, R.W., Experiments on fault reactivation in strike-slip mode. *Tectonophysics* 188, 117–131, 1991.

Richard, P.D., Moquet, B., Cobbold, P.R., Experiments on simultaneous faulting and folding above a basement wrench fault. *Tectonophysics* 188, 133–141, 1991.

Richard, P.D., Naylor, M.A., Koopman, A., Experimental models of strike-slip tectonics. *Petroleum Geoscience* 1, 71– 80, 1995.

Rosenau, M., J. Lohrmann and O. Oncken, Shocks in a box: An analogue model of subduction earthquake cycles with application to seismotectonic forearc evolution, *J. Geophys. Res., [Solid Earth]*, 114, B01409, doi:10.1029/2008JB005665, 2009.

Rossi, D., and F. Storti, New artificial granular materials for analogue laboratory experiments: Aluminium and siliceous microspheres, *J. Struct. Geol.*, 25, 1893–1899 2003.

Rubio, M. A. and J. Galeano, Stick-Slip Dynamics in the Relaxation of Stresses in a Continuous Elastic Medium, *Phys Rev E*, 50(2), 1000-1004, 1994.

Russo, R. M., and P. G. Silver, Trench-parallel flow beneath the Nazca plate from seismic anisotropy, *Science*, 263, 1105– 1111, 1994.

Schellart W.P., Shear test results for cohesion and friction coefficients for different granular materials: scaling implications for their usage in analogue modeling. *Tectonophysics* 324, 1–16, 2000.

Schellart W.P., Kinematics of subduction and subduction-induced flow in the upper mantle. *Journal of Geophysical Research* 109, B07401, doi:10.1029/2004JB002970, 2004.

Schellart, W.P., Estimate of the slab to upper mantle effective viscosity ratio from fluid dynamic models of subduction, *Bollettino di Geofisica Teorica ed Applicata*, 49 (suppl. 2), 194-198, 2008.

Schellart, W.P., Evolution of the slab bending radius and the bending dissipation in three-dimensional subduction models with a variable slab to upper mantle viscosity ratio. *Earth and Planetary Science Letters 288*, 309-319, doi:10.1016/j.epsl.2009.09.034, 2009.

Scholz, C. H., Earthquakes and friction laws, *Nature*, 391(6662), 37-42, 1998.

ten Grotenhuis, S.M., Piazolo, S., Pakula, T., Passchier, C.W., Baus, P.D., Are polymers suitable rock analogs? *Tectonophysics* 350, 35–47, 2002.

Tovish, A., Schubert, G., and Luyendyk, B.P., Mantle fl ow pressure and the angle of subduction: Non-Newtonian corner fl ows: *Journal of Geophysical Research*, v. 83, no. B12, p. 5892–5898, 1978.

Van der Hilst, R.D., Widiyantoro, S., and Engdahl, E.R., Evidence for deep mantle circulation from global tomography. *Nature*, 386, 578- 584, 1997.

Vargas, C. A., E. Basurto, L. Guzman-Vargas and F. Angulo-Brown, Sliding size distribution in a simple spring-block system with asperities, *Physica A*, 387(13), 3137-3144, doi:10.1016/j.physa.2008.01.108, 2008.

Vendeville B., Cobbold P.R., Davy P., Brun J.P. & Choukroune P., Physical models of extensional tectonics at various scales, in Coward M.P., Dewey J.F. & Hancock P.L. (eds) *Continental Extensional Tectonics*, 1987.

Voisin, C., F. Renard and J. R. Grasso, Long term friction: From stick-slip to stable sliding, *Geophys. Res. Lett.*, 34(13), L13301, doi:10.1029/2007GL029715, 2007.

Voisin, C., J. R. Grasso, E. Larose and F. Renard, Evolution of seismic signals and slip patterns along subduction zones: Insights from a friction lab scale experiment, *Geophys. Res. Lett.*, 35(8), L08302, doi:10.1029/2008GL033356, 2008.

Wang, K., Y. Hu, M. Bevis, E. Kendrick, R. Smalley Jr., R. B. Vargas, and E. Laurı́a, Crustal motion in the zone of the 1960 Chile earthquake: Detangling earthquake-cycle deformation and forearc-sliver translation, 8, Q10010, doi:10.1029/2007GC001721, 2007.

Weijermars, R. and H. Schmeling, Scaling of newtonian and non newtonian fluid dynamics without inertia for qantitative modelling of rock flow due to gravity (including the concept of rheological similarity), *Physics of the Earth and Planetary Interiors*, 43, 316-330, 1986.

Zheng, G., R. Dmowska, and J. R. Rice, Modeling earthquake cycles in the Shumagin subduction segment, Alaska, with seismic and geodetic constraints, *J. Geophys. Res.*, 101(B4), 8383– 8392, 1996.

Chapter 3

Allmendinger, R.W., Smalley, R. Jr, Bevis, M., Caprio, H., and Brooks, B., Bending the Bolivian orocline in real time: *Geology*, 33, 905-908, 2005.

Arriagada, C., Roperch, P., Mpodozis, C., and Cobbold, P.R., Paleogene building of the Bolivian Orocline: Tectonic restoration of the central Andes in 2-D map view: *Tectonics*, 27, 2008.

Boutelier, D.A., and Oncken, O., Role of the plate margin curvature in the plateau buildup: Consequences for the central Andes: *Journal of Geophysical Research*, 115, B04402, 2010.

Funiciello, F., Faccenna, C., Giardini, D., and Regenauer-Lieb, K., Dynamics of retreating slabs: 2. Insights from three-dimensional laboratory experiments: *Journal of Geophysical Research*, 108, 2207, 2003.

Ghosh, P., Garzione, C.N., Eiler, J.M., Rapid uplift of the Altiplano revealed through 13C-18O bonds in paleosol carbonates: *Science*, 311, p. 511-515, 2006.

Gregory-Wodzicki, K.M., Uplift history of the central and northern Andes: A review: *Geological Society of America Bulletin*, 112, 1091– 1105, 2000.

Hindle, D., Kley, J., Oncken, O., and Sobolev, S., Crustal balance and crustal flux from shortening estimates in the Central Andes: *Earth and Planetary Science Letters*, 230, 113-124, 2005.

Iaffaldano, G., Bunge, H.-P., and Dixon, T.H., Feedback between mountain belt growth and plate convergence: *Geology*, 36, 443-446, 2006.

Iaffaldano, G., and Bunge, H.-P., Strong plate coupling along the Nazca- South America convergent margin: *Geology*, 34, 893-896. 2008.

Iaffaldano, G., and Bunge, H.-P., Relating rapid plate-motion variations to plate-boundary forces in global coupled models of the mantle/lithosphere system: Effects of topography and friction: *Tectonophysics*, 474, 393-404, 2009.

Isacks, B.L., Uplift of the central Anead plateau and bending of the Bolivian orocline: *Journal of Geophysical Research*, 93, 3211-3231, 1998.

Klay, J. and Monaldi, C.R., Tectonic shortening and crustal thickness in the Central Andes: How good in the correlation?: *Geology*, 26, 723-726 1998.

Kopf, A, and Brown, K.M., Friction experiments on saturated sediments and their implications for the stress state of the Nankai and Barbados subduction thrusts: *Marine Geology*, 202, 193-210, 2003.

Lamb, S., and Davies, P., Cenozoic climate change as a possible cause for the rise of the Andes: *Nature*, 425, 792-797, 2003.

Maffione, M. Speranza, F., and Faccenna, C., Bending of the Bolivian orocline and growth of the central Andean plateau: Paleomagnetic and structural constraints from the Eastern Cordillera (22-24 degrees S, NW Argentina): *Tectonics*, 28, 2009.

Marques, F.O., and Cobbold, P.R., Effects of topography on the curvature of fold-and-thrust belts during shortening of a 2-layer model of continent lithosphere: *Tectonophysics*, 415, 65-80, 2006.

Mart, Y., Aharonov, E., Mulugeta, G., Ryan, W., Tentler, T., and Goren, L., Analogue modelling of the initiation of subduction: *Geophysical Journal International*, 160, 1081-1091 2005.

McKenzie, D.P., Speculations on consequences and causes of plate motions: *Geophysical Journal of the Royal Astronomical Society*, 8, 1-8, 1969.

Montgomery, D.R., Balco, G., Willett, S.D., Climate, tectonics, and the morphology of the Andes: *Geology*, 29, 579-582, 2001.

Morgan, W.J., Rises, trenches, great faults, and crustal blocks: *Journal of Geophysical Research*, 73, 1959–1982, 1968.

Morra, G., Regenauer-Lieb, K., and Giardini, D., Curvature of oceanic arcs: *Geology*, 34, 877-880, 2006.

Mueller, R.D., Sdrolias, M., Gaina, C., Steinberger, B., and Heine, C., Long-term sea-level fluctuations driven by ocean basin dynamics: *Science*, 319, 1357-1362, 2008.

Rousse, S., Gilder, S., Farber, D., McNulty, B., Patriat, P., Torres, V., and Sempere, T., Paleomagnetic tracking of mountain building in the Peruvian Andes since 10 Ma: *Tectonics*, 22, 1048, 2003.

Russo, R.M., and Silver, P.G., Cordillera formation, mantle dynamics, and the Wilson cycle: *Geology*, 24, 511-514, 1996.

Schellart, W.P., Freeman, J., Stegman, D.R., Moresi, L., and May, D., Evolution and diversity of subduction zones controlled by slab width: *Nature*, 446, 308-311, 2007.

Chapter 4

Acocella, V., Tibaldi, A., Dike propagation driven by volcano collapse: a general model tested at Stromboli, Italy. *Geophysical Research Letters* 32, L08308. doi:10.1029/2004GL022248, 2005.

Askeland, D.R., The Science and Engineering of Materials. *PWSPub*, Boston. 812, 1994.

Bagdassarov, N., Dorfman, A., Viscoelastic behavior of partially molten granites. *Tectonophysics* 290, 27–45, 1998.

Barnes, H.A., Hutton, J.F.,Walters, K., An Introduction to Rheology. Elsevier Science Publishing Company, New York. 212, 1989.

Barrangou, L.M., Daubert, C.R., Foegeding, E.A., Textural properties of agarose gels. I. Rheological and fracture properties. *Food Hydrocolloids* 20, 184–195, 2006.

Bons, P.D., Elburg, M.A., Dougherty-Page, J., Analogue modeling of segregation and ascent of magma. In: Rawling, T., Ailleres, L. (Eds.), Animations in Geology. *Journalof the Virtual Explorer*, 4, 5–10, 2001.

Bot, A., van Amerongen, I.A., Groot, R.D., Hoekstra, N.L., Agterof, W.G.M., Large deformation rheology of gelatin gels. *Polymer Gels and Network* 4, 189–227, 1996a.

Bot, A., Groot, R.D., Agterof, W.G.M., Non-linear elasticity and rupture of gelatin gels. In: Philipps, G.O., Williams, P.A., Wedlock, D.J. (Eds.), *Gums and Stabilizers for the Food Industry* 8. IRL Press, Oxford, 117–126, 1996b.

Boudreau, B.P., Algar, C., Johnson, B.D., Croudace, I., Reed, A., Furukawa, Y., Dorgan, K.M., Jumars, P.A.,Grader, A.S.,Gardiner, B.S., Bubble growth and rise in soft sediments. *Geology* 33, 517–520, 2005.

Boutelier, D., Schrank, C., Cruden, A., Power-law viscous materials for analogue experiments: new data on the rheology of highly-filled silicone polymers. *Journal of Structural Geology* 30, 341–353, 2008.

Brun, J.-P., Sokoutis, D., van den Driessche, J., Analogue modeling of detachment fault systems and core complexes. *Geology* 22, 319–322, 1994.

Chou, P.C., Pagano, N.J., The alternating tensor. Elasticity: Tensor, Dyadic, and Engineering Approaches. Dover, New York, 182–186, 1992.

Cobbold, P.R., Fold propagation in single embedded layers. *Tectonophysics* 27, 333–351, 1975.

Cobbold, P.R., Jackson, M.P.A., Gum rosin (colophony): a suitable material for thermomechanical modeling of the lithosphere. *Tectonophysics* 210, 255–271, 1992.

Craig, C.H., McKenzie, D., The existence of a thin low-viscosity layer beneath the lithosphere. *Earth and Planetary Science Letters* 78, 420–426, 1986.

Davaille, A., 1999. Simultaneous generation of hotspots and superswells by convection in a heterogeneous planetary mantle. *Nature* 402, 756–760.

Davidson, R.L., Handbook of Water-soluble Gums and Resins. McGraw Hill0-07- 015471-6, 1980.

Davy, P., Cobbold, P.R., Indentation tectonics in nature and experiment. 1. Experiments scaled for gravity. *Bulletin of the Geological Institute of Uppsala*, New Series 14, 129–141, 1988.

Davy, P., Cobbold, P.R., Experiments onshortening of a 4-layer continental lithosphere. *Tectonophysics* 188, 1–25, 1991.

Drozdov, A.D., Finite Elasticity and Viscoelaticity. *World Scientific Publishing*, Singapore. 434, 1996.

Eisenstadt, G., Sims, D., Evaluating sand and clay models: do rheological differences matter? *Journal of Structural Geology* 27 (8), 1399–1412, 2005.

Ferry, J.D., Viscoelatic Properties of Polymers, 3rd ed. Wiley Blackwell. 672, 1980.

Fiske, R.F., Jackson, E.D., Orientation and growth of Hawaiian volcanic rifts: the effect of regional structure and gravitational stresses. *Proceedings of the Royal Society of London*, Series A 329, 299–326, 1972.

Funiciello, F., Faccenna, C., Giardini, D., Regenauer-Lieb, K., Dynamics of retreating slabs (part 2): insights from 3D laboratory experiments. *Journal of Geophysical Research* 108. doi:10.1029/2001JB000896, 2003.

Galland, O., Cobbold, P.R., Hallot, E., d Ars, J., Delavaud, G., Use of vegetable oil and silica powder for scale modeling of magmatic intrusion in a deforming brittle crust. *Earth and Planetary Science Letters* 243, 786–804, 2006.

Griffiths, R.W., Hackney, R.I., van der Hilst, R.D., A laboratory investigation of effects of trench migration on the descent of subducted slabs. *Earth and Planetary Science Letters* 133, 1–17, 1995.

Grujic, D., Mancktelow, N.S., Folds with axes parallel to the extension direction: an experimental study. *Journal of Structural Geology* 17, 279–291, 1995.

Heimpel, M., Olson, P., Buoyancy-driven fracture and magma transport through the lithosphere: models and experiments. In: Ryan, P. (Ed.), *Magmatic Systems. Academic Press*, 223–240, 1994.

Hubbert, M.K., Theory of scale models as applied to the study of geologic structures. *Bulletin of the Geological Society of America* 48, 1459–1520, 1937.

Hubbert, M.K., Mechanical basis for certain familiar geological structures. *Geological Society of America Bulletin* 62, 355–372, 1951.

Hyndman, D.W., Alt, D., Radial dikes, laccoliths, and gelatinmodels. *Journal of Geology* 95, 763–774, 1987.

Ito, G., Martel, S.J., Focusing of magma in the upper mantle through dike interaction. *Journal of Geophysical Research* 107. doi:10.1029/2001JB000251, 2002.

James, M.R., Bagdassarov, N., Müller, K., Pinkerton, H., Viscoelastic behavior of basaltic lavas. *Journal of Volcanology and Geothermal Research* 132, 99–113, 2004.

Johnson, A.M., Pollard, D.P., Mechanics of growth of some laccolithic intrusions in the Herny Mountains, Utah. I. Field observations, Gilbert's model, physical properties and flow of magma. *Tectonophysics* 18, 261–309, 1973.

Kavanagh, G.M., Ross-Murphy, S.B., Rheological characterization of polymer gels. *Progress of Polymer Sciences* 23, 533–562, 1998.

Kavanagh, J.L., Menand, T., Sparks, R.S., An experimental investigation of sill formation and propagation in layered elastic media. *Earth and Planetary Science Letters* 245, 799–813, 2006.

Keep, M., McClay, K.R., Analoguemodeling ofmultiphase rift systems. *Tectonophysics* 273, 239–270, 1997.

Koyaguchi, T., Takada, A., An experimental study on the formation of composite intrusions from zoned magma chambers. *Journal of Volcanology and Geothermal Research* 59, 261–267, 1994.

Krantz, R.W., Measurements of friction coefficients and cohesion for faulting and fault reactivation in laboratory using sand and sandmixture. *Tectonophysics* 188, 203–207, 1991.

Lister, J.R., Kerr, R.C., Fluid-mechanicalmodels of crack-propagation and their application to magma transport in dykes. *Journal of Geophysical Research* 96, 10049–10077, 1991.

Mancktelow, N.S., The rheology of paraffin wax and its usefulness as an analogue for rocks. *Bulletin of the Geological Institute University of Uppsala* 14, 181–193, 1988.

Marin, G., Oscillatory rheometry. In: Collyer, A.A., Clegg, D.W. (Eds.), Rheological Measurements. Chapman and Hall, London, 5–46, 1998.

McGuire, W.J., Pullen, A.D., Location and orientation of eruptive fissures and feeder-dykes at Mount Etna: influence of gravitational and regional tectonic stress regimes. *Journal of Volcanology and Geothermal Research* 38, 325–344, 1989.

McLeod, P., Tait, S., The growth of dykes from magma chambers. *Journal of Volcanology and Geothermal Research* 92, 231–245, 1999.

Menand, T., Tait, S.R., A phenomenological model for precursor volcanic eruptions. *Nature* 411, 678–680, 2001.

Menand, T., Tait, S.R., The propagation of a buoyant liquid-filled fissure from a source under constant pressure: an experimental approach. *Journal of Geophysical Research* 107. doi:10.1029/2001JB000589, 2002.

Mezger, T.G., In: Ulrich, Zorll (Ed.), The Rheology Handbook: For Users of Rotational and Oscillatory Rheometers. Hannover, Germany. 2002.

Muller, J.R., Ito, G., Martel, S.J., Effects of volcano loading on dike propagation in an elastic half-space. *Journal of Geophysical Research* 106, 11,101–11,113, 2001.

Nelson, B.I., Dealy, J.M., Dynamic mechanical analysis using complex waveforms. In: Collyer, A.A. (Ed.), Techniques in Rheological Measurement. Chapman & Hall, Cambridge, pp. 197–224, 1993.

Norziah, M.H., Foo, S.L., Karim, A.A., Rheological studies on mixtures of agar (Gracilaria changii) and κ-carr. eenan. *Food Hydrocolloids* 20, 2006.

Nowick, A.S., Berry, B.S., Anelastic Relaxations in Crystalline Solids. Academic Press Inc., New York. 677, 1972.

Parsons, B., Sclater, J.G., Analysis of variation of ocean-floor bathymetry and heatflow with age. *Journal of Geophysical Research* 82, 803–827, 1977.

Pasquare, F.A., Tibaldi, A., Do transcurrent faults guide volcano growth? The case of NW Bicol Volcanic Arc, Luzon, Philippines. *Terra Nova* 15, 204–212, 2003.

Pollard, D.D., Johnson, A.M., Mechanics of growth of some laccolitihic intrusions in the Henry Mountains, Utah, II. Bending and failure of overburden layers and sill formation. *Tectonophysics* 18, 311–354, 1973.

Rahman, M.D.S., Food Properties Handbook. CRC Press, *Boca Raton*. 528, 1995.

Ramberg, H., Natural and experimental boudinage and pinch-and swell structures. *Journal of Geology* 63, 512–526, 1955.

Ramberg, H., Gravity, Deformation and the Earth's crust. New York, p. 452, 1981.

Ranalli, G., Average lithospheric stresses induced by thickness change: a linear approximation. Physics of the Earth and Planetary Interiors 69, 263–269, 1992.

Ranalli, G., Rheology of the Earth. Chapman and Hall, London. 413 pp., 1995.

Richard, P.D., Naylor, M.A., Koopman, A., Experimental models of strike-slip tectonics. *Petroleum Geoscience* 1, 71–80, 1995.

Rivalta, E., Böttinger, M., Dahm, T., Buoyancy-driven fracture ascent: experiments in layered gelatine. *Journal of Volcanology and Geothermal Research* 144, 273–285, 2005.

Rossetti, F., Ranalli, G., Faccenna, C., Rheology of paraffin wax as an analogue material for crustal deformation. *Journal of Structural Geology* 21, 413–417, 1999.

Schellart, W.P., Shear test results for cohesion and friction coefficients for different granular materials: scaling implications for their usage in analogue modeling. *Tectonophysics* 324, 1–16, 2000.

Shemenda, A.I., Subduction: Insights from Physical Modeling Modern Approaches in Geophysics. Kluwer, Netherlands. 215 pp., 1994.

Storti, F., McClay, K., Influence of syntectonic sedimentation on thrust wedges in analogue models. *Geology* 23, 999–1002, 1995.

Sumita, I., Manga, M., Suspension rheology under oscillatory shear and its geophysical implications. *Earth and Planetary Science Letters* 269, 467–476, 2008.

Takada, A., Experimental study on propagation of liquid-filled crack in gelatin: shape and velocity in hydrostatic condition. *Journal of Geophysical Research* 95, 8471–8481, 1990.

Takada, A., Development of a subvolcanic structure by the interaction of liquidfilled cracks. *Journal of Volcanology and Geothermal Research* 61, 207–224, 1994.

ten Grotenhuis, S.M., Piazolo, S., Pakula, T., Passchier, C.W., Baus, P.D., Are polymers suitable rock analogs? *Tectonophysics* 350, 35–47, 2002.

Tosh, S.M., Marangoni, A.G., Hallett, F.R., Britt, I.J., Aging dynamics in gelatin gel microstructure. *Food Hydrocolloids* 17, 503–513, 2003.

van Vliet, T.,Walstra, P., Large deformation and fracture behaviour of gels. *Faraday Discussions* 101, 359–370, 1995.

Walter, T.R., Troll, V.R., Experiments on rift zone evolution in unstable volcanic edifices. Journal of *Volcanology and Geothermal Research* 127, 107–120, 2003.

Watanabe, T., Koyaguchi, T., Seno, T., Tectonic stress control on ascent and emplacement of magmas. *Journal of Volcanology and Geothermal Research* 91, 65–78, 1999.

Watanabe, T., Masuyama, T., Nagaoka, K., Tahara, T., Analog experiments on mama-filled cracks: competition between external stresses and internal pressure. *Earth Planets Space* 54, 1247–1261, 2002.

Weijermars, R., Flowbehavior and physical chemistry of bouncing putties and related polymers in view of tectonic laboratory application. *Tectonophysics* 124, 325–358, 1986.

Weijermars, R., Schmeling, H., Scaling of newtonian and non newtonian fluid dynamics without inertia for quantitative modelling of rock flow due to gravity (including the concept of rheological similarity). *Physics of the Earth and Planetary Interiors* 43, 316–330, 1986.

Weijermars, R., Jackson, M.P.A., Vendeville, B., Rheological and tectonic modeling of salt provinces. *Tectonophysics* 217, 143–174, 1993.

Williams,R.,Mittal,G.S., Low-fat foodswith edible coatings:modeling and simulation. *Journal of Food Science* 64, 317–322, 2006.

Chapter 5

Abers, G., B. Parsons and J., Weissel, Seamount abundances and distributions in the southeast Pacific, *Earth Planet. Sci. Lett.*, 87(1 - 2), 137-151, 1988.

Aki, K., Earthquake mechanism, *Tectonophysics*, 13, 423-446, 1972.

Aki, K., Asperities, barriers, characteristic earthquakes and strong motion prediction, *J. Geophys. Res.*, 89, 5867-5872, 1984.

Amontons, G., De la résistance causée dans les machines, *Mém. Acad. R. Sci*., 206-226, 1699.

Balsamo, F. and F. Storti, Grain size and permeability evolution of soft-sediment extensional sub-seismic and seismic fault zones in high-porosity sediments from the Crotone basin, southern Apennines, Italy, *Mar. Pet. Geol.*, 27(4), 822-837, doi:10.1016/j.jsg.2009.10.010, 2010.

Baumberger, T., C. Caroli and O. Ronsin, Self-healing slip pulses along a gel/glass interface, *Phys. Rev. Lett.*, 88(7), 1-4, 2002.

Baumberger, T., C. Caroli and O. Ronsin, Self-healing slip pulses and the friction of gelatin gels, *Eur. Phys. J. E: Soft Matter Biol. Phys*., 11(1), 85-93, doi:10.1140/epje/i2003-10009-7, 2003.

Biegel, R. L., C. G. Sammis and J. H. Dieterich, The frictional properties of a simulated gouge having a fractal particle distribution, *J. Struct. Geol.*, 11(7), 827-846, 1989.

Bilek, S. L., Influence of subducting topography on earthquake rupture, in The seismogenic zone of subduction thrust fault, edited by T. Dixon and C. Moore, pp. 123-146, Columbia University Press, New York, 2007.

Bird, P., Y. Y. Kagan, D. D. Jackson, F. P. Schoenberg and M. J. Werner, Linear and Nonlinear Relations between Relative Plate Velocity and Seismicity, *Bull. Seismol. Soc. Am.*, 99(6), 3097-3113, doi:10.1785/0120090082, 2009.

Bird, R., R. C. Armstrong and O. Hassager, Dynamics of Polymeric Liquids, John Wiley and Sons Inc., New York, NY, 1987.

Bowden, F. P. and D. Tabor, The friction and lubrication of solids. Pt I, Oxford Univ. Press Inc., New York, 1950.

Brace, W. F. and D. L. Kohlsted, Limits on lithospheric stress imposed by laboratory experiments, *J. Geophys. Res.*, 85, 6248-6252, 1980.

Brodsky, E., J. Gilchrist, A. Sagy, and C. Collettini, Faults smooth gradually as a function of slip, *Earth Planet. Sci. Lett.,* 302 (2011) 185–193, 2010.

Burridge, R. and L. Knopoff, Model and theoretical seismicity, *Bull. Seismol. Soc. Am.*, 57, 341-371, 1967.

Byerlee, J. D., Frictional characteristics of granite under high confining pressure *J. Geophys. Res.*, 72(14 (1967)), 3639-3648, 1967.

Byerlee, J. D., Static and kinetic function of granite at high normal stress*, Int. J. Rock Mech. Min. Sci*, 7, 577-582, 1970.

Charitat, T. and J. F. Joanny, Solid-like friction of a polymer chain, Eur. Phys. J. E*: Soft Matter Biol. Phys.*, 3(4), 369-376, 2000.

Choi, Y. S., H. R. Piehler and A. D. Rollett, Introduction and application of modified surface roughness parameters based on the topographical distributions of peaks and valleys, *Mater. Charact.,* 58(10), 901-908, doi:10.1016/j.matchar.2006.09.003, 2007.

Cloos, M., Thrust-Type Subduction-Zone Earthquakes and Seamount Asperities - a Physical Model for Seismic Rupture, *Geology*, 20(7), 601-604, 1992.

Coulomb, C. A., Théorie des machines simples, *Mem.Math.Phys.Acad.Sci.*, 10, 161-331, 1785.

Currie, C. A., R. D. Hyndman, K. Wang and V. Kostoglodov, Thermal models of the Mexico subduction zone: Implications for the megathrust seismogenic zone, *J. Geophys. Res., [Solid Earth],* 107(B12), 2370, doi:10.1029/2001jb000886, 2002.

Das, S. and C. Scholz, Why large earthquakes do not nucleate at shallow depths, *Nature*, 305, 621-623, 1983

Di Giuseppe, E., F. Funiciello, F. Corbi, G. Ranalli and G. Mojoli, Gelatins as rock analogs: A systematic study of their rheological and physical properties, *Tectonophysics*, 473(3-4), 391-403, doi:10.1016/j.tecto.2009.03.012, 2009.

Dieterich, J. H., Modeling of rock friction. 1. Experimental results and constitutive equations, *J. Geophys. Res.*, 84(NB5), 2161-2168, 1979.

Dieterich, J. H., Constitutive properties of faults with simulated gouge, in Mechanical Behavior of Crustal Rocks, Geophys. Mono. Ser., edited by N. L. Carter, et al., pp. 103-120, AGU, Washington DC, 1981.

Dziewonski A. M., and J. H. Woodhouse, Determination of earthquake source parameters from waveform data for studies of global and regional seismicity, *J. Geophys. Res.,* 86, 2825-2852, 1981

Engdahl R., R. Van Der Hilst and R. Buland, Global teleisismic earthquake relocation with improved travel times and procedures for depth determination, *Bull. Seism. Soc. Amer.*, 88, 722-743, 1998.

Engelder, T. and C. H. Scholz, The role of asperity indentation and ploughing in rock friction, 2: influence of relative hardness and normal load, *Int. J. Rock Mech. Min. Sci,* 13, 155-163, 1976.

Engelder, T., Aspects of asperity-surface interaction and surface damage of rocks during experimental frictional sliding, *Pure Appl. Geophys.*, 116, 706-716, 1978.

Gomberg, J. and C. W. Grp, Slow-slip phenomena in Cascadia from 2007 and beyond: A review, *Geol. Soc. Am. Bull.*, 122(7-8), 963-978, doi:10.1130/B30287.1, 2010.

Gutenberg, B., and C. F. Richter, Seismicity of the Earth and Associated Phenomena, 310 pp., *Princeton Univ. Press*, Princeton, N. J, 1954

Gutscher, M. A. and G. K. Westbrook, Great earthquakes in slow-subduction, low-taper margins, in Subduction zone geodynamics, edited by S. Lallemand and F. Funiciello, pp. 119-133, Springer Berlin Heidelberg, 2009.

Hanks, T. and H. Kanamori, A moment magnitude scale, *J. Geophys. Res.*, 84(b5), 2348-2350, 1979.

Hayes C.W. and C.P. Conrad, Subduction Dynamics and Great Earthquakes, American Geophysical Union Fall Meeting, San Francisco, CA, 2007.

Hayes, D. E. and K. A. Kane, The Dependence of Sea-Floor Roughness on Spreading Rate, *Geophys. Res. Lett.*, 18(8), 1425-1428, 1991.

Heslot, F., T. Baumberger, B. Perrin, B. Caroli and C. Caroli, Creep, Stick-Slip, and Dry-Friction Dynamics - Experiments and a Heuristic Model, *Phys Rev E*, 49(6), 4973-4988, 1994.

Heuret, A., S. Lallemand, F. Funiciello, C. Piromallo, C. Faccenna, Physical properties of subduction-type seismogenic zones revisited, *Geochem. Geophys. Geosyst.*, in press.

Higashi, N. and I. Sumita, Experiments on granular rheology: Effects of particle size and fluid viscosity, *J. Geophys. Res., [Solid Earth],* 114, B04413, doi:10.1029/2008JB005999, 2009.

Hyndman, R. D. and K. Wang, Thermal Constraints on the Zone of Major Thrust Earthquake Failure - the Cascadia Subduction Zone, *J. Geophys. Res., [Solid Earth],* 98(B2), 2039-2060, 1993.

Hyndman R. D., M. Yamano, K. Wang, Thermal constraints on the seismogenic portion of the southwestern Japan subduction thrust, *J. Geophys. Res.*, 100, 15373-15392, 1995.

Hyndman, R. D., M. Yamano and D. A. Oleskevich, The seismogenic zone of subduction thrust faults, *Isl. Arc*, 6(3), 244-260, 1997

Jordan, T. H., H. W. Menard and D. K. Smith, Density and size distribution of seamounts in the eastern Pacific inferred from wide-beam sounding data, *J. Geophys. Res.*, 88(NB12), 508-518, 1983.

Kanamori H., The energy release in great earthquakes, *J. Geophys. Res.*, 82, 2981 - 2987, 1977.

Lallemand, S., A. Heuret, C. Faccenna and F. Funiciello, Subduction dynamics as revealed by trench migration, *Tectonics*, 27(3), TC3014, doi:10.1029/2007TC002212, 2008.

Lapusta, N., J. R. Rice, Y. Ben-Zion and G. T. Zheng, Elastodynamic analysis for slow tectonic loading with spontaneous rupture episodes on faults with rate- and state-dependent friction, *J. Geophys. Res., [Solid Earth],* 105(B10), 23765-23789, 2000.

Lay, T. and H. Kanamori, An asperity model of large earthquake sequences, in Earthquake Prediction - an International Review, edited by D. W. Simpson and P. G. Richards, pp. 579-592, AGU, Washington, DC, 1981.

Lay, T., H. Kanamori and L. Ruff, The asperity model and the nature of large subduction zone earthquakes, *Earthquake Pred. Res.*, 1, 3-71, 1982.

Marone, C. and B. Kilgore, Scaling of the Critical Slip Distance for Seismic Faulting with Shear Strain in Fault Zones, *Nature*, 362(6421), 618-621, 1993.

Marone, C. and S. J. D. Cox, Scaling of Rock Friction Constitutive Parameters - the Effects of Surface-Roughness and Cumulative Offset on Friction of Gabbro, *Pure Appl. Geophys.*, 143(1-3), 359-385, 1994.

Marone, C., J.E. Vidale and W.L. Ellsworth, Fault healing inferred from time dependent variations in source properties of repeating earthquakes, *Geophys. Res. Lett.* 22, (22), 3095-3098, 1995.

Marone, C. and C. H. Scholz, The depth of seismic faulting and the upper transition from stable to unstable slip regimes, *Geophys. Res. Lett.*, 15(6), 621 – 624, 1988.

Marone, C. and D. M. Saffer, Fault friction and the upper transition from seismic to aseismic faulting, in The seismogenic zone of subduction thrust fault, edited by T. Dixon and C. Moore, pp. 346-369, Columbia University Press, New York, 2007.

McCaffrey, R., Influences of recurrence times and fault zone temperature on the age-rate dependence of subduction zone seismicity, *J. Geophys. Res.*, 102, 22,839– 22,854, doi:10.1029/97JB01827, 1997.

McCaffrey, R., The next great earthquake, Science, 315(5819), 1675-1676, doi:10.1126/science.1140173, 2007.

McCaffrey, R., Global frequency of magnitude 9 earthquakes, *Geology*, 36(3), 263-266, doi:10.1130/G24402A.1, 2008.

Molnar, P., Earthquake recurrence intervals and plate tectonics, *Bull. Seismol. Soc. Am.*, 69(1), 115–133, 1979.

Moore, J.C., and D. Saffer, Updip limit of the seismogenic zone beneath the accretionary prism of southwest Japan: An effect of diagenetic to low-grade metamorphic processes and increasing effective stress: *Geology*, 29, 183–196, 2001.

Nelson, B.I., and Dealy, J.M., Dynamic-mechanical analysis using complex waveforms. In: Collyer, A.A. (Ed.), Techniques in Rheological Measurement. Chapman&Hall, Cambridge, pp. 197-224, 1993.

Ohnaka, M., A constitutive scaling law and a unified comprehension for frictional slip failure, shear fracture of intact rock, and earthquake rupture, *J. Geophys. Res.*, 108(B2), 2080, doi:10.1029/2000JB000123, 2003.

Pacheco, J. F. and L. R. Sykes, Seismic Moment Catalog of Large Shallow Earthquakes, 1900 to 1989, *Bull. Seismol. Soc. Am.*, 82(3), 1306-1349, 1992.

Pacheco, J. F., L. R. Sykes and C. H. Scholz, Nature of Seismic Coupling Along Simple Plate Boundaries of the Subduction Type, *J. Geophys. Res., [Solid Earth],* 98(B8), 14133-14159, 1993.

Peacock, S. M. and R. D. Hyndman, Hydrous minerals in the mantle wedge and the maximum depth of subduction thrust earthquakes, *Geophys. Res. Lett.,* 26(16), 2517-2520, 1999.

Pytte, A. and R. C. Reynolds, The thermal transformation of smectite to illite, in Thermal Histories of Sedimentary Basins, edited by T. H. McCulloh and N. D. Naeser, pp. 133-140, Springer, New York, 1988.

Rice, J. R., Spatiotemporal Complexity of Slip on a Fault, *J. Geophys. Res., [Solid Earth],* 98(B6), 9885-9907, 1993.

Rosenau, M., J. Lohrmann and O. Oncken, Shocks in a box: An analogue model of subduction earthquake cycles with application to seismotectonic forearc evolution, *J. Geophys. Res., [Solid Earth]*, 114, B01409, doi:10.1029/2008JB005665, 2009.

Rubio, M. A. and J. Galeano, Stick-Slip Dynamics in the Relaxation of Stresses in a Continuous Elastic Medium, *Phys Rev E*, 50(2), 1000-1004, 1994.

Ruff, L. and H. Kanamori, Seismic coupling and uncoupling at subduction zones, *Tectonophysics*, 99, 99-117.

Ruff, L. (1989), Do trench sediments affect great earthquake occurrence in subduction zones?, *Pure Appl. Geophys.*, 129, 262 – 282, 1983.

Ruina, A., Slip instability and state variable friction laws, *J. Geophys. Res.*, 88(NB12), 359-370, 1983.

Saffer, D. M. and C. Marone, Comparison of smectite- and illite-rich gouge frictional properties: application to the updip limit of the seismogenic zone along subduction megathrusts, *Earth Planet. Sci. Lett.*, 215(1-2), 219-235, doi:10.1016/S0012-821X(03)00424-2, 2003.

Sagy, A., E. E. Brodsky and G. J. Axen, Evolution of fault-surface roughness with slip, *Geology*, 35(3), 283-286, doi:10.1130/G23235a.1, 2007.

Scholz, C. H., P. Molnar and T. Johnson, Detailed studies of frictional sliding of granite and implications for the earthquake mechanism, *J. Geophys. Res.*, 77, 6392-6406, 1972.

Scholz, C. H. and J. T. Engelder, The role of asperity indentation and plounghing in rock friction: 1. Asperity creep and stick-slip, *Int. J. Rock Mech. Min. Sci*, 13, 149-154, 1976.

Scholz, C. H., Geophysics - Earthquakes as Chaos, *Nature*, 348(6298), 197-198, 1990.

Scholz, C. H., Earthquakes and friction laws, *Nature*, 391(6662), 37-42, 1998.

Schwartz, S. Y. and J. M. Rokosky, Slow slip events and seismic tremor at circum-pacific subduction zones, *Rev. Geophys.*, 45(3), RG3004, 2007.

Seno, T., Fractal asperities, invasion of barriers, and interplate earthquakes, *Earth, Planets Space,* 55(11), 649-665, 2003.

Smith, D. K. and T. H. Jordan, Seamount Statistics in the Pacific Ocean, *J. Geophys. Res.*, 93(B4), 2899-2918, 1988.

Storti, F., F. Balsamo and F. Salvini, Particle shape evolution in natural carbonate granular wear material, *Terra Nova*, 19(5), 344-352, doi:10.1111/j.1365-3121.2007.00758.x, 2007.

Vargas, C. A., E. Basurto, L. Guzman-Vargas and F. Angulo-Brown, Sliding size distribution in a simple spring-block system with asperities, *Physica A*, 387(13), 3137-3144, doi:10.1016/j.physa.2008.01.108, 2008.

Voisin, C., F. Renard and J. R. Grasso, Long term friction: From stick-slip to stable sliding, *Geophys. Res. Lett.*, 34(13), L13301, doi:10.1029/2007GL029715, 2007.

Voisin, C., J. R. Grasso, E. Larose and F. Renard, Evolution of seismic signals and slip patterns along subduction zones: Insights from a friction lab scale experiment, *Geophys. Res. Lett.,* 35(8), L08302, doi:10.1029/2008GL033356, 2008.

Wang, K., Coupling of tectonic loading and earthquake fault slips at subduction zones, *Pure Appl. Geophys.*, 145(3/4), 537-559, 1995.

Wang, K., Finding Fault in Fault Zones, *Science*, 329(5988), 152-153, doi:10.1126/science.1192223, 2010a.

Wang, K., What facilitates or hinders giant earthquakes, paper presented at AGU Chapman Conference on Giant Earthquakes and their Tsunamis, Valparaiso, Chile, 2010b.

Weijermars, R. and H. Schmeling, Scaling of Newtonian and non- Newtonian fluid dynamics without inertia for quantitative modeling of rock flow due to gravity (including the concept of rheological similarity). *Phys Earth Planet In*, 43, 316-330, 1986.

Chapter 6

Abe and Kanamori , Magnitudes of great shallow earthquakes from 1953 to 1977. *Tectonophysics* 62, 191–203, 1980.

Ammon, C. J., Kanamori, H., Lay, T. & Velasco, A. A. The 17 July 2006 Java tsunami earthquake (Mw 5 7.8). *Geophys. Res. Lett.* 33, L24308, doi:10.10239/ 2006GL028005, 2006.

Atwater, B. F., Evidence for great Holocene earthquakes along the outer coast of Washington State, *Science*, 236, 942– 944, 1987.

Atwater, B. F., and E. Hemphill-Haley, Recurrence intervals for great earthquakes of the past 3500 years at northeastern Willapa Bay, Washington, U. S. Geol. Surv. *Prof. Pap.*, 1576, 108 pp., 1997.

Baumberger T., C. Caroli, and O. Ronsin, Self healing slip pulses along a gel/glass interface, Phys. Rev. Lett., 88, p0755, 2002.

Bilek, S. L., S. Y. Schwartz, and H. R. DeShon, Control of seafloor roughness on earthquake rupture behavior. G*eology* 31, 5; 455–458, 2003.

Bilek, S. L., Influence of subducting topography on earthquake rupture, in The seismogenic zone of subduction thrust fault, edited by T. Dixon and C. Moore, pp. 123-146, Columbia University Press, New York, 2007.

Burgmann, R., M. G. Kogan, V. E. Levin, C. H. Scholz, R. W. King, and G. M. Steblov, Rapid aseismic moment release following the 5 December, 1997 Kronotsky, Kamchatka, earthquake, *Geophys. Res. Lett.*, 28, 1331–1334, 2001.

Cohen, S. C., and J. T. Freymueller, Crustal uplift in the southcentral Alaska subduction zone: A new analysis and interpretation of tide gauge observations, *J. Geophys. Res.*, 106, 11,259-11,270, 2001.

Currie C. A., R. D. Hyndman, K. Wang, V. Kostoglodov, Thermal models of the Mexico subduction zone: Implications for the megathrust seismogenic zone, *J. Geophys. Res.*, 1061 107(B12), doi: 10.1029/2001JB000886, 2002.

Das, S., and C. H. Scholz, Why large earthquakes do not nucleate at shallow depths, *Nature*, 305, 621– 623, 1983.

Dieterich, J. H., Modeling of rock friction. 1. Experimental results and constitutive equations, *J. Geophys. Res*., 84(NB5), 2161-2168, 1979.

Di Giuseppe, E., F. Funiciello, F. Corbi, G. Ranalli and G. Mojoli, Gelatins as rock analogs: A systematic study of their rheological and physical properties, *Tectonophysics*, 473(3-4), 391-403, doi:10.1016/j.tecto.2009.03.012, 2009.

Dixon T. and Moore J. C:, Introduction, in The seismogenic zone of subduction thrust fault, edited by T. Dixon and C. Moore, pp. 2-15, Columbia University Press, New York, 2007.

Funiciello F., M. Moroni, C. Piromallo, C. Faccenna, A. Cenedese, and H. A. Bui, Mapping mantle flow during retreating subduction: Laboratory models analyzed by feature tracking, *J. Geophys. Res*, 111, B03402, doi:10.1029/2005JB003792, 2006.

Gomberg, J. and C. W. Grp, Slow-slip phenomena in Cascadia from 2007 and beyond: A review, *Geol. Soc. Am. Bull.*, 122(7-8), 963-978, doi:10.1130/B30287.1, 2010.

Guillaume, B., F. Funiciello, C. Faccenna, J. Martinod, and V. Olivetti, Spreading pulses of the Tyrrhenian Sea during the narrowing of the Calabrian subduction zone, Geology, 38(9), 819–822, doi:10.1130/G31038.1, 2010.

Hayes, C. W., and C. P. Conrad, Subduction dynamics and great earthquakes, Eos Trans. AGU, 88(52), Fall Meet. Suppl., Abstract T52A□05, 2007.

Heuret, A., S. Lallemand, F. Funiciello, C. Piromallo, C. Faccenna, Physical properties of subduction-type seismogenic zones revisited, *Geochem. Geophys. Geosyst.*, in press.

Hyndman R. D., What we know and what we don't know, in The seismogenic zone of subduction thrust faults, edited by T. Dixon and C. Moore, pp. 15-40, Columbia University Press, New York, 2007.

Hyndman, R. D. and K. Wang, Thermal Constraints on the Zone of Major Thrust Earthquake Failure - the Cascadia Subduction Zone, *J. Geophys. Res., [Solid Earth],* 98(B2), 2039-2060, 1993.

Hyndman R. D., M. Yamano, K. Wang, Thermal constraints on the seismogenic portion of the southwestern Japan subduction thrust, *J. Geophys. Res.,* 100, 15373-15392, 1995.

Hyndman, R. D., M. Yamano, and D. A. Oleskevich, The seismogenic zone of subduction thrust fault, *Isl. Arc*, 6, 244–260, doi:10.1111/j.1440-1738.1997.tb00175.x, 1997.

Kanamori, H., Rupture process of subduction zone earthquakes, *Annu. Rev. Earth Planet. Sci*., 14, 293–322, doi:10.1146/annurev.ea.14.050186.001453, 1986.

Khazaradze, G., and J. Klotz, Short- and long-term effects of GPS measured crustal deformation rates along the south central Andes*, J. Geophys. Res*., 108(B6), 2289, doi:10.1029/2002JB001879, 2003.

Klotz, J., et al., GPS-derived deformation of the central Andes including the 1995 Antofagasta Mw = 8. 0 earthquake, *Pure Appl. Geophys*., 154, 3709–3730, 1999.

Klotz, J., G. Khazaradze, D. Angermann, C. Reigber, R. Perdomo, and O. Cifudentes, Earthquake cycle dominates contemporary crustal deformation in central and southern Andes, *Earth Planet. Sci. Lett*., 193, 437– 446, 2001.

Kodaira, S., E. Kurashimo, N. Takahashi, A. Nakanishi, S. Miura, J.-O. Park, T. Iwasaki, N. Hirata, K. Ito, and Y. Kaneda, Structural factors in controlling a rupture process of a magathrust earthquake at the Nankai trough seismogenic zone: results from an onshore-offshore seismic study, *Geophys. J. Inter.*, 149, 815–835, 2002.

Lapusta, N., J. R. Rice, Y. Ben-Zion and G. T. Zheng, Elastodynamic analysis for slow tectonic loading with spontaneous rupture episodes on faults with rate- and state-dependent friction, *J. Geophys. Res., [Solid Earth],* 105(B10), 23765-23789, 2000.

Lay, T. and H. Kanamori, An asperity model of large earthquake sequences, in Earthquake Prediction - an International Review, edited by D. W. Simpson and P. G. Richards, pp. 579-592, AGU, Washington, DC, 1981.

Lay, T., H. Kanamori and L. Ruff, The asperity model and the nature of large subduction zone earthquakes, *Earthquake Pred. Res*., 1, 3-71, 1982.

Lay T., H. Kanamori, C. Ammon, M. Nettles, S. Ward, R. Aster, S. Beck, S. Bilek, M. Brudzinski, R. Butler, H. DeShon, G. Ekström, K. Satake, S. Sipkin, The Great Sumatra-Andaman Earthquake of 26 December 2004, *Science*, 308 (5725), 1127-1133, doi: 10.1126/science.1112259, 2005.

Lykotrafitis, G., et al. (2006), Self-healing pulse-like shear ruptures in the laboratory, *Science*, 313, 1765– 1768, doi:10.1126/science.1128359.

McCaffrey, R., The next great earthquake, Science, 315(5819), 1675-1676, doi:10.1126/science.1140173, 2007.

McCaffrey, R., Global frequency of magnitude 9 earthquakes, *Geology*, 36(3), 263-266, doi:10.1130/G24402A.1, 2008.

Melbourne, T., Webb, F., Stock, J. & Reigber, C., Rapid post-seismic transients in subduction zones from continuous GPS, *J. geophys. Res.*, 107(B10), 2241, doi:10.1029/2001JB000555, 2002.

Miozzi M., Particle image velocimetry using feature tracking and Delauny tessellation Proc. 12th Int. Symp. on Application of Laser Techniques to Fluid Mechanics (Lisbon), 2004.

Mori J, Are asperities persistent features in repeated great earthquakes? paper presented at AGU Chapman Conference on Giant Earthquakes and their Tsunamis, Valparaiso, Chile, 2010.

Moroni M. and A. Cenedese, Comparison among feature tracking and more consolidated velocimetry image analysis techniques in a fully developed turbulent channel flow, *Meas. Sci. Technol.* 16, 2307–2322, 2005.

Norabuena, E., L. Leffler-Griffin, A. Mao, T. Dixon, S. Stein, I. S. Sacks, L. Ocola, and M. Ellis, Space geodetic observations of Nazca- South America convergence across the central Andes, *Science*, 279(5349), 358 – 362, doi:10.1126/science.279.5349.358, 1998.

Oleskevich, D. A., R. D. Hyndman, and K. Wang, The updip and downdip limits to great subduction earthquakes: Thermal and structural models of Cascadia, south Alaska, SW Japan, and Chile, *J. Geophys. Res.*, 104(B7), 14,965– 14,991, doi:10.1029/1999JB900060, 1999.

Pacheco J. and L. Sykes, Seismic moment catalog for large shallow earthquakes from 1900 to 1989, *Bull. Seism. Soc.*, 82, 1306-1349, 1992.

Pacheco J. F., L. R., Sykes and C. H. Scholz, Nature of seismic coupling along simple plate boundaries of the subduction type, *J. Geophys. Res.*, 98, 14133-14158, 1993.

Peterson, E. T., and T. Seno, Factors affecting seismic moment release rates in subduction zones, *J. Geophys. Res.*, 89, 10,233–10,248, doi:10.1029/JB089iB12p10233, 1984.

Plafker, G., Alaskan earthquake of 1964 and Chilean earthquake of 1960: Implications for arc tectonics, *J. Geophys. Res.*, 77, 901–925, 1972.

Plafker, G., and J. Savage, Mechanism of the Chilean earthquake of May 21 and 22, 1960, *Geol. Soc. Am. Bull.*, 81, 1001–1030, 1970.

Rice, J. R., Spatiotemporal Complexity of Slip on a Fault, *J. Geophys. Res., [Solid Earth]*, 98(B6), 9885-9907, 1993.

Rosenau, M., J. Lohrmann and O. Oncken, Shocks in a box: An analogue model of subduction earthquake cycles with application to seismotectonic forearc evolution, *J. Geophys. Res., [Solid Earth]*, 114, B01409, doi:10.1029/2008JB005665, 2009.

Rosenau, M., and O. Oncken, Shocks in a box 3D: Experimental insights into seismotectonic segmentation and synchronization of megathrust earthquakes in subduction zones, paper presented at GeoMod 2010, Fac. of Sci., Univ. of Lisbon, Lisbon, 2010.

Rossetti, F., Faccenna, C., Ranalli, G., Storti, F., Convergence rate-dependent growth of experimental viscous orogenic wedges. Earth Planet. Sci. Lett. 178, 367–372, 2000.

Rubio, M. A. and J. Galeano, Stick-Slip Dynamics in the Relaxation of Stresses in a Continuous Elastic Medium, *Phys Rev E*, 50(2), 1000-1004, 1994.

Ruff, L. J., and H. Kanamori, Seismicity and the subduction process, *Phys. Earth Planet. Inter.*, 23, 240–252, doi:10.1016/0031-9201(80)90117-X, 1980.

Ruff, L. J., Do trench sediments affect great earthquake occurrence in subduction zones?, in Subduction Zones Part I, edited by L. J. Ruff and H. Kanamori, Pure Appl. Geophys., 129, 263–282, 1989.

Ruina, A., Slip instability and state variable friction laws, *J. Geophys. Res.*, 88(NB12), 359-370, 1983.

Saffer, D. M. and C. Marone, Comparison of smectite- and illite-rich gouge frictional properties: application to the updip limit of the seismogenic zone along subduction megathrusts, *Earth Planet. Sci. Lett.*, 215(1-2), 219-235, doi:10.1016/S0012-821X(03)00424-2, 2003.

Satake K. and B. F. Atwater, Long-term perspectives on giant earthquakes and tsunamis at subduction zones, *Annual Review of Earth Planet. Sci. Lett.*, 35, 349-374, 2007.

Scholz, C. H., Geophysics - Earthquakes as Chaos, *Nature*, 348(6298), 197-198, 1990.

Scholz, C. H., Earthquakes and friction laws, *Nature*, 391(6662), 37-42, 1998.

Scholz, C. H., and J. Campos, On the mechanism of seismic decoupling and backarc spreading at subduction zones, *J. Geophys. Res.*, 100, 22,103–22,115, doi:10.1029/ 95JB01869, 1995.

Schwartz, S. Y. and J. M. Rokosky, Slow slip events and seismic tremor at circum-pacific subduction zones, *Rev. Geophys.*, 45(3), RG3004, 2007.

Seno T., Fractal asperities, invasion of barriers, and interplate earthquakes*, Earth Planets Space*, 55 (11), 649-665, 2003.

Shimamoto, T., T. Seno, and S. Uyeda, Rheological framework for comparative subductology, in Relating Geophysical Structures and Processes: The Jeffreys Volume, Geophys. Monogr., edited by K. Aki and R. Dmowska, IUGG/AGU, 76, 39–52, 1993.

Stein S. and E. A. Okal, Speed and size of the Sumatra earthquake, *Nature*, 434, 581-582, 2005.

Thatcher W. and J. B. Rundle, A viscoelastic coupling model for cyclic deformation due to periodically repeated earthquakes at subduction zones, *J. Geophys. Res.*, 89, 7631-7640, 1984.

Uyeda, S., and H. Kanamori, Back arc opening and the mode of subduction, *J. Geophys. Res.*, 84, 1049–1061, doi:10.1029/JB084iB03p01049, 1979.

Wang, K., Coupling of tectonic loading and earthquake fault slips at subduction zones, *Pure Appl. Geophys.*, 145(3/4), 537-559, 1995.

Wang K., J. He, H. Dragert and T. James, Three-dimensional viscoelastic interseismic deformation model for the Cascadia subduction zone, *Earth Planets Space*, 53, 295–306, 2001.

Wang K., R. Wells, S. Mazzotti,R.D. Hyndman, and T. Sagiya, A revised dislocation model of interseismic deformation of the Cascadia subduction zone, *J. Geophys. Res*, 108, B1, 2026, doi:10.1029/2001JB001227, 2003.

Wang, K., and Y. Hu, Accretionary prisms in subduction earthquake cycles: The theory of dynamic Coulomb wedge, *J. Geophys. Res.*, 111, B06410, doi:10.1029/2005JB004094, 2006.

Wang, K., Elastic and viscoelastic models of crustal deformation in subduction earthquake cycle, in The seismogenic zone of subduction thrust fault, edited by T. Dixon and C. Moore, pp. 2-15, Columbia University Press, New York, 2007.

Wang, K., What facilitates or hinders giant earthquakes, paper presented at AGU Chapman Conference on Giant Earthquakes and their Tsunamis, Valparaiso, Chile, 2010.

Yagi, Y., M. Kikuchi, and T. Nishimura, Co-seismic slip, postseismic slip, and largest aftershock associated with the 1994 Sanrikuharuka- oki, Japan, earthquake, *Geophys. Res. Lett*., 30(22), 2177, doi:10.1029/2003GL018189, 2003.

Chapter 7

Cloos, M., Thrust-Type Subduction-Zone Earthquakes and Seamount Asperities - a Physical Model for Seismic Rupture, *Geology*, 20(7), 601-604, 1992.

Das, S. and C. Scholz, Why large earthquakes do not nucleate at shallow depths, *Nature*, 305, 621-623, 1983

Gorbatov, A., and Kennett, B.L.N., Jount bulk-sound and shear tomography for Western Pacific subduction zones, *Earth and Planetary Science Letters*, v. 210, 527-543, 2003.

Gutscher, M. A. and G. K. Westbrook, Great earthquakes in slow-subduction, low-taper margins, in Subduction zone geodynamics, edited by S. Lallemand and F. Funiciello, pp. 119-133, Springer Berlin Heidelberg, 2009.

Heuret, A., S. Lallemand, F. Funiciello, C. Piromallo, C. Faccenna, Physical properties of subduction-type seismogenic zones revisited, *Geochem. Geophys. Geosyst.*, in press.

Hindle, D., Kley, J., Oncken, O., and Sobolev, S., Crustal balance and crustal flux from shortening estimates in the Central Andes: *Earth and Planetary Science Letters*, 230, 113-124, 2005.

Klay, J. and Monaldi, C.R., Tectonic shortening and crustal thickness in the Central Andes: How good in the correlation?: *Geology*, 26, 723-726 1998.

Molnar, P., and Atwater, T., Interarc spreading and cordilleran tectonics as alternates related to the age of subducted oceanic lithosphere, *Earth and Planetary Science Letters*, 41, 330-340, 1978.

Pacheco, J. F. and L. R. Sykes, Seismic Moment Catalog of Large Shallow Earthquakes, 1900 to 1989, *Bull. Seismol. Soc. Am*., 82(3), 1306-1349, 1992.

Pacheco, J. F., L. R. Sykes and C. H. Scholz, Nature of Seismic Coupling Along Simple Plate Boundaries of the Subduction Type, *J. Geophys. Res., [Solid Earth]*, 98(B8), 14133-14159, 1993.

Rosenau M., R. Nerlich, S. Brune and O. Oncken, Experimental insights into the scaling and variability of local tsunamis triggered by giant subduction megathrust earthquakes *J. Geophys. Res*. 115, B09314, doi:10.1029/2009JB007100, 2010.

Schellart, W.P., Freeman, J., Stegman, D.R., Moresi, L., and May, D., Evolution and diversity of subduction zones controlled by slab width, *Nature*, 446, 308-311, 2007.

Wang, K., What facilitates or hinders giant earthquakes, paper presented at AGU Chapman Conference on Giant Earthquakes and their Tsunamis, Valparaiso, Chile, 2010.

Acknowledgements

The first acknowledgement is to my friend/supervisor Francesca Funiciello, for the opportunity she gave me. My PhD experience represented a moment of great scietific and personal growt. Working and discussing with Francesca has always been a pleasure. In particular I thank her for stimulating in me the pleasure of the research and for the good atmosphere I've always lived in. I will always be grateful to Francesca.

Special thanks to Claudio Faccenna, for transmiting me his entusiastic approach to science. I'm particularly grateful to him for introducing me into an international- state of the art scientific community.

I'm particularly grateful to my friend Erika Di Giuseppe how showed me the right way at the beginning of this experience; she is still remaining a reference.

I always enjoyed working with prof. Giorgio Ranalli, Giampiero Iaffaldano, Javier Galeano, Arnauld Heuret, Monica Moroni, Ogus Gogus, Giorgio Mojoli, Ylona van Dinther, thank you all.

Thanks to my personal Matlab trainer Valentina and to the best lab-mate Benjamin.

Thanks to my friend Francesca Cifelli who delight me with food specialties that made me feel at home every day (particularly during lunches!).

I am grateful to Matthias Rosenau and Giacomo Corti, who accepted to review my Thesis.

I would like to thank all my friends and all the members of the Fantor Team for the beers, for laughing together and for enjoining every moment spent together including serious ones.

Particular thanks to the fuel that all my kites and my boards gave me and for helping in riding wild winds!

A really special thanks to Claudia for everything happened during the last years, including finding the best wife.

I am very grateful to my mother Michela and my father Stefano that always supported me with love.